
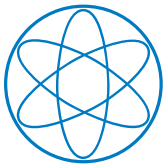


Light-Matter Interactions and Electron Dynamics of Semiconductor Systems in Femto- and Attosecond Timescale

Dissertation

of

Dionysios Potamianos

Fakultät für Physik

Light-Matter Interactions and Electron Dynamics of Semiconductor Systems in Femto- and Attosecond Timescale

Dionysios Potamianos

Vollständiger Abdruck der von der Fakultät für Physik der Technischen Universität München zur Erlangung des akademischen Grades eines
Doktors der Naturwissenschaften
genehmigten Dissertation.

Vorsitzender: apl. Prof. Dr. Norbert Kaiser
Prüfer der Dissertation:
1. Prof. Dr. Reinhard Kienberger
2. Prof. Dr. Wilhelm Auwärter

Die Dissertation wurde am 23.08.2021 bei der Technischen Universität München eingereicht und durch die Fakultät für Physik am 07.12.2021 angenommen.

Abstract

In the present work, experimental and computational investigations on the response of several semiconductor systems upon exposure to light pulses are presented. The considered responses span from relatively long lived nanosecond (10^{-9} s) scale, where energy dissipation mechanisms along a large area of the semiconductor crystal is to be considered, to the picosecond (10^{-12} s) and femtosecond (10^{-15} s) scales, where the electronic motion around the parent atom dominates, all the way down to the attosecond (10^{-18} s) scale, where only the initial photo-excitation and the immediate effects of the potential landscape on the excited electron are relevant.

The determination of the intraband dynamics of mono- and polycrystalline Mg-Phthalocyanine thin film semiconductors were determined by means of the mid-infrared-pump visible-probe transient absorption technique, revealing a dimensionality difference in the excitonic dissipation mechanism. The interband dynamics of the two systems were experimentally investigated using a visible-pump visible-probe transient absorption technique. A computational model was developed to describe the interband and excitonic dynamics that were recorded with the latter technique. The use of the model allowed for the full dynamics description of the monocrystalline system and the uncoupling of the complex dynamics of the polycrystalline system, pinning the differences in the optical response to structural differences between the two crystal variants.

A complete investigation was launched on the implementation of the solid-state attosecond streaking spectroscopy technique as a transient photoemission setup for recording the photoexcitation dynamics of semiconductor surfaces with attosecond resolution, yielding experimentally negative results due to parasitic effects, but introducing useful concepts towards the development of setups dedicated on such purpose, as well as analysis and computational methods.

The effect of the ionizing photon energy on the photoionization delay from homo-nuclear semiconductor system, namely highly oriented pyrolytic graphite, is experimentally determined and supported by computational methods around the bandgap present 84 eV above the Fermi energy. The effect was found to be an increase in the Eisenbud-Wigner-Smith delay, which translates to an effective retardation of the photoionization process when the excitation energy liess within the bandgap.

Zusammenfassung

In der vorliegenden Arbeit werden experimentelle und theoretische Untersuchungen zum Verhalten verschiedener Halbleitersysteme nach Absorption von Lichtpulsen vorgestellt. Die betrachteten Reaktionen reichen von der relativ langlebigen Nanosekundenskala (10^{-9} s), wo Energiedissipationsmechanismen entlang einer großen Fläche des Halbleiterkristalls zu berücksichtigen sind, über die Pikosekunden- (10^{-12} s) und Femtosekundenskala (10^{-15} s), wo die elektronische Bewegung um das Mutteratom dominiert, bis hin zur Attosekundenskala (10^{-18} s), wo die initiale Photoanregung und die unmittelbaren Auswirkungen der Potentiallandschaft auf das angeregte Elektron relevant sind.

Die Bestimmung der Intrabanddynamik von mono- und polykristallinen Mg-Phthalocyanin-Dünnschicht-Halbleitern wurde mit Hilfe der transienten VIS-Anrege und MIR-Abfrage Absorptionsspektroskopie ermittelt, wobei ein Dimensionalitätsunterschied im exzitonischen Dissipationsmechanismus festgestellt wurde. Die Interbanddynamik der beiden Systeme wurde experimentell mit Hilfe einer sichtbar-Anregung sichtbar-Abfrage transienten Absorptionstechnik untersucht. Ein Theoriemodell wurde entwickelt, um die Interband- und exzitonischen Dynamiken zu beschreiben, die mit der letztgenannten Technik identifiziert wurden. Die Anwendung des Modells ermöglichte die vollständige Beschreibung der Dynamiken des monokristallinen Systems und die Entkopplung der komplexen Dynamiken des polykristallinen Systems, wobei die Unterschiede in der optischen Antwort auf strukturelle Unterschiede zwischen den beiden Kristallvarianten zurückgeführt wurden.

Es wurde eine vollständige Untersuchung der Festkörper-Attosekunden-Streaking-Spektroskopie-Technik als transienter Photoemissionsaufbau zur Aufzeichnung der Photoanregungsdynamiken von Halbleiteroberflächen mit Attosekunden-Auflösung durchgeführt. Aufgrund von parasitären Effekten lieferte dies experimentell negative Ergebnisse, aber nützliche Konzepte für die Entwicklung von Aufbauten für solche Zwecke und auch die Einführung von Analyse- und Berechnungsmethoden.

Der Effekt der ionisierenden Photonenenergie auf die Photoionisationsverzögerung von homo-nuklearen Halbleitersystemen, nämlich hochorientiertem pyrolytischem Graphit, wird ex-

perimentell bestimmt und durch rechnerische Methoden um die Bandlücke herum unterstützt, die 84 eV oberhalb der Fermi-Energie liegt. Der Effekt konnte als eine Erhöhung der Eisenbud-Wigner-Smith-Verzögerung erklärt werden, was zu einer effektiven Verzögerung des Photoionisationsprozesses führt, wenn die Anregungsenergie innerhalb der Bandlücke liegt.

List of Publications

M. Schnitzenbaumer, D. Potamianos, C. Lemell, P. Scigalla, F. Libisch, E. Schock-Schmidtke, M. Haimerl, M. Schäffer, J. T. Küchle, J. Riemensberger, Y. Cui, U. Kleineberg, J. Burgdörfer, J. V. Barth, P. Feulner, F. Allegretti and R. Kienberger, *"Attosecond chronoscopy of the photoemission near a band gap of 2 a single-element layered system," PRL,* ***2021*** *(In review).*

D. Potamianos, M. Nuber, A. Schletter, M. Schnitzenbaumer, M. Haimerl, P. Scigalla, M. Wörle, R. Kienberger, and H. Iglev, *"Full dynamics description of Mg-Phthalocyanine mono- and poly-crystalline semiconductor systems," J. Phys. Chem. C,* ***2021*** *(Accepted).*

J. Riemensberger, S. Neppl, D. Potamianos, M. Schäffer, M. Schnitzenbaumer, M. Ossiander, C. Schröder, A. Guggenmos, U. Kleineberg, D. Menzel, F. Allegretti, J. V. Barth, R. Kienberger, P. Feulner, A. G. Borisov, P. M. Echenique, and A. K. Kazansky, *"Attosecond dynamics of sp-band photoexcitation," PRL, vol. 123,* ***2019*** .

S. Prinz, M. Schnitzenbaumer, D. Potamianos, M. Schultze, S. Stark, M. Häfner, C. Y. Teisset, C. Wandt, K. Michel, R. Kienberger, B. Bernhardt, and T. Metzger, *"Thin-disk pumped optical parametric chirped pulse amplifier delivering CEP-stable multi-mJ few-cycle pulses at 6 kHz," Opt. Express, vol. 26, p. 1108,* ***2018****.*

I. Papagiannouli, D. Potamianos, T. Krasia-Christoforou, and S. Couris, *"Third-order optical nonlinearities of PVP/Pd nanohybrids," Opt. Mater., vol. 72, pp. 226–232, 10* ***2017****.*

D. Potamianos, I. Papadakis, E. Kakkava, A. B. Bourlinos, G. Trivizas, R. Zboril, and S. Couris, *"Nonlinear optical response of gold-decorated nanodiamond hybrids," J. Phys. Chem. C, vol. 119, pp. 24614–24620,* ***2015****.*

K. Iliopoulos, D. Potamianos, E. Kakkava, P. Aloukos, I. Orfanos, S. Couris, G. Papadopoulos, D. Bonifazi, C. Sooambar, A. Mateo-Alonso, and M. Prato, *"Ultrafast third order nonlinearities of organic solvents," Opt. Express, vol. 23, pp. 131–134,* ***2015****.*

List of Abbreviations

CW Continuous Wave

HHG High Harmonic Generation

XUV Extreme Ultraviolet

RWA Rotating Wave Approximation

DOS Density of States

MIR Mid-Infrared

NOPA Noncollinear Optical Parametric Amplifier

NIR Near-Infrared

OPA Optical Parametric Amplifier

DFG Difference Frequency Generation

SHG Second Harmonic Generation

BBO Beta Barium Borate $Ba(BO_2)_2$

OLED Organic Light Emitting Diode

Pc Phthalocyanines

H2Pc Phthalocyanine

MPc Metal Phthalocyanine

MgPc Magnesium Phthalocyanine

DCM Dichloromethane

VIS Visible

FTIR Fourier Transform Infrared

XRD X-ray Diffraction

GI Grazing Incidence

DMF N,N-Dimethylformamide

SPM Self-Phase Modulation

ESA Excited State Absorption

GSB Ground State Bleaching

ISC Inter-System Crossing

TOF Time of Flight

SFA Strong Field Approximation

CEP Carrier Envelope Phase

FROG Frequency Resolved Optical Gating

LSGPA Least-Squares Generalized Projections Algorithm

COE Center of Energy

TDSE Time-Dependent Schrödinger's Equation

MPQ Max Plank Institute for Quantum Optics

TUM Technical University of Munich

AOFS Acousto-Optic Frequency Modulator

CPA Chirped Pulse Amplification

XPS X-ray Photoemission Spectroscopy

LEED Low-Energy Electron Diffraction

TPD Temperature Programmed Disorption

STM Scanning Tunneling Microscopy

STS Scanning Tunneling Spectroscopy

EDC Energy Dispersion Curves

DFT Density Functional Theory

OMBE Organic Molecular Beam Epitaxy

HOMO Highest Occupied Molecular Orbital

LUMO Lowest Unoccupied Molecular Orbital

ATI Above-Threshold Ionization

ARPES Angle-Resolved Photoemission Spectroscopy

HOPG Highly Oriented Pyrolytic Graphite

XES X-ray Emission Spectroscopy

VASP Vienna Ab initio Simulation Package

EWS Eisenbud-Wiegner-Smith

PIE Ptychographic Iterative Engine

Contents

Chapter 1

Introduction

A major part of our experience of the physical world comes from light which is generated, interacts with the environment and finds its way into our eyes, where it interacts again with the neurons in our retinas. The information coming from light being generated, propagated and finally absorbed into our retinas is decoded in our brain into the sensation of vision. By this fact alone, one should realize that the amount of information a photon carries is the result of its history. The detection of photons with well-designed experimental techniques can reveal information about its past, from the moment of generation to its interaction with its environment, ultimately revealing how matter acts on a specific instance. The generation of a detected photon is nothing more than an atom releasing energy into the environment. Collecting light that is emitted by an atom (or a collection of atoms) can reveal crucial information about the source. A large portion of our understanding of the universe comes from such measurements on distant stars, revealing their composition, size, distance and status.

On the other hand, how light interacts with matter after it has been generated can also reveal the nature of the illuminated material, as it will leave a distinct mark in the light that interacted with it. Spectroscopy was the first experimental technique that revealed the quantised nature of atoms, since the absorption and emission of radiation of atoms happens only in discrete wavelengths. Spectroscopic studies are among the first tools that one would use for probing an unknown substance, wanting to find its composition and properties.

When it comes to technology, especially manipulating the world around us, our most advanced tool is admittedly electronics. Using currents and voltages to move matter, emit light, detect changes in the environment is typically done by electronic devices that operate, store and process information in the form of electrical signals. As much as we seem to be proficient in electronics, though, there are intrinsic limitations, as the propagation of electrons comes with inherit dispersion, ultimately broadening and destroying the electric signals. The response of

electrons and the atoms within our electronic devices is also not instantaneous, leading to restrictions in the durations of rise and fall times of an electronic signal, limiting the duration of controlled electrical pulses that we can have. In modern day electronics, control up to picosecond (10^{-12} s) time scale can be achieved in specific cases. This time scale, although impressive, does not compare with the timescales that the electrons move within atoms, reaching the femtosecond (10^{-15} s) time scale. In order to investigate the dynamic behavior of matter in the scale of individual atoms, we need to move to a different kind of clocking mechanism. Here is where light enters the picture again, as with the advent of lasers, intense short pulses can be generated.

Laser technology holds the record for the shortest man-made event. In typical laser setups, using Q-switching and mode-locking, the output can be light pulses from nanosecond (10^{-9} s) all the way down to femtosecond (10^{-15} s) durations, and of stable repetition rates typically up to megahertz regimes. In dedicated setups, pulses in the attoesecond (10^{-18} s) regime can be achieved. At this extreme time scale the electrons within an atom barely have any time to react to any external stimulus. It is the time scale where the subatomic particle reactions can be expected to occur. To obtain the most complete picture of how matter behaves, light has to be used as a stimulation and detection method, since it can be controlled it to an extend that is enough for recording all the possible dynamics within an atom.

The main subject of this work was the understanding of light-matter interactions, which is key for tracing the information encoded into light back to the dynamic response of matter to an external stimulus. Being able to trace the information inevitably reveals the nature of the material in question. By having a good understanding of the light-matter interactions, one can investigate the possibility of implementing a solid state attosecond streaking spectroscopy setup as a transient photoemission technique for the determination of the photo-excitation dynamics in solid samples such as organic monolayer semiconductors or in principle semiconductor materials with sub-femtosecond temporal resolution. In addition, by utilising a solid-state attosecond streaking spectroscopy setup, one can investigate the dynamics of the photoemission process.

Chapter 2 will give a detailed description of light and light pulses in the scope of electromagnetism. As this work heavily utilized pulsed laser systems to perform measurements of optical response and photo-ionization, a clear definition of the pulse properties is necessary. The definitions of the pulses were also proven useful for constructing the simulations of the different systems.

Chapter 3 will further focus on theoretical aspects of this work. More specifically, the quantum mechanical description of matter will be presented, as well as the different ways to treat light matter interactions within the frame of quantum optics. This is important as the development of quantum mechanical computational framework was a significant part of this thesis and

allowed for the analysis of complex signals and the theoretical prediction of the response of mater under photo-excitation. In addition, this chapter inevitably paves the way for understanding the photo-ionization process, as well as the more complicated attosecond streaking spectroscopy technique in which several light-matter interactions take place simultaneously whilst manifesting in different ways.

In Chapter 4, the findings of a study on Mg Phthalocyanine thin film semiconductors of different structural complexity, using transient absorption techniques in the mid-infrared and visible range, will be presented. First, a brief introduction of the technique will be given, followed by an introduction of the Mg Phthalocyanine molecule, the fabrication methods and the characterization of the fabricated films. After that, the results and findings of the intra-band dynamics recorded with a picosecond resolution mid-infrared-probe transient absorption setup will be given, followed by the results of the inter-band dynamics recorded with a femtosecond resolution visible-probe transient absorption setup. Lastly, the construction of a model for describing the complex inter-band dynamics will be shown. The results of the simulations will be shown and discussed as they allow for the interpretation of every major feature of the recorded signals and even help decouple contributions from different morphological components of the studied films.

From Chapter 5 onwards, we will focus on the attosecond regime, and more specifically, on the solid state attosecond streaking spectroscopy. Chapters 5 and 6 will focus on implementing the attosecond streaking spectroscopy technique as a visible-pumped transient photoemission technique. Chapter 5 will give a theoretical description of the attosecond streaking spectroscopy. Based on that, a theoretical model capable of predicting the signals one should expect in such an experiment will be constructed. The chapter will conclude by exploring the different analysis schemes and methods that can be devised to analyze the experimental recordings and deduce the dynamics from them.

In Chapter 6, the experimental findings from utillzing the attosecond streaking spectroscopy technique as a visible-pumped transient photoemission technique will be presented. The experimental apparatus will be briefly introduced and a study on two different systems will be shown. First, a study of Mg Phthalocyanine self assembled monolayer on an Ag(100) surface will be presented, starting with a description of the preparation method and characterization of the sample, followed by a density functional theory (DFT) study of the molecule, the output of which will then be introduced into the model devised in Chapter 5, giving a prediction of the signals expected. The experimental findings will then be presented, revealing some parasitic space-charge effects. A study of a second system, namely a Gallium Antimonide (GaSb) wafer, is shown in order to mitigate some of the shortcomings of the molecular monolayer system. An expansion of the model described in the previous chapter is given in order to include band struc-

ture effects into the description, enabling the model to describe semiconductors. This allows the recalculation of the expected signal for the new system. The experimental findings of this study are then presented, revealing further that the parasitic effects cannot be overcome by the given instrumentation. The chapter concludes with a discussion of other methods to surpass the limitations encountered in this study.

Chapter 7 will focus on the intended use of attosecond streaking spectroscopy as a chronoscopy technique, investigating the nature of solid state photoemission process in the attosecond time scale. The effect of the photon energy of the photo-ionizing radiation on the photoemission delay from a homonuclear layered system will be presented. A description of Highly Oriented Pyrolytic Graphite (HOPG), which is used as the homonuclear layered system in this study, and the preparation method used will be provided. The experimental findings will follow. A brief description of the theoretical models and the conclusions that they lead to is finally given to conclude this chapter.

Chapter 2

Light Pulses

In the present work, a firm understanding of light and the properties of light pulses is necessary for the description of the studied phenomena and methods. Therefore, a brief description of light is presented here. Throughout the chapter, the following sources were used [1--4].

Light is an oscillation of the electromagnetic field and is fully described as such from wave equations for the electric and magnetic fields that can be derived from Maxwell's equations. Solving the wave equations would provide the exact behavior of light for the specific case or problem. By knowing though the general properties of the wave equation some general conclusions can be derived that paint a rather accurate picture of the nature of light. Firstly, the wave equation can have harmonic or exponential solutions both in time and in space. As such, the most common behaviors, when studying light, have the above forms. When light propagates it does so as an oscillation of the electric and magnetic field. Like any other wave it can form standing waves given the right circumstances. When light penetrates a material that can absorb it, there is an exponential decay behavior. An exponential increase can be seen if light passes through a pumped active medium, causing amplification. Superposition is also a property that can immediately be derived from the wave equation, which is the source of a number of phenomena. Superposition of harmonic functions though give rise to a complete set. This means that any function within a given space can be described as a superposition of those harmonic functions. The Fourier analysis is thus a very common tool, with frequent transformation between the time and spectral domains, depending on which fits the specific case. In this work primarily time domain experiments were performed, although spectrally resolved, and thus main interest is in the time domain.

2.1 Light as an Electromagnetic Field

Any attempt in the understanding of light should start from the first principles. Maxwell's equations for electromagnetism describe the behavior of electric and magnetic fields and their interconnection. Assuming the absence of free charges and currents, they read:

$$\left.\begin{array}{ll} (i) \quad \boldsymbol{\nabla} \cdot \boldsymbol{E} = 0 & (iii) \quad \boldsymbol{\nabla} \times \boldsymbol{E} = -\dfrac{\partial \boldsymbol{B}}{\partial t} \\ (ii) \quad \boldsymbol{\nabla} \cdot \boldsymbol{B} = 0 & (iv) \quad \boldsymbol{\nabla} \times \boldsymbol{B} = \mu_0 \epsilon_0 \dfrac{\partial \boldsymbol{E}}{\partial t} \end{array}\right\} \tag{2.1}$$

By substituting and performing a few lines of math to the above the wave equation for light can be derived.

$$\nabla^2 \boldsymbol{E} = \mu_0 \epsilon_0 \frac{\partial^2 \boldsymbol{E}}{\partial t^2}, \qquad \nabla^2 \boldsymbol{B} = \mu_0 \epsilon_0 \frac{\partial^2 \boldsymbol{B}}{\partial t^2} \tag{2.2}$$

Having two wave equations for the same phenomenon shouldn't be intimidating or alienating, since the two are tightly connected by Equations 2.1(iii) and 2.1(iv). One field can be derived from Equation 2.2 and then, from Equations 2.1(iii) and 2.1(iv) derive the second field. It should already be obvious that the described waves travel with a speed of:

$$c = \frac{1}{\sqrt{\mu_0 \epsilon_0}} \approx 3 \times 10^8 m/s \tag{2.3}$$

Similar equations could be derived for within matter, but in the absence of free charges or currents, for which the propagation speed would be:

$$u = \frac{1}{\sqrt{\mu \epsilon}} \tag{2.4}$$

where μ is the magnetic permeability of the material and ϵ is the electric permittivity of the material. The refractive index can be defined as:

$$n = \frac{c}{u} = \sqrt{\frac{\mu \epsilon}{\mu_0 \epsilon_0}} \tag{2.5}$$

The above is a major statement for the nature of light as it is the most accurate description of light in terms of classical physics. Most, if not all, classical phenomena involving light can be calculated using the above, although this might not be the most efficient way for special cases.

2.2 Solution of the wave equation

Let us for the time being concern ourselves with this problem in one dimension and only for the electric field (since the wave equations are the same for E and B). In this case, the equation spells:

$$\frac{\partial^2 E}{\partial x^2} = \frac{1}{c^2}\frac{\partial^2 E}{\partial t^2}. \tag{2.6}$$

The electric field can be written as $E = X(x)T(t)$. Replacing that in the equation, yields:

$$c^2 \frac{X"}{X} = \frac{\ddot{T}}{T} \tag{2.7}$$

Since there are two functions of different independent values being always equal, this can only mean that they are always constant:

$$c^2 \frac{X"}{X} = \frac{\ddot{T}}{T} = \kappa \tag{2.8}$$

Now, one can independently solve each part of the partial differential equation as an ordinary differential equation. Starting with the temporal part, the following ordinary differential equation is obtained:

$$\ddot{T} - \kappa T = 0 \tag{2.9}$$

If $\kappa > 0$, so that $\kappa = \omega^2$, the solution would be in the form of:

$$T = Ae^{\omega t} + Be^{-\omega t} \tag{2.10}$$

Now, if $\kappa < 0$ so that $\kappa = -\omega^2$, the solution would be of the form:

$$T = A\sin\omega t + B\cos\omega t \tag{2.11}$$

That dilemma is usually decided by the initial and boundary conditions of the specific problem. For the time being though, let's proceed with the harmonic solution. This decision directly affects the solution of the spatial part, since:

$$X" + \frac{\omega^2}{c^2}X = 0 \tag{2.12}$$

giving us the solutions:

$$X = C\sin\frac{\omega}{c}x + D\cos\frac{\omega}{c}x \tag{2.13}$$

Now the solution for E can be written as:

$$E = XT = \left(C\sin\frac{\omega}{c}x + D\cos\frac{\omega}{c}x\right)(A\sin\omega t + B\cos\omega t) =$$

$$= AC\sin\frac{\omega}{c}xsin\omega t + BD\cos\frac{\omega}{c}x\cos\omega t + AD\cos\frac{\omega}{c}x\sin\omega t + BC\sin\frac{\omega}{c}x\cos\omega t$$

Although it's not always the case, if $AC = BD = A'$ and $AD = BC = B'$, let's define $k = \frac{\omega}{c}$.

$$= A'(\sin kxsin\omega t + \cos kx\cos\omega t) + B'(\cos kx\sin\omega t + \sin kx\cos\omega t) =$$

$$= A'\cos(kx - \omega t) + B'\sin(kx + \omega t)$$

This solution represents two traveling waves propagating in opposite directions. Let's only keep the right propagating wave by setting $B' = 0$.

$$E = A'\cos(kx - \omega t)$$

This equation describes a monochromatic wave of amplitude A' frequency $f = \frac{\omega}{2\pi}$ and wavelength $\lambda = \frac{k}{2\pi}$. But since this term is a solution of the wave equation, any sum of such terms would also be a solution of the wave equation.

$$E = \sum_i A'_i \cos\left(k_i x - \omega_i t\right) \tag{2.14}$$

This exercise, although trivial, brings to the fore some very important facts about the nature of light. First is the realization that, as a solution to the wave equation, light behaves in very specific ways, as described by Equations 2.10 and 2.11. For any observable behavior that seemingly doesn't follow the afore mentioned equations there is obviously a cause, be it interaction with matter, nonlinearities, quantum nature or just superposition. The second major observation is superposition itself. Equation 2.14 should already hint the reader towards the Fourier analysis. The implications of this are significant and should be investigated further for the understanding of light.

2.3 Superposition of Harmonics

As seen by the solution of the wave equation above, for a propagating electromagnetic wave the temporal and spatial part of the solution are oscillating terms. Those are connected by the equation $c = \lambda f$. In the present work, the spatial part was not integral and was therefore omitted from most dicussions.

2.3.1 Fourier Expansion

There can be any number of harmonic functions superposed as a solution of the wave equation. Harmonic functions form a complete set for a given interval, which in turn means that any continuous function (f) within that interval can be expressed as a sum of sine and/or cosine terms with a specific amplitude and phase. The last statement is called the Fourier theorem and is the basis on which some properties of light can be understood. It is expressed in discrete form as:

$$f(x) = \frac{1}{2}a_0 + \sum_{n=1}^{\infty} \left(a_n cos(nx) + b_n sin(nx)\right) \tag{2.15}$$

where a_0, a_n, b_n are the harmonic coefficients. This equation can easily be expressed as sine or cosine only terms while including a phase as:

$$f(x) = \frac{1}{2}a_0 + \sum_{n=1}^{\infty} c_n cos(nx - \theta_n) \tag{2.16}$$

with $c_n^2 = a_n^2 + b_n^2$ and $\tan\theta_n = b_n/a_n$. An expansion in the complex domain is also easy to implement using Euler's formula as:

$$f(x) = \sum_{n=-\infty}^{+\infty} d_n e^{\mathrm{i}(nx-\theta_n)} \tag{2.17}$$

in which $2d_n = a_n - \mathrm{i}b_n$, when $n \geq 0$ and $2d_n = a_n + \mathrm{i}b_n$ when $n < 0$. The last generalization would then be to allow the frequency (n) to span a continuous range, in which case the last equation can be written as:

$$f(x) = \int_{-\infty}^{+\infty} d(n) e^{\mathrm{i}(nx-\theta(n))} \mathrm{d}n \tag{2.18}$$

The generalization to a continuous range could also happen in any other form of the expansion. The latter though, would be the most relevant one. What follows is an attempt to contextualize it and explain its implications.

2.3.2 Time and Frequency Domains

The generalizations and replacements made to reach in Equation 2.18 reveal some important properties of light that are integral to the understanding of it. For instance, two new functions ($d(n)$ and $\theta(n)$) with very real and significant meanings were created. In order to bring everything into context, let us write the electric field of a propagating wave in a position in space (neglecting the spatial part) as the Fourier expansion of some function $S(\omega)$.

$$E(t) = \int_{-\infty}^{+\infty} S(\omega) e^{\mathrm{i}(\omega t-\theta(\omega))} \mathrm{d}\omega \tag{2.19}$$

where ω, as defined above, is the radial frequency. The function $S(\omega)$ is by definition the spectrum of this electric field. In other words, it shows how much of every frequency term the electric field contains. On the other hand, $\theta(\omega)$ is the spectral phase. It reveals the relative

phase between the different oscillation terms. Some more specific views on this function will be given later on, as some more concepts will be introduced. For the time being, a relation for calculating a spectrum of a given electric field can be given:

$$S(\omega) = \int_{-\infty}^{+\infty} E(t) e^{-\mathrm{i}(\omega t - \theta(t))} \mathrm{d}t \tag{2.20}$$

The equations above reveal that there is a very tight relation between the temporal and spectral features of a given electric field. It is worth mentioning that the operation of transforming from the electric field to the spectrum is called a Fourier transform, while the opposite is the inverse Fourier transform. The electric field in time and the spectrum and spectral phase are uniquely expressing each other and are representations of the same thing. In essence, it is a way to express the same quantity in an inverse space. As frequency is the inverse of period (hence time), features that are spread along time will be localized in the spectrum and vice versa. The most obvious but also extreme example is assuming a single sine or cosine function as the electric field in time. It goes without saying that the spectrum consists of a unique frequency, i.e. that of the sine or cosine function. Hence the spectrum would be a delta function in this particular frequency. Given that a sine/cosine function spans to infinity, in this example, a feature that is completely spread across time would result in the most defined feature in the spectrum, a spike in the specific frequency. Following the symmetry of the transform and inverse transform, a delta function in the electric field in time would result in a sine or cosine function in the spectrum, which is the exact opposite case.

Of course, in reality nothing is infinitely sharp and nothing seems to really span to infinity in time unperturbed, so in reality everything sits in-between the two given examples. However it should be apparent that sharp features in one domain spread out on the other. The ability to shift perspective (or domain) proves to be a useful tool in many cases.

2.4 Pulsating Light

Through the perspective of both domains for describing an electric field, it should now come as no surprise that a collection of frequency components with a specific phase relation would give rise to periodic structures in time domain which are called pulses. The duration of such pulses would relate to the spectral width of the source. Pulses, as sharp temporal features, are an extremely useful tool with which one can make clocks, which can be used to measure time. Electrical pulses are what makes computers possible. Telecommunications are based on electromagnetic pulses in different ranges of the spectrum. In physics (and in this work in particular) electromagnetic pulses are used to excite and evaluate the temporal evolution of

physical phenomena. The necessity for ever more sharp pulses is apparent since they allow for the determination of physical mechanisms with better resolution.

2.4.1 Obtaining Sharp Optical Pulses

In optics, the number one candidate for obtaining short pulses is tabletop lasers which are a source of intense, coherent light. There are a plethora of mechanisms and methods used to obtain pulses out of a laser, and although such devices do not hold the record for the shortest man-made event, they are an essential ingredient for making it.

At first, beam-blocks were periodically introduced to continuous wave (CW) lasers to obtain pulses that were capable of going down to microsecond timescale. It did not take long to realize that, by periodically attenuating the Q-factor of a laser cavity, pulsed operation of a laser could be obtained and pulse durations of down to nanoseconds were achievable [5, 6]. To be able to push to ever shorter pulses, considerations of both the spectral width and the spectral phase need to be taken into account. It was then shown that, if the frequency of Q-switching matches the round-trip time of the cavity (or a multiple of it), the available frequency components will lock their phases with respect to one another. This fact alone guarantees a much smaller pulse duration. This method is called mode-locking and is the limit of what can be achieved with a laser oscillator alone [7, 8]. To date the Ti:Sapphire oscillators are the record holders in this technology, with pulse durations down to 10 femtoseconds.

Apart from the laser oscillator there are more things that can be done. For a spectral region, the shortest pulse available is one where a complete carrier oscillation occurs. For the visible range, that oscillation is around 1.7 fs for 510 nm central wavelength. Pushing towards this limit, though, is a non trivial task. The pulses have to be amplified in order to be able to invoke nonlinear phenomena, which will then convert part of the excess energy in new spectral components. This is typically performed propagating the pulse through a hollow core fiber filled with a nonlinear medium. The pulse is then propagated through an optical system designed to correct the spectral phase and effectively compress the pulse. With such methods it is typical to reach few-cycle pulses. Pushing even further is achieved by spectrally separating the pulse, broadening and recombining the parts in a more controlled way. The resulting pulses are called light transients and reach the 1 cycle limit [9].

2.4.2 Passing the Femtosecond Barrier

Obtaining pulses with durations shorter than a femtosecond cannot be achieved in the optical range, since the average period is about 1.6 fs. The solution is to move to spectral regions where the carrier periods are smaller. Using intense optical pulses focused on a target material (usually

a gas), one can force electrons out of the parent ions. These electrons, as free charged particles in an electric field, will be accelerated by the strong electric field of the pulse and will then be driven back to the parent ion. If this happens, there is a chance of the electron recombining to the parent ion. The electrons that do recombine while having the excess energy from the intense pulse have to release it in the form of photons of higher frequency. The frequency will be an odd multiple of the pulses carrier frequency and the order depends on the electrons' excess energy. Such a process is called high harmonic generation (HHG) and results in pulse trains with attosecond duration [10, 11]. Such pulses are spectrally in the highest region of ultraviolet (UV) light up to the low X-ray region, called extreme ultraviolet (XUV). It is important to mention that, in this spectral range, the pulses are incapable of propagating in the atmosphere since they are heavily absorbed by any material. The HHG and the propagation of such pulses has to be done in vacuum.

2.4.3 Isolating an Attosecond Pulse

As described in the previous subsection, an attosecond pulse train can be generated by the process of HHG. For every zero crossing of the electric field that drives the harmonic generation, a new peak in the pulse train is generated. The existence of so many pulses hinders the temporal resolution that one could obtain from attosecond pulses in some experiments. To overcome this, a few different methods are used to isolate an attosecond pulse [12--19]. All of them are based on the fact that there is a one-to-one correspondence between the number of zero crossings of the generating field and the number of pulses in the pulse train. For example, one method is to allow only one of those zero crossing events to generate harmonics. This is achieved by taking advantage of the fact that the electrons have to return to the parent ion for the mechanism to take place. If the polarization of the generating field is not linear, the recombination probability reduces to zero. Therefore, a pair of partially overlapping, counter-rotating, circularly polarized pulses are used as a driving field, allowing for only one linear polarization zero crossing to happen. This is called polarization gating. The method used during the present work takes advantage of the relation between driving field strength and resulting harmonic frequency. If a few-cycle pulse is used for the harmonic generation, the consecutive maxima of the field strength of the driving pulse will be significantly different. If the pulse is also carrier stable, the case where only one field maximum can be selected (cosine pulse). In this case, there will only be one pulse generated containing the highest frequencies and a proper reflective mirror can be used to reflect only the highest frequencies. This is the spectral filtering and allows for a tunable setup, where different XUV frequencies can be selected to fit the needs of the experiment.

2.5 Description of Pulses

As described above, a superposition of harmonics gives rise to temporally localized spikes. Although such spikes can have many shapes or forms, the main source of such spikes is pulsed lasers. The outputting shapes are commonly characterized by simple shapes such as *Sech*, *Sinc*, *Lorenzian*, or *Gaussian*. Nevertheless, any pulse in the time domain can be described mathematically as:

$$P(t) = A(t)e^{\mathrm{i}(\omega_0 t)} \tag{2.21}$$

where A is the complex envelope, ω_0 the central frequency. In addition amplitude $|A|$ and a phase ϕ for A can be defined. Replacing back to Equation 2.21 yields:

$$P(t) = |A(t)|e^{\mathrm{i}(\omega_0 t + \phi(t))} \tag{2.22}$$

The temporal intensity profile of the pulse is defined as:

$$I = |P(t)|^2 \tag{2.23}$$

By Fourier transforming the pulse, the expression in the spectral domain is derived:

$$V(\mathrm{v}) = \int P(t)e^{-\mathrm{i}2\pi \mathrm{v}}\mathrm{dv} = |V(\mathrm{v})|e^{\mathrm{i}\psi(\mathrm{v})} \tag{2.24}$$

where ψ is the spectral phase, just as described above. The spectral intensity, which is what detectors record, is defined as:

$$S(\mathrm{v}) = |V(\mathrm{v})|^2 \tag{2.25}$$

The finer details of a pulse are represented in the phase term whether in spectral or temporal domain. In order to analyze what contributions are hidden in the phase term, a Taylor expansion on the phase term in time around zero can be atempted:

$$\phi(t) = \phi(0) + \frac{\mathrm{d}\phi}{\mathrm{d}t}t + \frac{1}{2}\frac{\mathrm{d}^2\phi}{\mathrm{d}t^2}t^2 + \cdots \tag{2.26}$$

In order to understand what these terms mean, it is worth considering how they would affect a sine or cosine function if they were introduced in the arguments. The zeroth order term is a shift in the phase and in some contexts it can be percieved as a time shift. The second term would result in a static change in the frequency. The following terms would result in an ever more intense, time-dependent change of the frequency. These terms are called chirp.

At this point a solid understanding of the classical nature of light, its main properties and behaviors and a mathematical description fitting for this thesis should be established. Readers are welcome to consult further sources to increasing their understanding and gaining further insight on the matter.

Chapter 3

Light-Matter Interactions

As described in the previous chapter, light is an oscillation of the electromagnetic field. As such, it is only reasonable that light can act on matter, since the latter is composed of electrically charged particles. Before one can really understand light matter interactions, a firm understanding of the framework on which matter is described most accurately needs to be established. This framework is no other than quantum mechanics.

In this section, a brief overview of the fundamentals of quantum mechanics will be presented. Although the reader is expected to have a firm understanding already, it is necessary to emphasize on the context under which most of this work was carried out. Once the used framework has been explained, some more advanced concepts will be demonstrated, such as perturbation theory and quantization of light, which will add to the picture of light. By the quantization of light all phenomena related to the quantum nature of light can be explained. Unfortunately, most of these phenomena are of no direct relevance to this work, so the concept will only be touched upon. As a last step, a way of including interactions of a quantum system with the environment will be presented. By including all of the above, a solid framework for describing light-matter interactions will have been established. This chapter is based on the following sources [20--27].

3.1 Quantum Description of Matter

In the late 19^{th} and early 20^{th} century, the study of a number of phenomena proved that classical physics had reached its limit. Such phenomena were for example the black body radiation (1900), the photoelectric effect (1905), atomic spectra (1911), and the Compton effect (1921). Corrections and assumptions were made to the classical picture of the atomic nature which provided a solution to the above. In 1923, it was understood that all of the assumptions and corrections were pointing to the same underlying physical principle which was the wave-particle

duality. This principle was in complete disagreement with the principles of classical physics. The basic idea behind it is that in a small scale, everything behaves both as wave and as particle. The following equations bridge those previously incompatible natures.

$$E = hf, \qquad p = \frac{h}{\lambda} \tag{3.1}$$

or

$$\omega = 2\pi f, \qquad k = \frac{2\pi}{\lambda} \tag{3.2}$$

and it's also defined $\hbar = \frac{h}{2\pi}$, which makes the equations above:

$$E = \hbar\omega, \qquad p = \hbar k \tag{3.3}$$

3.1.1 Schrödinger's Equation

The final formulation of the new physics that was being born during that era came from Erwin Schrödinger who derived the famous Schrödinger equation (1925):

$$i\hbar\frac{\partial\psi}{\partial t} = \hat{H}\psi \tag{3.4}$$

where ψ is the so called wavefunction and $\hat{H}$ is in the Hamiltonian of the system. In the most general case, the Hamiltonian is given by:

$$\hat{H}\psi = \left(-\frac{\hbar^2}{2m}\nabla^2 + V\right)\psi \tag{3.5}$$

and for completeness it should also be written:

$$-\frac{\hbar^2}{2m}\nabla^2\psi = \frac{p^2}{2m}\psi \tag{3.6}$$

It is common ground in classical mechanics that the Hamiltonian of a system is nothing more than the sum of its energy. Equation 3.5 clearly dictates a sum of the system's kinetic and potential energy respectively.

3.1.2 Statistical explanation

The meaning and nature of the wavefunction was and still is debated heavily. The standard interpretation is the so-called Copenhagen interpretation. Irrespective of the interpretation though, the calculation and the results coming out of the mathematical theory are the same. It is indeed agreed upon that the absolute squared value of ψ gives the probability density.

$$P(x) = |\psi(x)|^2 = \psi^*(x)\psi(x) \tag{3.7}$$

It goes without saying that, the sum of all probabilities along x should add up to one.

$$\int_{-\infty}^{+\infty} |\psi(x)|^2 \, dx = 1 \tag{3.8}$$

If that is not the case, the wavefunction can be divided by a constant to reduce the amplitude so that this holds true.

$$\begin{aligned} &\int_{-\infty}^{+\infty} |\psi(x)|^2 \, dx = N \\ &\Rightarrow \frac{\psi^*(x)\psi(x)}{N} = 1 \\ &\Rightarrow \psi'^*(x)\psi'(x) = 1 \\ &\Rightarrow \psi'(x) = \frac{1}{\sqrt{N}}\psi(x) \end{aligned}$$

This doesn't change the physics of the system, but helps preserve a statistical overview.

3.1.3 Operators

In quantum mechanics, it is often the case that a physical quantity is described as a set of operations on the wavefunction rather than functions. Take the example of the Hamiltonian:

$$\hat{H} = -\frac{\hbar^2}{2m}\nabla^2 + V$$

or what earlier defined as momentum:

$$\hat{p} = i\hbar\nabla$$

It is obvious that such quantities have no physical meaning unless they operate on a function. Then they will modify the initial and produce a new function, which hold the information of what is to be calculated. Such quantities are called operators.

In quantum mechanics, any observable can be written as an operator ($\hat{A}$) and obtaining the expectation value of that operator is mathematically translated to:

$$\left\langle \hat{A} \right\rangle = \int_{-\infty}^{+\infty} \psi^*(x)\hat{A}\psi(x)dx \tag{3.9}$$

It can be seen from the above how this proceidure can fail in some cases, since any possible observable should be real, while the wavefunction and the operators are in principle complex, leading to complex-vaulued observables. On top of that, assuming a closed system, there is nothing guaranteeing that the total probability stays constant in later times, leading to probabilities of finding the said particle anywhere less or more than one, violating the conservation of matter and energy.

Both problems can be prevented if the operators used are properly selected. Such operators are called Hermitian and follow the equation:

$$\int_{-\infty}^{+\infty} \psi^*(x) \left(\hat{A}\psi(x)\right) dx = \int_{-\infty}^{+\infty} \left(\hat{A}\psi(x)\right)^* \psi(x)dx \tag{3.10}$$

The above equation poses restrictions in the form and shape of an operator. Later on, more intuitive ways for understanding Hermitianity will be presented.

3.1.4 Eigenvalue problem

At this point an investigation of Schrödinger's equation seems fit. The Schrödinger equation can be thought of as a partial differential equation that it is. If $\hat{H}$ is not time-dependent, separation of constants can be performed, by writing that $\Psi(x,t) = T(t)u(x)$. Isolating the spatial part then reads:

$$\hat{H}u(x) = Eu(x) \tag{3.11}$$

This is the eigenvalue problem and can be solved analytically or numerically if the right boundary conditions and a valid definition of $\hat{H}$ are given. In general, though, the properties of the solutions of the eigenvalue problem are known. The functions $(u_i(x))$ that satisfy such a problem are called eigenfunctions and are:

1. Orthogonal $\int_{-\infty}^{+\infty} u_i^*(x)u_j(x) = \delta_{ij}$
2. Complete $g(x) = \sum_i a_i u_i(x)$

otherwise called orthonormal. Each eigenfunction $u_i(x)$ is a solution of the equation only for a specific eigenvalue E_i. First and foremost it is worth mentioning that the solutions are discrete. Surely the end solution can be any linear combination of the eigenfunctions as described by the completeness of the solutions, but this depends on the specific details of the problem (boundary and initial conditions).

3.1.5 Matrix form and Dirac formalism

Combining the above, the eigenvalue problem can be rewritten as:

$$\left\langle \hat{H} \right\rangle_{ij} = \int_{-\infty}^{+\infty} u_i^*(x) \left(\hat{H} u_j(x) \right) dx = E_j \int_{-\infty}^{+\infty} u_i^*(x) u_j(x) dx = E_j \delta_{ij} \tag{3.12}$$

This directly reveals the working principles of the operators as well as their matrix nature which will prove to be a very intuitive tool.

Let the complete solution of the system be $\psi(x) = \sum c_i u_i(x)$. The operators themselves can thus be depicted as 2D matrices with elements $\hat{A}_{ij}$ and the solutions as vectors (1D matrices) describing how much of each eigenfunction they contain (c_i). The eigenvalue problem can then be written as:

$$\begin{pmatrix} A_{11} & \dots & A_{1n} \\ \vdots & \ddots & \\ A_{n1} & & A_{nn} \end{pmatrix} \cdot \begin{pmatrix} c_1 \\ \vdots \\ c_n \end{pmatrix} = \hat{A} \begin{pmatrix} c_1 \\ \vdots \\ c_n \end{pmatrix}$$

where ψ is denoted as a $(n \times 1)$ matrix. If in the same manner ψ^* is written as a $(1 \times n)$ matrix, and by multiply it from the left the expectation value of $\hat{A}$ can be obtained:

$$\left\langle \hat{A} \right\rangle = \begin{pmatrix} c_1^* & \dots & c_n^* \end{pmatrix} \cdot \hat{A} \cdot \begin{pmatrix} c_1 \\ \vdots \\ c_n \end{pmatrix} = \begin{pmatrix} c_1^* & \dots & c_n^* \end{pmatrix} \cdot \begin{pmatrix} A_{11} & \dots & A_{1n} \\ \vdots & \ddots & \\ A_{n1} & & A_{nn} \end{pmatrix} \cdot \begin{pmatrix} c_1 \\ \vdots \\ c_n \end{pmatrix}$$

which gives:

$$\begin{pmatrix} c_1^* & \dots & c_n^* \end{pmatrix} \cdot \begin{pmatrix} \sum_{j=1}^{n} A_{1j} c_j \\ \vdots \\ \sum_{j=1}^{n} A_{nj} c_j \end{pmatrix} = \sum_{i=1}^{n} \sum_{j=1}^{n} A_{ij} c_i^* c_j$$

In order to get a more meaningful result, the normalization needs to be implemented as well:

$$\sum_{i=1}^{n} |c_i|^2 = 1$$

Then the orthogonality can be introduced as:

$$c_i^* c_j \Rightarrow c_i^* c_j \delta_{ij}$$

That is because the terms with c_i were denoted, but the fully correct term contains the eigenfunctions and an integral of them across x. The expectation value of $\hat{A}$ then reads:

$$\left\langle \hat{A} \right\rangle = \sum_{i=1}^{n} A_{ii} \left| c_i \right|^2$$

In this form of the operators, it is much easier to show that a Hermitian operator is one that follows the relation:

$$A_{ij} = A_{ji}^* \tag{3.13}$$

Another very important and useful formalism, that is based on the matrix properties of the operators and wavefunctions is the Dirac formalism. Let's assume the eigenvalue problem of the

operator $\hat{A}$:

$$A\left|n\right\rangle = a_n\left|n\right\rangle \tag{3.14}$$

in which the wavefunctions is written as ket, i.e.:

$$\psi = \left|\psi\right\rangle = \sum c_n\left|u_n\right\rangle = \sum c_n\left|n\right\rangle, \text{ where } c_n = \langle n|\psi\rangle \tag{3.15}$$

and the complex conjugates as bra:

$$\psi^* = \langle\psi| = \sum c_n^*\langle u_n| = \sum c_n^*\langle n| \tag{3.16}$$

Whenever a bra and a ket meet, from left to right in that order, a bra-ket is made:

$$\langle\phi|\psi\rangle = \int \phi^*\psi dr^3 \tag{3.17}$$

If a ket meets a bra in that order, then an operator is formed. In practice one can write the operator $\hat{A}$ as:

$$A = \sum a_n\left|n\right\rangle\langle n| \tag{3.18}$$

And when an operator meets a ket, or a bra meet an operator, the operator acts on the vector.

$$A\left|\psi\right\rangle = \sum_n a_n\left|n\right\rangle\langle n|\cdot\left|\psi\right\rangle = \sum_n a_n\left|n\right\rangle\langle n|\psi\rangle = \sum_n a_n c_n\left|n\right\rangle \tag{3.19}$$

The expectation value of the operator can be found by multiplying from the left Equation 3.19 with $\langle\psi|$:

$$\langle A\rangle = \langle\psi|A\left|\psi\right\rangle = \langle\psi|\cdot\sum_n a_n c_n\left|n\right\rangle = \sum_n a_n c_n\langle\psi|n\rangle = \sum_n a_n c_n c_n^* = \sum_n a_n\left|c_n\right|^2 \tag{3.20}$$

3.1.6 Density matrix

Based on the matrix form of the operators and the vector form of the wavefunction, a new matrix can be defined, such that it holds all of the information of the wavefunction that would prove to be a useful tool in the case of statistical mixtures. This matrix is defined as:

$$\rho \equiv |\psi(\vec{r})\rangle \langle\psi(\vec{r})| \tag{3.21}$$

In order to investigate the properties and the intuitive nature of this matrix, it would be advisable to limit ourselves to a simple two level system. In that case, the density matrix can be written as:

$$\rho = |c_1|^2 |1\rangle \langle 1| + |c_2|^2 |2\rangle \langle 2| + c_1 c_2^* |1\rangle \langle 2| + c_2 c_1^* |2\rangle \langle 1| \tag{3.22}$$

Or in matrix form:

$$\rho = \begin{pmatrix} |c_1|^2 & c_1 c_2^* \\ c_2 c_1^* & |c_2|^2 \end{pmatrix} = \begin{pmatrix} \rho_{11} & \rho_{12} \\ \rho_{21} & \rho_{22} \end{pmatrix} \tag{3.23}$$

It should be noted that the diagonal elements give the probability for the system to be in the respective state, while the trace of the matrix has to be equal to one due to the conservation of probability. The off-diagonal elements relate with the coherence of the respective states. The expectation value of any operator $\hat{Q}$ will be given by:

$$\left\langle \hat{Q} \right\rangle = Tr\left[\rho \hat{Q}\right] \tag{3.24}$$

Finally, it is important to reformulate the time dependent Schrödinger's equation to show the time evolution of the density matrix:

$$i\hbar \frac{\partial}{\partial t} |\psi\rangle = H |\psi\rangle \quad \text{and} \quad -i\hbar \frac{\partial}{\partial t} \langle\psi| = H \langle\psi| \tag{3.25}$$

$$i\hbar \frac{\partial \rho}{\partial t} = i\hbar \left[|\dot{\psi}\rangle \langle\psi| + |\psi\rangle \langle\dot{\psi}| \right] = \left[H |\psi\rangle \langle\psi| - |\psi\rangle \langle\psi| H \right] \tag{3.26}$$

$$\Rightarrow i\hbar \frac{\partial \rho}{\partial t} = [H, \rho] \tag{3.27}$$

Equation 3.27 is called the master equation and it is a very useful tool. It is the basis of all models developed during this work.

3.2 Perturbation theory

Let there be an atom who's unperturbed Hamiltonian is given by:

$$H_0 = -\frac{\hbar^2}{2m}\nabla^2 + V(\vec{r}) \tag{3.28}$$

The solution of the Schrödinger equation will be in the form of:

$$\psi_n(\vec{r},t) = u_n(\vec{r})e^{-i\omega_n t} \tag{3.29}$$

The complete solution will be a linear superposition of the eigenfunctions

$$\Psi(\vec{r},t) = \sum_n C_n\psi_n(\vec{r},t) = \sum_n C_n u_n(\vec{r})e^{-i\omega_n t} \tag{3.30}$$

where C_n is the probability amplitude for the atom to be in the $|n\rangle$ eigenstate. Let the atom be perturbed slightly, such that the Hamiltonian of the system will be given by:

$$H = H_0 + \mathcal{V} \tag{3.31}$$

where $\mathcal{V}$ is the perturbation Hamiltonian (in other words the energy of interaction). If the interaction is small with respect to the unperturbed Hamiltonian, the wavefunction can be written as a sum of the unperturbed eigenfunctions with time dependent probability amplitudes.

$$\Psi(\vec{r},t) = \sum_n C_n(t)u_n(\vec{r})e^{-i\omega_n t} \tag{3.32}$$

Replacing the above in the time dependent Schrödinger equation gives:

$$\sum_n \left[\hbar\omega_n C_n(t) + i\hbar\frac{dC_n}{dt}\right] u_n(\vec{r})e^{i\omega_n t} = \sum_n \left(\hbar\omega_n + \mathcal{V}\right) C_n(t)u_n(\vec{r})e^{-i\omega_n t} \tag{3.33}$$

By multiplying with $u_m^*(\vec{r})e^{i\omega_m t}$ and using the orthogonality relation $\int u_n^*(\vec{r})u_m(\vec{r})d^3r = \delta_n m$ the equation of motion for the probability amplitudes can be derived:

$$\frac{dC_m(t)}{dt} = -\frac{i}{\hbar}\sum_n \mathcal{V}_{mn}e^{i\omega_{mn}t}C_n(t) \tag{3.34}$$

where $\omega_{mn} = \omega_m - \omega_n$ and $\mathcal{V} = \int u_m^*(\vec{r})\mathcal{V}u_n(\vec{r})d^3r$ being the mn element of the interaction Hamiltonian. The physical meaning of this equation is that the perturbation is causing coupling between the different probability amplitudes, causing the atom to transition from one state to another.

3.2.1 Time independent perturbation

If $\mathcal{V}$ is independent of time, and the system was initially in the state $|i\rangle$, the equation of motion for the probability amplitudes can be written as:

$$\frac{dC_n(t)}{dt} = -\frac{i}{\hbar}\mathcal{V}_{ni}e^{i\omega_{ni}t} \tag{3.35}$$

Integrate the above gives the solution:

$$C_n(t) = -\frac{i}{\hbar}\mathcal{V}_{ni}\frac{e^{i\omega_{ni}t}-1}{i\omega_{ni}} = -\frac{i}{\hbar}\mathcal{V}_{ni}\frac{\sin\left(\omega_{ni}t/2\right)}{\omega_{ni}/2} \tag{3.36}$$

The probability of transitioning from state $|i\rangle$ to $|n\rangle$ is

$$|C_n(t)|^2 = \frac{|\mathcal{V}_{ni}|^2}{\hbar^2}\frac{\sin^2\left(\omega_{ni}t/2\right)}{\left(\omega_{ni}/2\right)^2} \tag{3.37}$$

This equation makes obvious that the probability of transitioning is periodic in time, causing the system to transition back and forth between the system's eigenstates.

3.2.2 Time dependent perturbation

One of the most common cases will be investigated, where $\mathcal{V} = \mathcal{V}_0\cos\left(\omega t\right) = \mathcal{V}_0\frac{1}{2}\left[e^{i\omega t} + e^{-i\omega t}\right]$. Just as before, it is assumed that initially, the system is in the state $|i\rangle$. Equation 3.34 can

now be written as:

$$\frac{dC_n(t)}{dt} = -\frac{i}{2\hbar}\mathcal{V}_{0,ni}\left[e^{i(\omega_{ni}+\omega)t} + e^{i(\omega_{ni}-\omega)t}\right] \tag{3.38}$$

Integration of the above results in:

$$C_n(t) = -\frac{i\mathcal{V}_{0,ni}}{2\hbar}\left[\frac{e^{i(\omega_{ni}+\omega)t}-1}{i\left(\omega_{ni}+\omega\right)} + \frac{e^{i(\omega_{ni}-\omega)t}-1}{i\left(\omega_{ni}-\omega\right)}\right] \tag{3.39}$$

The two terms are describing oscillations in different frequencies and are called anti-resonant and resonant terms respectively. In the case where $\omega_{ni} > 0$ and $\omega_{ni} \approx \omega$ the anti-resonant term is vanishingly small with respect to the resonant term and is ignored. This is called the Rotating Wave Approximation (RWA). In such a case, the transition probability is given by:

$$|C_n(t)|^2 = \frac{|\mathcal{V}_{0,ni}|^2}{4\hbar^2}\frac{\sin^2\left(\omega_{ni}-\omega\right)t/2}{\left[\left(\omega_{ni}-\omega\right)/2\right]^2} \tag{3.40}$$

3.2.3 Transitions to continuum and Fermi's golden rule

As discussed in the introduction, if the particle has energy higher than the binding potential energy of the atom, the electron will find itself in an unbound state. There is no quantization in the number of such states and hence, the energy spectrum of an electron in such case will be continuous. Assuming the perturbation frequency to correspond to an energy ($\hbar\omega$) higher than the atom's binding potential, the electron will have to transition to a continuum of unbound states. One important parameter in such a case is the density of states (DOS) $D(\nu)$ which describes number of states per unit of energy (or frequency). Such a quantity can be calculated for each individual case. The total probability for transition will be given by:

$$P_{total} = \sum_n |C_n(t)|^2 \to \int_\nu D(\nu)\,|C(\nu)|^2\,d\nu = \int_\nu D(\nu)\frac{|\mathcal{V}_0(\nu)|^2}{4\hbar^2}\frac{\sin^2\left(\nu-\omega\right)t/2}{\left[\left(\nu-\omega\right)/2\right]^2}d\nu \tag{3.41}$$

or more conveniently:

$$P_{total} = \int_\nu D(\nu)\frac{|\mathcal{V}_0(\nu)|^2}{4\hbar^2}t^2\left[\frac{\sin\left(\nu-\omega\right)t/2}{\left(\nu-\omega\right)t/2}\right]^2 d\nu$$

For $t \ll 2/(\nu - \omega)$ the term $[sinx/x]^2$ is close to unity and hence:

$$P_{total} \approx t^2 \int D(\nu) \frac{|\mathcal{V}_0(\nu)|^2}{4\hbar^2} d\nu \tag{3.42}$$

On the other hand, for $t \gg 2/(\nu - \omega)$ and, keeping in mind that the term $\left[\frac{\sin(\nu-\omega)\,t/2}{(\nu-\omega)\,t/2}\right]^2$ behaves like $\pi\delta(\nu - \omega)$,

$$P_{total} = \int_\nu D(\nu) \frac{|\mathcal{V}_0(\nu)|^2}{2\hbar^2} t \left[\frac{\sin(\nu-\omega)\,t/2}{(\nu-\omega)\,t/2}\right]^2 d(\nu t/2) = \frac{\pi}{2\hbar^2} D(\omega)|\mathcal{V}_0(\omega)|^2 t \tag{3.43}$$

What is most important in such cases, though, is the photo-current induced, which relates to the transition rate to the continuum.

$$\Gamma \equiv \frac{dP_{total}}{dt} = -\frac{d}{dt}|C_i(t)|^2$$

$$= \frac{\pi}{2\hbar^2} D(\omega)|\mathcal{V}_0(\omega)|^2 = \frac{\pi}{2\hbar} D(E)|\mathcal{V}_0(E)|^2 = \frac{2\pi}{\hbar} D(E)|\mathcal{V}(E)|^2 \tag{3.44}$$

where the following relation has been used:

$$D(\omega)d\omega = D(E)dE = D(E)\hbar d\omega \rightarrow D(\omega) = D(E)\hbar$$

Equation 3.44 is Fermi's golden rule describing the photoelectric effect and it is a very useful equation relating the photo-current with the intensity of the light $|\mathcal{V}(E)|^2$ for single photon processes.

3.2.4 Perturbation theory using the density matrix formalism

All of the above can be derived using the density matrix formalism, which also allows for open quantum systems, greater flexibility and physical insight. Starting from Equation 3.27 the equation for the evolution of the density matrix elements can be derived.

$$\frac{\partial \rho_{nm}}{\partial t} = -\frac{i}{\hbar} \langle n| [H, \rho] |m\rangle =$$

$$= -\frac{i}{\hbar} \langle n| H\rho - \rho H |m\rangle =$$

$$= -\frac{i}{\hbar} \sum_k \left[\langle n| H |k\rangle \langle k| \rho |m\rangle - \langle n| \rho |k\rangle \langle k| H |m\rangle\right] =$$

$$= -\frac{i}{\hbar} \sum_k \left[H_{nk}\rho_{km} - \rho_{nk}H_{km}\right] = \tag{3.45}$$

In the Equation 3.45 a phenomenological terms for de-phasing and/or decay can be added.

$$\frac{\partial \rho_{nm}}{\partial t} = -\frac{i}{\hbar} \sum_k \left[H_{nk}\rho_{km} - \rho_{nk}H_{km}\right] + \frac{\Gamma_{nm}}{2}\left(\rho_{nm} - \rho_{nm}^{(eq)}\right) \tag{3.46}$$

where Γ_{nm} is the decay rate of the nm element. The term $\rho_{nm}^{(eq)}$ depicts the equilibrium value that the density matrix element should have. It is meant to limit the effect of the decay term. The decay terms for off-diagonal elements cause de-phasing by reducing the coherence between the states, while the diagonal elements reduce the probability of the system being in the specific state. Returning to the perturbation point of view, by replacing the Hamiltonian with Equation 3.31:

$$\frac{\partial \rho_{nm}}{\partial t} = -\frac{i}{\hbar} \langle n| \left[H_0, \rho\right] |m\rangle - \frac{i}{\hbar} \sum_k \left[\mathcal{V}_{nk}\rho_{km} - \rho_{nk}\mathcal{V}_{km}\right] + \frac{\Gamma_{nm}}{2}\left(\rho_{nm} - \rho_{nm}^{(eq)}\right)$$

The term with the commutator of the unperturbed Hamiltonian can be calculated as:

$$-\frac{i}{\hbar} \langle n| \left[H_0, \rho\right] |m\rangle = -\frac{i}{\hbar} \sum_k \left[H_{0,nk}\rho_{km} - \rho_{nk}H_{0,km}\right] =$$

$$= -\frac{i}{\hbar} \sum_k \left[\hbar\omega_n\delta_{nk}\rho_{km} - \rho_{nk}\hbar\omega_m\delta km\right] = -i\left(\omega_n - \omega_m\right)\rho_{nm} =$$

$$= -i\omega_{nm}\rho_{nm}$$

Replacing and rearranging results in:

$$\frac{\partial \rho_{nm}}{\partial t} = -i\omega_{nm}\rho_{nm} - \frac{i}{\hbar} \sum_k \left[\mathcal{V}_{nk}\rho_{km} - \rho_{nk}\mathcal{V}_{km}\right] + \frac{\Gamma_{nm}}{2}\left(\rho_{nm} - \rho_{nm}^{(eq)}\right) \tag{3.47}$$

The equation above can be numerically integrated for every case. It is possible to work the equations further by solving in perturbation orders. To do that, the unperturbed system can be calculated as:

$$\frac{\partial \rho_{nm}^{(0)}}{\partial t} = -i\omega_{nm}\rho_{nm}^{(0)} + \frac{\Gamma_{nm}}{2}\left(\rho_{nm}^{(0)} - \rho_{nm}^{(eq)}\right) \tag{3.48}$$

It is evident that the zeroth order perturbation is the equilibrium case $\rho_{nm}^{(0)} = \rho_{nm}^{(eq)}$, which gives:

$$\begin{aligned} \frac{\partial \rho_{nm}^{(0)}}{\partial t} &= -i\omega_{nm}\rho_{nm}^{(0)} \\ \rightarrow \left[\frac{\partial}{\partial t} + i\omega_{nm}\right]\rho_{nm}^{(0)} &= 0 \end{aligned} \tag{3.49}$$

All higher orders of perturbation can be calculated as:

$$\begin{aligned} \frac{\partial \rho_{nm}^{(i)}}{\partial t} &= -\left(i\omega_{nm} - \frac{\Gamma_{nm}}{2}\right)\rho_{nm}^{(i)} - \frac{i}{\hbar}\sum_k \left[\mathcal{V}_{nk}\rho_{km}^{(i-1)} - \rho_{nk}^{(i-1)}\mathcal{V}_{km}\right] \\ \rightarrow \left[\frac{\partial}{\partial t} + \left(i\omega_{nm} - \frac{\Gamma_{nm}}{2}\right)\right]\rho_{nm}^{(i)} &= -\frac{i}{\hbar}\sum_k \left[\mathcal{V}_{nk}\rho_{km}^{(i-1)} - \rho_{nk}^{(i-1)}\mathcal{V}_{km}\right] \\ \rightarrow \left[\frac{\partial}{\partial t} + \left(i\omega_{nm} - \frac{\Gamma_{nm}}{2}\right)\right]\rho_{nm}^{(i)} &= -\frac{i}{\hbar}\left[\mathcal{V}, \rho^{(i-1)}\right]_{nk} \end{aligned} \tag{3.50}$$

The complete solution would then be:

$$\rho_{nm} = \sum_{i=0} \rho_{nm}^{(i)} \tag{3.51}$$

Equations 3.49 and 3.50 form a system of equations that can be integrated directly, by estimating up to which order one has to solve. The advantage of having the response organized in orders, makes the investigation in the field of nonlinear optics very convenient, where the nonlinear effects are categorized based on which perturbation order gives rise to them.

3.2.5 Electromagnetic Field as Perturbation

In all previous sections, it would be possible to include the interaction of the quantum system with radiation by assuming the electric field as a time dependent perturbation, as it was done in subsection 3.2.2, although not discussed in detail. The interaction Hamiltonian can be expressed in the dipole interaction picture, assuming a single electron, as:

$$\mathcal{V} = -\boldsymbol{\mu} \cdot \boldsymbol{E}(t) - \boldsymbol{\mu_B} \cdot \boldsymbol{B}(t) \tag{3.52}$$

where $\boldsymbol{\mu}$ is the electric dipole matrix, and $\boldsymbol{E}$ the electric field of the perturbing radiation, $\boldsymbol{\mu_B}$ is the magnetic dipole matrix, and $\boldsymbol{B}$ is the perturbing magnetic field. In the case of interactions with light, the magnetic field can be neglected in most cases, leaving us with:

$$\mathcal{V} = -\boldsymbol{\mu} \cdot \boldsymbol{E}(t) \tag{3.53}$$

Both quantities are vectors, which is important to keep in mind because not all possible and resonant transitions may take place if the subject system is not oriented properly within the field. The dipole matrix can be calculated as:

$$\boldsymbol{\mu}_{nm} = e \langle n | \boldsymbol{r} | m \rangle = e\boldsymbol{r_{nm}} \tag{3.54}$$

with e being the electron charge and $\boldsymbol{r}$ the position vector. The interaction Hamiltonian is then:

$$\mathcal{V} = -e\boldsymbol{r_{nm}} \cdot \boldsymbol{E}(t) \tag{3.55}$$

In this equation, the electric field has to be given as a real quantity, so if the definitions of chapter 2 for pulses is to be used, the complex conjugate term and the amplitude correction have to be included. If P as defined in Equation 2.22 and describes the electric field of a pulse, the correct replacement would be:

$$\mathcal{V} = -e\boldsymbol{r_{nm}} \cdot \left[\frac{\boldsymbol{P}(t) + \boldsymbol{P}(t)^*}{2}\right] = -\frac{e}{2}\boldsymbol{r_{nm}} \cdot [\boldsymbol{P}(t) + c.c.] \tag{3.56}$$

For multi-electron systems, the contribution of every electron has to be considered as:

$$\mathcal{V} = -\frac{e}{2}\sum \boldsymbol{r_{nm}^{(i)}} \cdot [\boldsymbol{P}(t) + c.c.] \tag{3.57}$$

where the index i runs over all electrons. For the rest of this work, the terms electric dipole matrix and dipole matrix will be used interchangeably, and the symbol $\boldsymbol{\mu}$ will be used whether it refers to multi- or single-electron systems, since in the multi-electron case a single matrix can

be calculated by summing up the single-electron matrices.

3.3 Quantization of Electromagnetic Fields

Up to this point, an accurate description of matter and its interaction with classical electromagnetic fields has been provided. As much as this can achieve, the limitations already became apparent in Section 3.2.4, where there was no other way to include de-phasing or relaxations without adding phenomenological terms, with no direct derivation from the master equation, since such effects are of purely quantum nature. In order for an electron to be able to make a leap from an excited state to a lower state, it needs to release a quanta of energy. The system described above, though, has no environment to interact with. On the other hand, noise is a doesn't exist classical mechanics, where everything is deterministic. However, the statistical nature of quantum mechanics inherently introduces noise, which in turn leads to coherence loss. In this section the quantum nature of light will be investigated. Bring together two quantum systems so that they can interact with one another will be shown. The reader is advised to refer to quantum mechanics books on the chapter of quantum harmonic oscillators for an understanding of the concepts and operators used in this section.

3.3.1 Electromagnetic Wave in Cavity

In order to expose the quantum nature of something, its freedom has to be limited. As it is the case for an electron that, without any limitations, finds itself within a continuum of states, while, when its position is confined by a potential well, the discretization of its states is revealed, so will be the case for the electromagnetic field. This is not a peculiar fact, but rather forcing the wave nature to reveal itself by forming standing waves.

Limiting the electromagnetic field can be easily achieved by confining the wave between two counter-facing reflectors, forming a cavity. A monochromatic field with circular frequency ω polarized in $\hat{x}$ direction and limited in $\hat{z}$ direction will be assumed. The length of the cavity would be L and the volume V. The describing field would then be:

$$\boldsymbol{E}(z,t) = q(t)\sqrt{\frac{2\omega^2}{\epsilon_0 V}}\sin(kz)\hat{x} \tag{3.58}$$

where q is the field's amplitude, $k = \omega/c = n(\pi/L)$ is the wavenumber. ϵ_0 is the vacuum permittivity. From Equation 2.1(vi) the magnetic field can be deduced:

$$\boldsymbol{B}\left(z,t\right)=\frac{\dot{q}(t)}{c^2k}\sqrt{\frac{2\omega^2}{\epsilon_0 V}}\cos(kz)\hat{y} \tag{3.59}$$

The electromagnetic energy density can be calculated as:

$$U_{EM}=\frac{1}{2}\left[\epsilon_0 E^2+\frac{B^2}{\mu_0}\right]=\frac{1}{V}\left[q^2\omega^2\sin^2(kz)+\dot{q}^2\cos^2(kz)\right] \tag{3.60}$$

The Hamiltonian would then be given by:

$$H=\int_0^L U_{EM}dL=\frac{1}{2}\left(\omega^2q^2+\dot{q}^2\right) \tag{3.61}$$

The resulting Hamiltonian is equivalent to that of a quantum harmonic oscillator with:

$$\left.\begin{aligned}a&=\tfrac{1}{\sqrt{2\hbar\omega}}\left(\omega q+i\dot{q}\right)\\ a^\dagger&=\tfrac{1}{\sqrt{2\hbar\omega}}\left(\omega q-i\dot{q}\right)\end{aligned}\right\} \tag{3.62}$$

where a, $a^\dagger$ are the destruction and creation operators. The number operator is also defined as $n=a^\dagger a$, which has an expectation value equal to the number of oscillators. The Hamiltonian can then be written as:

$$H=\hbar\omega\left(a^\dagger a+\frac{1}{2}\right)=\hbar\omega\left(n+\frac{1}{2}\right) \tag{3.63}$$

Hence the eigenfunctions of the electric field can be expressed as a number of quanta in this oscillation. Rewriting the electric field gives:

$$\boldsymbol{E}\left(z,t\right)=\sqrt{\frac{\hbar\omega}{\epsilon_0 V}}\left(a+a^\dagger\right)\sin(kz)\hat{x}=\mathcal{E}_\omega\left(a+a^\dagger\right)\sin(kz)\hat{x} \tag{3.64}$$

with $\mathcal{E}_\omega=\sqrt{\hbar\omega/\epsilon_0 V}$ the electric field amplitude per photon. Generalizing to polychromatic fields, the Hamiltonian can be written as a sum over the available frequencies.

$$H=\sum_s H_s=\sum_s\hbar\omega_s\left(a_s^\dagger a_s+\frac{1}{2}\right)=\sum_s\hbar\omega_s\left(n_s+\frac{1}{2}\right) \tag{3.65}$$

3.3.2 Propagating Electromagnetic Waves

For propagating electromagnetic waves one can write in general:

$$E(z,t) = \mathcal{E}_0 e^{i(kz-\omega t)} + \mathcal{E}_0^* e^{-i(kz-\omega t)} \tag{3.66}$$

Calculating the Hamiltonian as before by setting periodic boundary conditions for the integration:

$$H = \int \epsilon_0 E^2 dV = \epsilon_0 \left(\mathcal{E}^* \mathcal{E} + \mathcal{E}\mathcal{E}^*\right) \tag{3.67}$$

For the harmonic oscillator the Hamiltonian is:

$$H = \hbar\omega \left(a^\dagger a + \frac{1}{2}\right) = \frac{\hbar\omega}{2}\left(a^\dagger a + a a^\dagger\right) \tag{3.68}$$

Comparing the last two equations, the need to transform the complex electric field amplitude $\mathcal{E}$ into an operator related to the destruction operator becomes evident. By doing so, the following relations can be deduced:

$$\left.\begin{aligned} \mathcal{E}(t) &= \sqrt{\tfrac{\hbar\omega}{2\epsilon_0 V}}\, a e^{-i\omega t} \\ \mathcal{E}^*(t) &= \sqrt{\tfrac{\hbar\omega}{2\epsilon_0 V}}\, a^\dagger e^{i\omega t} \end{aligned}\right\} \tag{3.69}$$

The total electric field can now be written as:

$$E(z,t) = \sqrt{\frac{\hbar\omega}{2\epsilon_0 V}}\left[a_s e^{-i(\omega_s t - k_s z)} + a_s^\dagger e^{i(\omega_s t - k_s z)}\right] \tag{3.70}$$

It is worth noting that the result for propagating waves is reduced by a factor of $\sqrt{2}$ with respect to the result for standing waves in a cavity. That is because the standing waves are a sum of two counter-propagating waves and the energy density has to be double that of a propagating wave. Another interesting result is that the expectation value of the Hamiltonian for zero photons is still half a photon energy per frequency. Given that the electric field is not quantized in free space, and that there is a continuum of frequency states, that gives an infinite amount of energy being stored in the electric field of free space without it containing any photons at all.

Further investigation of the quantized electric fields can reveal numerous properties like the inherit noise, the photon distribution of different types of sources and more. These go beyond the scope of this work and will not be investigated here.

3.3.3 Interaction of Quantum Systems and Quantized Fields

A description of both a quantum system and a quantized electric field have been provided so far, and it is only natural to attempt to describe the interaction between the two. To do that, it is necessary to promote the operators from matrices to tensors. Tensor analysis is needed to achieve a strict mathematical description. An intuitive perspective can be maintained by assuming that, for a system which comprises of a number of subsystems, there may be operators that only act on a part of the system's wavefunction, which corresponds to the wavefunction of one of the subsystems. The total wavefunction of the system would be a multiplication (outer product) of the wavefunctions of the subsystem. For the purposes of this subsection, though, the operation will not be completed, so that the wavefunctions of the individual subsystems are easily tracked. Let the Hamiltonian of an unperturbed atom in a quantized electromagnetic field be, just like before:

$$H_a = \sum_{l,m} |l\rangle \langle l| H_a |m\rangle \langle m| = \sum_l \hbar\omega_l |l\rangle \langle l| \tag{3.71}$$

where $\hbar\omega_l$ are the atom's eigenenergies. The Hamiltonian of the quantized field has already been determined in the previous section and it was found to be:

$$H_f = \hbar\omega \left(a^\dagger a + \frac{1}{2}\right) \tag{3.72}$$

Lastly, it is important to define in this framework the interaction Hamiltonian. Starting from the interaction Hamiltonian defined in Equation 3.53, one can derive:

$$\mathcal{V} = -\mu E(t) = -\sum_{l,m} \mu_{lm} |l\rangle \langle m| \sum_s \mathcal{E}_s \left[a_s e^{-i(\omega_s t - k_s z)} + a_s^\dagger e^{i(\omega_s t - k_s z)}\right] \tag{3.73}$$

Admittedly, the interaction Hamiltonian may seem hard to interpret in this format, but with some reforming an intuitive form can be reached. First considering the nature of the dipole matrix, for atomic systems due to symmetry the diagonal elements are zero. This is not necessarily the case for molecular systems, but for the systems studyed here, the symmetry is enough to ensure that the diagonal elements are not contributing significantly. The interaction Hamiltonian

can thus be rewritten as:

$$\begin{aligned}\mathcal{V} &= -\sum_{l>m}\left(\mu_{lm}\left|l\right\rangle\left\langle m\right| + \mu_{lm}^{*}\left|m\right\rangle\left\langle l\right|\right)\sum_{s}\mathcal{E}_s\left[a_s e^{-i(\omega_s t-k_s z)} + a_s^{\dagger}e^{i(\omega_s t-k_s z)}\right] = \\ &= -\sum_{l>m,s}\left(\mu_{lm}\mathcal{E}_s\left|l\right\rangle\left\langle m\right| + \mu_{lm}^{*}\mathcal{E}_s\left|m\right\rangle\left\langle l\right|\right)\left[a_s e^{-i(\omega_s t-k_s z)} + a_s^{\dagger}e^{i(\omega_s t-k_s z)}\right] = \\ &= \sum_{l>m,s}\left(g_{lm,s}\sigma_{lm}^{+} + g_{lm,s}^{*}\sigma_{lm}^{-}\right)\left[a_s e^{-i(\omega_s t-k_s z)} + a_s^{\dagger}e^{i(\omega_s t-k_s z)}\right] \end{aligned} \tag{3.74}$$

where the operators $\sigma_{lm}^{+} = \left|l\right\rangle\left\langle m\right|$ and $\sigma_{lm}^{-} = \left|m\right\rangle\left\langle l\right|$ are defined as the generalized atomic raising and lowering operators. The factors $g_{lm,s} = -\mu_{lm}\sqrt{\frac{\hbar\omega}{2\epsilon_0 V}}$ are the generalized coupling factors between atom and field. For a set transition (set l and m) and frequency (set s) the interaction Hamiltonian describes four possible mechanisms, a rise of the atomic state by destruction of a photon, lowering of the atomic state by creation of a photon, increase of the atomic state by creation of a photon, and lowering of the atomic state by destruction of a photon. The last two mechanisms might sound strange since the existence of one of them alone would defy the conservation of energy. In reality the mechanisms do take place, but once one such transition has occured within a small time window, the counter mechanism will occur, ensuring that the energy is conserved. The time frame within which the counter mechanism will take place can be estimated from the uncertainty principle $\Delta E\Delta t \geq \hbar/2$. For a 800 nm transition (close to the fundamental wavelength of Ti:Sapphire lasers), the uncertainty principle dictates a time frame of approximately 0.2 fs for the counter mechanism to take place. These mechanisms will be more prominent when there is an abundance of photons. These terms are also called the anti-resonant terms. In the rotating wave approximation, the anti-resonant terms are neglected and the resulting interaction Hamiltonian becomes:

$$\mathcal{V} = \sum_{l>m,s}\left[g_{lm,s}\sigma_{lm}^{+}a_s e^{-i(\omega_s t-k_s z)} + g_{lm,s}^{*}\sigma_{lm}^{-}a_s^{\dagger}e^{i(\omega_s t-k_s z)}\right] \tag{3.75}$$

The total Hamiltonian can then be defined as the sum of the above contributions:

$$\begin{aligned} H &= H_a + H_f + \mathcal{V} = \\ &\sum_{l}\hbar\omega_l\left|l\right\rangle\left\langle l\right| + \sum_{s}\hbar\omega_s\left(a_s^{\dagger}a_s + \frac{1}{2}\right) + \sum_{l>m,s}\left[g_{lm,s}\sigma_{lm}^{+}a_s e^{-i(\omega_s t-k_s z)} + g_{lm,s}^{*}\sigma_{lm}^{-}a_s^{\dagger}e^{i(\omega_s t-k_s z)}\right] \end{aligned} \tag{3.76}$$

At this point in the discussion of theory, effects of spontaneous emission, coherence effects and much more are covered. By limiting the aforementioned system to two states and in-

vestigating the vacuum density of states of the electric field, one can reproduce the theory of Wiegner-Weisskopf for the spontaneous radiation. By limiting the radiation to a cavity, one will come to the Jaynes-Cummings model. Unfortunately, the calculation systems larger than the Jaynes-Cummings toy-model become tedious and unpractical as the number of states of the subsystems increase. This is because the number of states of the system would be equal to the product of the number of states of the subsystems. By including just two states for the field, the states of the complete system will double.

3.4 Interactions with the Environment

In the last subsection, a complete description of the quantum nature of light was given and the complete quantum mechanical approach for interactions of light and matter was shown. As is the case more often than not, the more detailed the description, the harder the calculations become. For the purposes of this work, the quantization of the electric field is only needed to allow for spontaneous emission to take place, implying that a more convenient way to include this mechanism needed to be found. The origin of spontaneous emission is known and it is an effect of the interaction of the system (that is of interest) with another system (which is otherwise irrelevant). In this section the perspective will be shifted, focusing on the energetics, describing the general interaction of the system with a reservoir that is considerably bigger than the system and with continuous spectrum, so that the decay time of the reservoir is very small.

3.4.1 System-Reservoir Interactions

The definition of the density matrix for the composite system is given by:

$$\hat{\rho} = \hat{\rho}^S \otimes \hat{\rho}^R \tag{3.77}$$

with $\hat{\rho}^S$ and $\hat{\rho}^R$ the reduced density matrices for the system (S) and the reservoir (R) respectively. The reduced density matrix of the system would be given at any time as:

$$\hat{\rho}^S = Tr_R\left[\hat{\rho}\right] \tag{3.78}$$

In general, tracing over R does not result in an R independent matrix, but if there is an operator $(\hat{T})$ acting only on the parameters of S, the expectation value of $\hat{T}$ would be:

$$\left\langle \hat{T} \right\rangle = Tr\left(\hat{\rho}^S \hat{T}\right) \tag{3.79}$$

Therefore the eigenvalue of such an operator depends only on the reduced density matrix of S. Starting from Equation 3.27, it can be shown that, for the composite system, the density matrix would be given as:

$$\frac{\partial \hat{\rho}}{\partial t} = \hat{\rho}_0 - \frac{i}{\hbar}\int_0^t \left[\hat{\mathcal{V}}\left(t'\right)\hat{\rho}\left(t'\right)\right] dt' \tag{3.80}$$

It should be borne in mind that R is infinitely bigger than S, so even if S dumps all of its energy into R, no significant change to the state of R will occur. Furthermore, at time zero, R is in equilibrium, which can be conveniently written as:

$$\frac{\partial \hat{\rho}^R}{\partial t} = 0 \tag{3.81}$$

The density matrix of Equation 3.80 can be substituted according to Equation 3.77. The trace over R can be taken to obtain:

$$\frac{\partial \hat{\rho}^S}{\partial t}\left(t\right) = -\frac{i}{\hbar} Tr_R\left[\hat{\mathcal{V}}\left(t\right), \hat{\rho}_0\right] - \frac{i}{\hbar^2}\int_0^t Tr_R\left[\hat{\mathcal{V}}\left(t\right), \left[\hat{\mathcal{V}}\left(t'\right), \hat{\rho}\left(t'\right)\right]\right] dt' \tag{3.82}$$

It is not surprising that, in the most general case, the reduced density matrix of S depends on the initial states of S and R, the type of interaction between them, as well as the evolution of S and R until the present time. If $\hat{\mathcal{V}}$ is linear in the S - R system (having multiplication of operators acting on S and operators acting on R) it can be deduced that the first term in the right hand side of Equation 3.83 will be zero. Assuming reasonably low coupling between S and R, as well as considering the size difference between S and R, the density matrix of the composite system can be assumed to be $\hat{\rho}\left(t'\right) = \hat{\rho}^S\left(t'\right)\hat{\rho}_0^R$, resulting in:

$$\frac{\partial \hat{\rho}^S}{\partial t}\left(t\right) = -\frac{i}{\hbar^2}\int_0^t Tr_R\left[\hat{\mathcal{V}}\left(t\right), \left[\hat{\mathcal{V}}\left(t'\right), \hat{\rho}^S\left(t'\right)\hat{\rho}_0^R\right]\right] dt' \tag{3.83}$$

where the state of S relates only to its past and the type of interaction with R. In practice, by invoking these assumptions, the description is being limited to the cases where R gets de-excited much faster with respect to the time that S needs to change its state significantly, which fits

the purposes of this work. The aim is to describe a quantized electric field in free space, where the photons escape the interaction volume technically instantly, leaving the field around the interacting atom or molecule in its initial state. Which limits any interaction of the excited R with S strictly around the present time (Markovian behaviour), which is translates to:

$$\frac{\partial \hat{\rho}^S}{\partial t}(t) = -\frac{i}{\hbar^2}\int_0^t Tr_R\left[\hat{\mathcal{V}}(t), \left[\hat{\mathcal{V}}(t'), \hat{\rho}^S(t)\,\hat{\rho}_0^R\right]\right] dt' \tag{3.84}$$

which is called the Redfield equation. By replacing $t' \to t - t'$ and extending the integration to infinity, the Born-Markov master equation can be deduced:

$$\frac{\partial \hat{\rho}^S}{\partial t}(t) = -\frac{i}{\hbar^2}\int_0^\infty Tr_R\left[\hat{\mathcal{V}}(t), \left[\hat{\mathcal{V}}(t-t'), \hat{\rho}^S(t)\,\hat{\rho}_0^R\right]\right] dt' \tag{3.85}$$

3.4.2 Interactions with a Markovian Reservoir

A more convenient form for the evolution of the reduced density matrix of S cannot be deduced without making some further assumptions about the type of interaction between S and R. A general and convenient case is considered here, where $\hat{\mathcal{V}} = \hat{A}\cdot\hat{B}$, with $\hat{A}$ acting only on S and $\hat{B}$ acting only on R. Both $\hat{A}$ and $\hat{B}$ are Hermitians and should be described as a linear superposition of promotion and demotion operators of S and R, with zero diagonal elements in the eigenvalue picture. The temporal evolution of $\hat{A}$ will be:

$$\hat{A}(t) = \sum_{i,j} e^{i\omega_i t}\,|i\rangle\, A\,\langle j|\, e^{-i\omega_j t} = \sum_{i,j} a_{ij} e^{i\omega_{ij} t} \tag{3.86}$$

while for $\hat{B}$ it will be:

$$\hat{B}(t) = \sum_k i\epsilon_k\left(b_k^\dagger e^{i\omega_k t} - b_k e^{-i\omega_k t}\right) = \sum_k \hat{\beta}_k(t) \tag{3.87}$$

Combining the above, the temporal evolution of $\mathcal{V}$ can be written as:

$$\hat{\mathcal{V}}(t) = \hat{A}(t)\cdot\hat{B}(t) = \sum_{i,j}\sum_k a_{ij}\hat{\beta}_k(t)\, e^{i\omega_{ij} t} \tag{3.88}$$

By replacing the above, Equation 3.85 would read:

$$\frac{\partial \hat{\rho}^S}{\partial t}(t) = \sum_{i,j,j',i'} \sum_{k,k'} e^{i\left(\omega_{i'j'} - \omega_{ij}\right)t} \Big[G_{kk'}(\omega_{ji}) \left(a_{ij} \hat{\rho}^S(t) a_{j'i'} - a_{j'i'} a_{ij} \hat{\rho}^S(t) \right) + \bar{G}_{kk'}(\omega_{ji}) \left(a_{j'i'} \hat{\rho}^S(t) a_{ij} - \hat{\rho}^S(t) a_{ij} a_{j'i'} \right) \Big] \tag{3.89}$$

where:

$$\begin{aligned} G_{kk'}(\omega_{ji}) &= \frac{1}{\hbar^2} \int_0^\infty e^{i\omega_{ji}t'} Tr_R \left(\hat{\beta}_{k'}(t) \hat{\beta}_k(t - t') \rho_0^R \right) dt' \\ \bar{G}_{kk'}(\omega_{ji}) &= \frac{1}{\hbar^2} \int_0^\infty e^{i\omega_{ji}t'} Tr_R \left(\hat{\beta}_k(t - t') \hat{\beta}_{k'}(t) \rho_0^R \right) dt' \end{aligned} \tag{3.90}$$

Further simplifying the above can be done by applying the rotating wave approximation (keeping terms with $\omega_{ji} = \omega_{j'i'}$) and setting:

$$\begin{aligned} G_{ij} &= \sum_{k,k'} G_{kk'}(\omega_{ji}) \\ \bar{G}_{ij} &= \sum_{k,k'} \bar{G}_{kk'}(\omega_{ji}) \end{aligned} \tag{3.91}$$

which results in:

$$\frac{\partial \hat{\rho}^S}{\partial t}(t) = \sum_{i,j} \Big[G_{ij} \left(a_{ij} \hat{\rho}^S(t) a_{ij}^\dagger - a_{ij}^\dagger a_{ij} \hat{\rho}^S(t) \right) + \bar{G}_{ij} \left(a_{ij}^\dagger \hat{\rho}^S(t) a_{ij} - \hat{\rho}^S(t) a_{ij} a_{ij}^\dagger \right) \Big] \tag{3.92}$$

The double summation can be reduced to a single sum by allowing $i > j$, in which case the terms need to be included with inverted indices. Then, only one index is practically needed, running over all available transitions. In turn, due to the symmetry of G_{ij} and $\bar{G}_{ij}$, although they are complex numbers, only the real parts ($\frac{\Gamma_i}{2}$) would survive the summation process. This parameter describes the rate at which the decay mechanism takes place.

$$\frac{\partial \hat{\rho}^S}{\partial t} = \sum_i \frac{\Gamma_i}{2} \left[2a_i \hat{\rho}^S a_i^\dagger - a_i^\dagger a_i \hat{\rho}^S - \hat{\rho}^S a_i^\dagger a_i + 2a_i^\dagger \hat{\rho}^S a_i - a_i a_i^\dagger \hat{\rho}^S - \hat{\rho}^S a_i a_i^\dagger \right] \Rightarrow$$

$$\Rightarrow \frac{\partial \hat{\rho}^S}{\partial t} = \sum_i \left[\mathcal{L}_i \hat{\rho}^S + \mathcal{L}_i^\dagger \hat{\rho}^S \right] \tag{3.93}$$

where it is defined:

$$\mathcal{L}_i \hat{\rho}^S = \frac{\Gamma_i}{2} \left(2a_i \hat{\rho}^S a_i^\dagger - a_i^\dagger a_i \hat{\rho}^S - \hat{\rho}^S a_i^\dagger a_i \right) \tag{3.94}$$

When this operator acts on a density matrix, it causes a decrease of probability in the present state and an equal increase of probability in the corresponding lower state. It describes the decay S due to the presence of R. On the contrary, the term $\mathcal{L}_i^\dagger \hat{\rho}^S$ describes the exact opposite flow of energy, where S gets excited from the presence of R. Due to the nature of the physical problem described here, the latter term needs to be neglected, resulting in the equation:

$$\frac{\partial \hat{\rho}^S}{\partial t} = \sum_i \mathcal{L}_i \hat{\rho}^S \equiv \hat{\mathcal{L}} \hat{\rho}^S \tag{3.95}$$

The operator $\hat{\mathcal{L}}$ is the Liouvillian and describes the non Hermitian dynamics of the system due to the coupling with a Markovian reservoir, as described above.

Returning to Equation 3.27 and adding the Liouvillian, the Lindblad master equation is deduced:

$$\frac{\partial \hat{\rho}^S}{\partial t} = -\frac{i}{\hbar} \left[\hat{H}_S, \hat{\rho}^S \right] + \hat{\mathcal{L}} \hat{\rho}^S \tag{3.96}$$

In the equation above, we can include all interactions described in previous sections, such as classical perturbations or coupling with other quantum systems, in the system's Hamiltonian, while any coupling to Bosonic Markovian fields can be included in the Liouvillian. It is also worth mentioning how the Liouvillian takes the place of the phenomenological terms included in Equation 3.46.

Chapter 4

Transient Absorption Study of Mg-Phthalocyanine Organic Semiconductor Systems

This chapter will present the transient absorption techniques and ways to utilize them to record the dynamics taking place in a material due to its interaction with light. It will also provide a brief description of the material that was studied and the new developments around it that motivated this study, as well as present the experimental results and what conclusions can be derived directly from them. Lastly, a way of modelling and simulating the dynamics by implementing and expanding on what was discussed in the previous chapters will be given.

This project was conceptualized by Iglev Hristo and the author. Major experimental efforts were made by Nuber Matthias, Schleltter Albert, Haimerl Michael and the author. The analysis of the transient absorption measurements in the mid-infrared (MIR) spectral range was conducted by Nuber Matthias. The experiments in the visible spectral range were performed by Schletter Albert and assisted by me, while the analysis and modelling were done by me. Other major contributors who made this project possible are Schnitzenbaumer Maximilian, Wörle Martin and Scigalla Pascal. Wagner I. Laura affiliated with the Walter Schotky Institute and the Physics department of TUM performed the XRD characterization of the films. The findings and the data of this work have originally been accepted for publishing in the Journal of Physical Chemistry C.

4.1 Transient Absorption Techniques

This section constitutes an overview of the concept of transient absorption techniques, and their value as a tool for studying optical systems. Then, a description of the two specific setups used during this study is provided.

4.1.1 Principles of Transient Absorption

Transient absorption is a pump-probe scheme, where an intense pulse is used to prepare the studied system into an excited state and a second pulse with much less intensity, but with a broad spectrum, is passed through the sample and then analyzed into its spectral components. By comparing such spectra from when the sample is excited or not, the extent to which the absorbance of the sample is affected by the exciting pulse can be deduced. A variable delay stage is used to adjust the delay between the pump and probe pulses, so that spectra can be recorded after different amount of time has passed from the excitation. By systematically doing so, a spectrogram can be obtained in which the dynamic response of the system is encoded for different frequencies from before excitation to relaxation.

In such systems, the pulses have to be selected in such a way that the pump pulse is intense enough and reasonably resonant to induce sufficient change on the system so that a response is strong enough to be recorded. On the other hand, if the pumping pulse is too intense, it can induce nonlinearities, sparking and optical damage to the sample, rendering the measurements useless. In the context of the previous chapter, the desired effect would be for the pulse to induce primarily first order perturbation on the system. The probe pulse should be selected in such a way that its intensity is not sufficient to induce any major effects on the sample, other than moving a few percents of the population, if any, for the absorption to happen. The spectrum of the pulse has to be selected in such a way that it is broad enough and within the spectral region of interest for the dynamics to be recorded. The duration of both pulses has to be as little as possible, given that, together with the quality and accuracy of the motors used, it will define the final temporal resolution of the experiment. To this end, it is easy to see why operating those techniques in the visible spectral range is the most common practice. In other words, very broad pulses that can be compressed down to sub-10 femtoseconds can be generated. This timescale is already enough to isolate the purely electronic contribution in the response of the sample. The downside is that short pulse duration implies broad spectrum according to the time-bandwidth product relation ($\Delta t \Delta f = 0.44$ for Gaussian pulses). This is desirable in the case of the probe pulse, but for maximizing the temporal resolution, the pump pulse would also have to be appropriately short. This greatly reduces the spectral selectivity in the excitation, implying that the system will have to be prepared in a statistical mixture of states, rather than

in a specific state.

The last thing that needs to be clarified about the transient absorption techniques is how the system dynamics are recorded onto the spectrogram. By following any textbook on light matter interaction, one would quickly come to the Beer-Lambert law:

$$I(z) = I_0 e^{-az} \tag{4.1}$$

where I is the radiation intensity along the propagation axis, I_0 the initial intensity, z the position where the equation is evaluated and depending on the level of the derivation or perspective of the textbook a would be the absorption coefficient, or it would appear together with the minus sign, usually with γ as its symbol, named small signal gain coefficient. No mater the name, it can be shown that the absorption coefficient relates with the state of a model two-level system with an equation such as:

$$\gamma(f) = -a(f) = N\sigma(f) = N\frac{\lambda^2}{8\pi\tau_{sp}}g(f) \tag{4.2}$$

where σ is the transition cross section, N is the population difference between the two states, λ is the wavelength associated with this transition, τ_{sp} is the spontaneous decay time constant and $g(f)$ is some line shape, usually Lorentzian, and f refers to the frequency under consideration. On the contrary, the absorbance, which is what is usually recorded in such experiments, can be defined as:

$$\begin{aligned} \frac{I}{I_0} = e^{-az} = 10^{-A} \rightarrow \\ \rightarrow A = \log_{10} e\, az \end{aligned} \tag{4.3}$$

replacing Equation 4.2 into the latter yields:

$$A(f) = -\log_{10} e\, z\frac{\lambda^2}{8\pi\tau_{sp}}g(f)N = -\log_{10} e\, z\sigma(f)N \tag{4.4}$$

in which it can be seen that the absorbance is directly related to the population difference between two levels of the system, the transition cross section (which also defines the absorption shape across the wavelengths) and the thickness of the sample. It is worth mentioning that this holds true only for a two level system. If a system has more than two levels, all possible

transitions have to be considered in the same manner. Still, this shows how recording the absorbance for different delay times records effectively the population difference between all available states at every time. The contribution of this technique lies on the fact that, by properly decoding the data one can virtually access the quantum state of the system and its temporal evolution.

4.1.2 Mid-Infrared Transient Absorption Setup

The first setup deployed for this study is a visible-pump MIR-probe technique, with the aim to investigate the dynamics that occur in the vibrational resonances, as well as probe free carriers and intraband dynamics in organic semiconductors. Most of these processes are not purely electronic and exist in the pico- to nanosecond timescales. As is the case in most optical setups nowadays, at the heart of the system lies a Ti:Sapphire oscillator generating pulses at 800 nm, with a repetition rate of 80 MHz and pulse duration down to 40 fs. The pulses are then amplified by a Ti:Sapphire regenerative amplification setup, which reduces the repetition rate to 1 kHz and increases the power and the duration of the pulses to 100 fs. These are used to generate both the pump and the probe pulses. Part of the pulses is being split and can either be used directly for pumping, or can be driven into a noncollinear optical amplifier (NOPA) system that is pumped by a frequency doubled part of the amplifier's output. Using the NOPA allows for tunable (within the visible range) wavelength of the pumping beam. Another part of the amplifier's output is driven into a two-stage near infrared (NIR) optical parametric amplifier (OPA) from which a tunable output can be obtained. The OPA output is then used together with another part of the amplifier's output to drive a difference frequency generation (DFG) process in a $AgGaS_2$ crystal. The resulting radiation lies in the MIR range and is used as a probe. The temporal resolution of the setup is estimated to be in the order of 1 ps and it is limited by the generation process of the MIR radiation.

In order to guarantee the quality of the results, the probe pulse is split into two parts. One passes through the sample and its spectrum is recorded directly, while the second passes through the sample at the same point where the pumping pulse is. This gives a reference to the spectrum changes of the probe pulse itself. Then a chopper wheel is placed in front of the sample, chopping every second pumping pulse, so that a reference to the unpumped system is taken at close intervals after the pumped spectrum is recorded.

4.1.3 Visible Transient Absorption Setup

As expected from the discussion in Section 4.1.1, investigating the purely electronic transitions demands a higher time resolution, which is easily achievable in the visible range. It is also

crucial for the development of optical devices to know the dynamics in the intended spectral range. Therefore, an visible-pump visible-probe setup was used.

As described before, the laser system is based on a Ti:Sapphire oscillator that feeds into a multi-pass Ti:Sapphire amplifier. The output is 800 nm pulses with a duration of 25 fs, a repetition rate of 3 kHz and a pulse energy of 1.2 mJ [28,29]. For spectral broadening purposes, the output beam is focused at the entrance of a hollow core fiber filled with neon (pressure of 1.7 bar). The output beam is re-collimated and, by a few reflections from a pair of chirped mirrors, the pulses are compressed down to sub-10 femtoseconds. A pair of glass wedges is used to fine-tune the dispersion of the pulses. The beam is split into two parts from which the pump and probe beams will be obtained. For the pump beam, the greater of the two parts can be directly used, or it can be frequency doubled by second harmonic generation (SHG) in a BBO crystal. A small fraction of the fiber's output can be used directly as the probe beam, as it is already broad enough to cover a good chunk of the visible spectrum. Adjusting the pressure of the fiber can slightly tune the spectra of both the pump and the probe beams. A combination of a motorized stage as well as a high precision piezo stage are used as a variable delay line to establish the required delay between the two pulses, and a collinear geometry is used in order to get the highest temporal resolution. Therefore, the two beams had perpendicular polarizations. This allows for the best separation of the two beams and minimization of pump radiation leakage into the recorded probe spectra. Just like the MIR-probe setup, a chopper wheel is used to block every second pump pulse to allow for an immediate recording of a reference spectrum.

4.2 Magnesium Phthalocyanine

In recent years there has been a great interest in organic semiconductors since they can be used in numerous modern day applications and offer an interesting alternative to established technologies. Perhaps one of the most iconic applications are the Organic Light Emitting Diode (OLED) displays which offer a unique color palette as well as deeper blacks than most competitive technologies. In addition, due to the soft nature of the organic semiconductor crystals, elastic and foldable displays can be created. Moreover, properties such as material availability, ease of synthesis, biocompatibility, low toxicity and even biodegradability only add to the list of desirable properties for electronic or optoelectronic devices.

Although there are many interesting organic molecules that can be used for such applications, the present work focuses on phthalocyanines (Pc). Phthalocyanines are a wide and diverse group of chemical complexes with many applications, from dyes to catalysts and from environment sensing to photoelectronic devices [30--35]. In its simplest form, phthalocyanine (H2Pc) is made of four isoindol groups, each connected to two other isoindol groups by two nitrogen atoms.

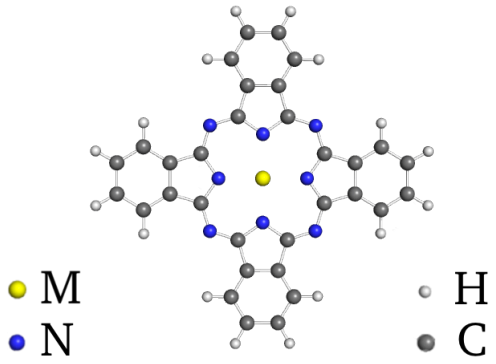

Figure 4.1: Phthalocyanine complex.

The resulting molecule with formula $(C_8H_4N_2)_4H_2$ is a two dimensional symmetric molecule that belongs to the D_{2h} point group. What makes Pcs intriguing, though, is their ability to substitute the central hydrogen atoms for a metal atom, forming metal phthalocyanines (MPc), or even a metal containing group forming greater complexes. This allows for tunability of the properties of MPcs as well as functionalization of the derivatives.

The main interest of this study was organic semiconductors, which implies that the high symmetry of MPc was essential to guarantee good crystal structure and properties. For instance, it is known that MPcs tend to self-assemble in neat monolayers when adsorbed on clean surfaces in vacuum [36, 37]. It is also known that good quality thin films of MPcs can be obtained with different preparation methods such as spin coating [38, 39], Lagmuir-Blogett [40--42] and vacuum vapor deposition [43, 44]. It was shown recently, that even single crystal magnesium phthalocyanine (MgPc) can be obtained [45] by following a new preparation method named liquid deposition [46], in which a solution of MgPc is deposited on top of an aqueous solution of a polymer, selected such that the surface tensions match, causing the deposited MgPc solution to spread over the whole surface of the polymer solution without mixing. The solvent of MgPc evaporates over time, leaving a crystalline MgPc film that can be fished and placed on any substrate.

The aforementioned development opened some new possibilities. MPc semiconductors of such quality were only obtainable in monolayers which, although useful, do not allow for the study of this material with visible and infrared light, due to the extremely low absorption. With this new preparation method, a possibility to study a crystalline MgPc with all transient absorption techniques available and use it as a benchmark against amorphous films that are obtainable by established manufacturing methods presented itself [47, 48].

4.2.1 Sample Preparations

As discussed above, the main objective of this study is to compare the transient absorption response of crystalline and amorphous MgPc semiconductor films. To do that, the liquid deposition technique was used as presented in the work of Ran et al. [45] to fabricate crystalline MgPc samples. The only difference in this manufacturing process was the use of a saturated solution of MgPc in dichloromethane (DCM) instead of the suggested concentrations, since the suggested concentrations would result in films that were practically transparent and were not usable. The resulting semiconductor crystals were fished and placed either on thin BaF_2 or CaF_2 windows. The reason for changing the windows was to best fit the needs of the transient absorption measurements. The amorphous samples were made by spin coating on BaF_2 or CaF_2 windows. A saturated solution of MgPc in DCM was used again. The windows were fixed on a rotating platform with rotation speeds of 5000 rpm, and a few drops were dropped at the center of the rotating window slow enough to allow for the previous drop to evaporate. After a few repetitions, a homogeneous thin film was formed on the window.

4.2.2 Characterizations

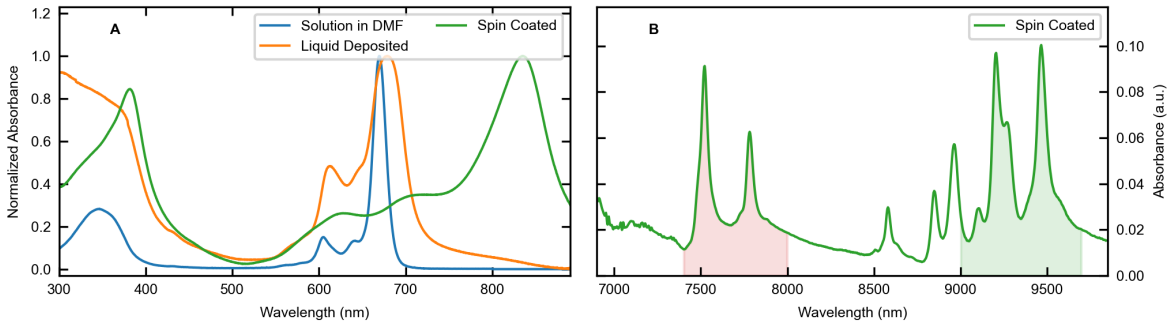

Figure 4.2: UV/VIS absorption spectra of crystalline and amorphous MgPc samples as well as solution of MgPc in N,N-Dimethylformamide (DMF)(A). The spectra have been normalized to allow for easy comparison. FTIR spectra of amorphous MgPc sample (B). Highlighted in red and green are the studied spectral regions with MIR transient absorption

The samples were characterised using steady state absorption techniques (UV/VIS, FTIR) as seen in Figure 4.2. The spectra on Figure 4.2A were normalized so that an easier comparison would be possible. A spectrum of a solution of MgPc in N,N-Dimethylformamide (DMF) with a concentration of 0.08 mg/ml is given. Nominal values for the absorption maxima are 1.26 $a.u.$ for the solution, 0.45 $a.u.$ for the liquid deposited and 0.71 $a.u.$ for the spin coated sample. It is

important to mention that there are major differences in the visible absorption spectra obtained from the different preparation methods, while the FTIR spectra are not different for the two methods and thus only one of them is presented here.

Understandably, the individual molecules stay rather unperturbed and isolated from one another in the solution. Although the solvent might induce some shift in the position of the absorption bands, this effect should be rather minor and the spectrum obtained should be rather close to what could be obtained from isolated molecules [49, 50]. Figure 4.2A illustrates the absorption of MgPc dissolved in DMF (blue line), which mainly contains two distinct spectral features. An absorption band from 700 to 600 nm named Q-Band and another absorption band centered around 350 nm (B- or Sorret Band). As the molecules come together to form a crystal, the bands are expected to slightly shift due to intermolecular interactions, as well as broaden due to the dispersion of the energy levels caused by the formation of a band structure [51]. In principle, well organized crystals of large organic molecules tend not to be densely packed. The crystal lattice constants tend to be in the order of ten Å resulting in dispersions of less that 0.5 eV (approximately 120 THz), so in principle the broadening effect should not be so dramatic [52]. This becomes obvious by comparing the absorption spectrum of the crystalline (liquid deposited) sample with the dissolved MgPc. There is a clear red shift of all peaks and a distinct broadening, but the effect is rather limited. It is easy to recognize that the two samples are made from the same material.

The situation changes when it comes to the amorphous (spin coated) sample (green line in Figure 4.2A). In this case, the distinct peaks within the Q-Band are severely broadened and even further red shifted. Furthermore, a new absorption peak has appeared around 820 nm. The strong broadening and redshift indicate tighter binding and distortions of the molecules that make up the crystal, as well as stronger intermolecular interactions. The near infrared peak has also been explained as an effect of strong exciton coupling between molecules that are situated perpendicular to each other forming X-like structures (so called X-phase) [53], which in turn lead to samller intermolecular distances and higher intermolecular excitonic coupling. This formation constitutes a side-effect of the preparation method and is not present, for example, in the vapor deposition method [53]. In the context of this study, the presence of this peak was instrumental, since the aim is to obtain and compare an organized lattice sample with the most disorganized one and compare the results.

In the case of FTIR spectra (Figure 4.2A), the origin of the absorption peaks observed are vibration modes of the different bonds present in the molecules [54]. Any intermolecular coupling effects have little to no effect on the vibrational modes since the core structure of the molecule is not drastically changed and the intermolecular distances are still greater than the interatomic distances within the molecule.

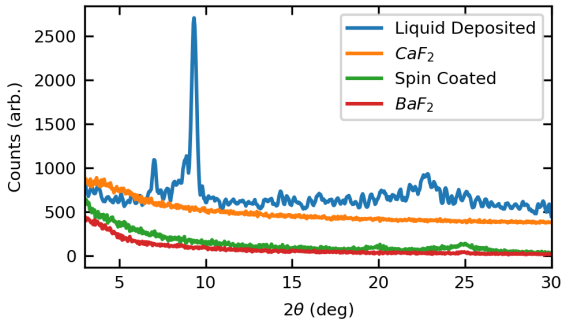

Figure 4.3: GI-XRD measurements of the liquid deposited sample (blue line), its substrate (orange line), the spin coated sample (green line) and its substrate(red line).

The structural properties of the fabricated studies were investigated using Grazing incidence X-ray diffraction (GI-XRD). Results from this study can be found in Figure 4.3. The feature-free nature of the spin coated sample is indicative of its amorphous nature. On the contrary, the liquid deposited sample exhibits a set of sharp peaks in its diffraction pattern, proving the crystallinity of the sample, as this is a typical behaviour of polycrystalline materials. An estimated grain size of 25 nm can be estimated using the Scherrer equation. The data recorded for the liquid deposited sample have been recorded with a small area beam of diameter 0.33 mm so as to have the probing beam localized only the coated areas of the film. This results in a decreased count rate. The data presented in Figure 4.3 have been scaled to overlap with the corresponding substrate (CaF_2), which increases the noise level as well. Then the data for the liquid deposited sample and its substrate have been offset by 350 counts for easier comparison of the spin coated sample and its substrate (BaF_2).

4.3 Intraband and Vibrational Dynamics of MgPc Semiconductors

An attempt to investigate and record any change in the structure of the MgPc molecules during photoexcitation and relaxation of MgPc molecules, as well as any intraband dynamics, was made by deploying a MIR transient absorption technique to probe the $7400 - 8000$ nm and $9000 - 9600$ nm spectral regions. This selection was made according to where vibrational resonances can be probed, as well as the expected dispersion of the valence band (estimated approximately 0.25 eV or otherwise wavelengths greater than 5000 nm) [52]. Some considerations of the limits of the technique also affected the decision of the probed spectral ranges. The samples were pumped with 600 nm and 800 nm pulses for the crystalline and amorphous samples respectively, exciting

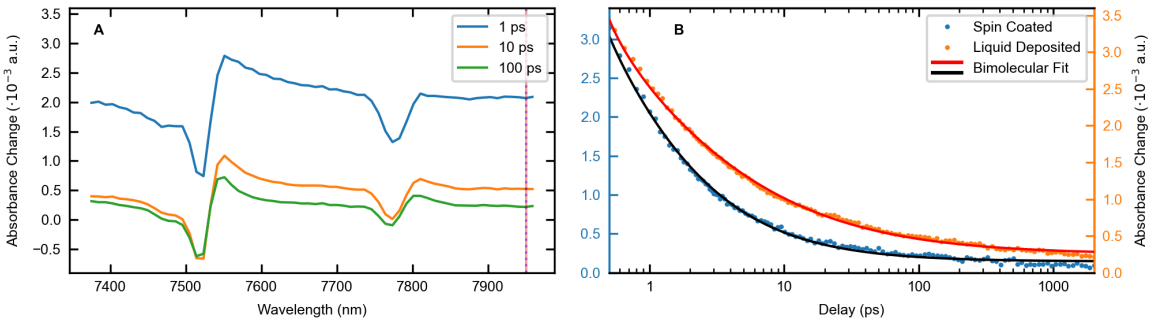

Figure 4.4: MIR transient absorption spectra recorded for different delays for the spin coated sample (A). The transient absorption signal at 7950 nm for the spin coated (blue dots) and liquid deposited (orange dots). Bimolecular fit for each is also displayed (solid lines). The inlay shows the same data on a log scale.

the samples to their lowest unoccupied molecular orbital (LUMO). The temporal resolution of the technique is estimated in the picosecond timescale and is limited by the DFG process, which generates the probe pulse.

In Figure 4.4A, typical transient absorption spectra for the liquid deposited sample are depicted. In both spectral regions and for both samples the observed effects were the same as the ones depicted here. A red shift of the observed vibrational resonances was always present, as seen by the "valley-peak" behaviour around the wavelengths where the vibrational resonances are located in the steady state FTIR spectra. This can be attributed to local increase of temperature as the sample absorbs energy from the exciting pulse, since the same effect can be induced by heating the sample. In Figure 4.5 FTIR spectra from the amorphous sample recorded at different temperatures are presented. A reference spectrum at 23 °C was subtracted from all spectra to reveal the same "valley-peak" behaviour. The FTIR spectra were recorded by heating the sample with a water heated sample holder, and the temperature was regulated by a thermostat. It can then be directly deduce that there is a temperature change of a few degrees happening locally on the sample when the exciting pulse hits.

The second effect that was observable is a uniform absorption increase across the entire spectral range under investigation. The origin of this effect is the opening of holes in the valence band (or the electrons occupying the conduction band) of the crystal as the material gets excited, which allows for intraband transitions within the valence and/or conduction bands. This is perceived as an absorption increase. Within the spectral ranges investigated here, there was no sign of specific resonances or any significant difference in the temporal evolution across wavelength for any sample, indicating that there are no significant effects of population moving

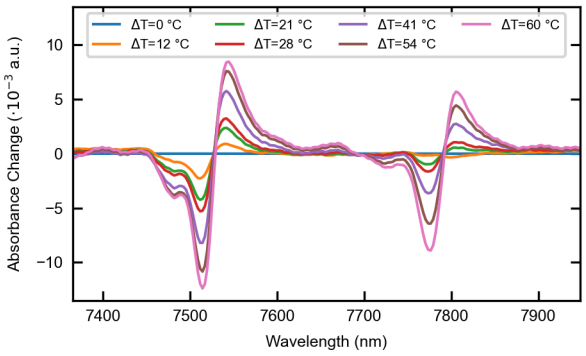

Figure 4.5: FTIR absorption change of the spin coated sample for different temperature settings. The reference was taken at 23 °C.

within the bands. The temporal evolution of the signal then can only depend on the relaxation mechanism of the first excited state, revealing the rate at which holes are being filled in the valence band.

It is already understood that the main relaxation mechanisms for MgPc films are of excitonic nature [45, 53, 55--57]. The temporal evolution of this transient absorption signal can be seen in Figure 4.4B for both crystalline and amorphous samples. Apparently, there is a significant difference in the relaxation dynamics between the two samples. The underlying mechanism has been studied elsewhere [58, 59]. The equation that relates the absorption change of a sample with the exciton density over time can be fitted in order to quantify the difference between the two samples. This is given by Equation 4.5 [58]:

$$\Delta A = \frac{A}{\frac{N}{n_0} + 2\gamma_0 N t^c} \tag{4.5}$$

where A relates to the absorption maximum and the exciton coefficients of the molecule in ground and excited state, n_0 is the initial exciton density, N is the molecule density, and γ_0 is the initial annihilation constant. Lastly, c is a parameter that relates to the dimensionality of the exciton annihilation process. In the recorded dataset, this was the main difference between the two samples. For the crystalline sample it was found to be 0.62, indicating an almost one dimensional exciton annihilation process, while for the amorphous sample had a value of 0.85, indicating higher dimensionality. The results are in good agreement with the well established understanding of how MgPc behaves. It is known that MgPc molecules tend to do π-stack, forming almost one dimensional columns where exciton coupling can happen between next neighbours up and down the stack. The crystalline sample consists predominantly of such

stacks and this is reflected in the dimensionality parameter of the relaxation mechanism. On the other hand in the amorphous MgPc, more configurations are present (as is evident by the X-phase absorption peak). The other molecule configurations allow for exciton dissipation along more directions, increasing the dimensionality of the annihilation mechanism. This is depicted by the increase of the dimensionality parameter.

4.4 Interband Dynamics of MgPc Semiconductors

Having gained a significant insight in the vibrational, intraband and relaxation dynamics taking place in MgPc semiconductors, a more detailed investigation of the interband transitions and the fast dynamics present can be attempted. For this to happen, a visible-pump visible-probe transient absorption setup was deployed, which can offer down to femtosecond timescale resolution. As the main interest is the interband dynamics this time, a decision was made to pump the system to higher excited states (B-Band), by pumping with 400 nm pulses generated by SHG of the laser's fundamental frequency in a BBO crystal, in order to be able to draw any conclusions possible about the decay times of the higher excited states as well. Combined with the fact that the samples have drastically different absorption spectra in the visible range, this severely complicates the situation. The probing was done by broadband pulses that are generated by propagating the laser's fundamental through a hollow core fiber, filled with Ne (pressure of 1.7 bar), so that self phase modulation (SPM) would occur and generate more frequencies. The resulting pulses were then temporally compressed by a set of chirped mirrors, bringing the duration down to a few femtoseconds. In this setup the temporal resolution is limited by the bandwidth of the probe pulse as well as the duration of the pump pulse (in this case due to the SHG process).

In Figure 4.6 typical transient absorption spectra recorded for the liquid deposited and spin coated samples are depicted. Although they differ in shape, Some patterns are easily identifiable. For instance, as can be seen in Figures 4.6A&B, the absorption increases wherever there were no absorption bands on the steady state spectra. Then, wherever there was an absorption maximum of the steady state spectra, there are absorption decreases present. In essence, these are the two main effects that can take place and they can overlap and cancel each other out or one can dominate and obscure the other. The increase of absorption is the excited state absorption (ESA) and the decrease of absorption, where there are absorption peaks in the steady state spectra, is the ground state bleaching (GSB).

Concerning the temporal evolution of the absorption signals (where some are shown in Figures 4.6C&D for the crystalline and amorphous sample respectively), it is obvious that the situation is significantly more complex than what was recorded for the MIR transient absorp-

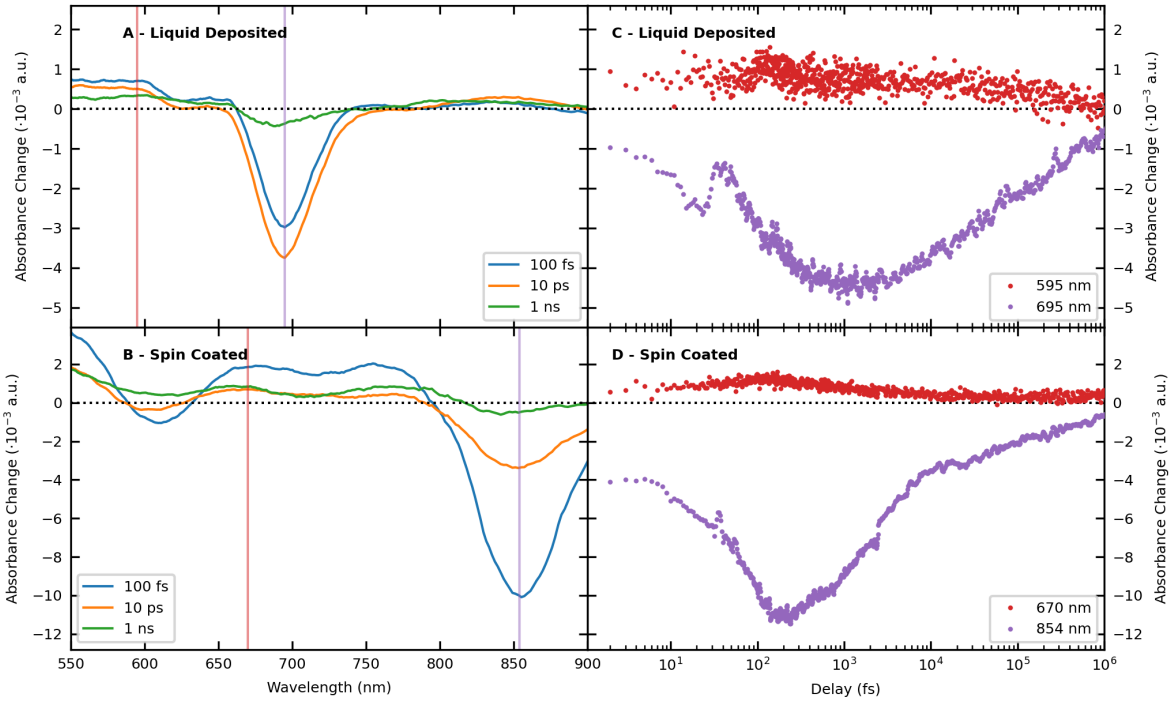

Figure 4.6: Transient absorption spectra recorded at different delay settings for the liquid deposited (A) and spin coated (B) samples, and their temporal evolution (C) and (D) respectively.

tion. Here, the raising of the signal can be clearly distinguished, where some features during this increase can be observed. A more complicated shape for the decay of the amorphous sample can be identified. It is evident that simplistic analysis methods, as it was done for the MIR dataset are bound to fail due to the complexity of the dynamics taking place. A multi-exponential fit was used to give some first insights in the processes taking place.

It was possible to accurately fit the transient absorption across all wavelengths with the same four time constants and by allowing only the amplitude factor to change for each wavelength. This offered the first major insight that the time constants are shared between ESA and GSB, greatly reducing the complexity of the analysis, since only two effects (ESA and GSB) need to be considered, and which can be represented by the values at their maximum manifestation (as shown in Figures 4.6C&D for the accordingly colored lines in Figures 4.6A&B). All the parameters deduced from the multi-exponential fit will not be presented here, since they hold little to no further physical value.

4.5 Modeling the Interband Dynamics of MgPc Semiconductors

It should now be evident that any interpretation of the visible-probe transient absorption data set has to be based on a valid model that is specific to the problem and covers all the effects present. Such model can be constructed from the discussion in the previous chapter, although there are some topics worth considering first.

4.5.1 Building a Model

To begin with, it is necessary to reduce the representation of the sample from a semiconductor with a band structure to as few molecules as possible, since this will greatly reduce the number of states needed to describe the system. This simplification is rather easy, if one considers that the transitions in question (400 nm pumping and $550-800$ nm probing) are in the order of a few electronvolts (3 eV approximately is the pumping photon energy). The expected band structure of the MgPc was estimated at about 0.25 eV, and in the MIR transient absorption study there was no evidence of any specific dynamics taking place within that band. Therefore the band structure can be safely reduced to individual states (otherwise consider isolated molecules). Vibrational transitions can easily be neglected in the visible spectral range as well.

From the steady state spectra of MgPc samples it can be seen that there are two bands, which will be reduced to transitions from individual states, bringing the bare minimum number of states needed to describe this spectrum to three, namely a ground state and two excited states. The ground to first excited state transition depicts the Q-band and the ground to second excited state depicts the B-Band. Although the system is not expected to ever transition past the second excited state, there is the need to depict some higher energy levels for the system to be free to absorb even when it is on the highest excited state. This is where (at least part of) the ESA originates from. In reality, the non localized ESA from the visible-probe transient absorption data indicate that the higher excited states form a broad band, or even a continuum of states.This would also have to be reduced to the minimum number of states. It can be considered that within the observed spectral range, transitions from both the first and the second excited states to higher excited states can take place. Since the higher excited states are not in a discrete energy, but rather spread all over the range, signals originating from transitions from the first and the second excited states are also spread in the spectrum and overlapping with each other. The easiest and simplest way to depict this is to define two higher excited states, located above the second excited state, in such a way that the transitions from the first- to third- and second- to fourth- excited states are in resonance with photons of wavelength equal to each other and equal to the wavelength where the ESA is evaluated at. This leaves us with a five-level system which should in principle be capable of describing the fast dynamics taking place in the samples.

The last considerations have to do with the dissipation dynamics. It can be understood that part of the dynamics is going to be a decay from the second excited state to the first excited state and even possibly to ground (which will also be neglected as out of two mechanisms, only the fastest will take place and the decay from the second- to first- excited state seems to be crucial, in the sence that it does take place). The dissipation seems to last for up to nanoseconds, meaning that some intersystem crossing (ISC) would have taken place, putting population to a triplet state, where it can stay for that long. For this model no triplet will be included; instead the population at the first excited state will be allowed to stay there indefinitely. In essence this can be considered as if the ISC is instant and the energy level landscape does not change significantly between singlet and triplet states. The system remains a five-level system which now has to interact with a reservoir to allow for spontaneous emission and decay from the second to the first excited state. All other decay channels will be irrelevant or not allowed.

From literature, as well as the MIR-probe transient absorption experiments, it is known that the dominating dissipation mechanism is of excitonic nature. Although the specifics of the inclusion of such effects into a model were not discussed in detail in the previous chapter, it can easily be understood how to include excitonic effects by first considering the nature of excitons. An exciton is the quasi-particle description of the mechanism where two coupled atoms/molecules exchange their quantum state. If one was excited and the other was not, after some time the first would not be excited and the second would. In a chain of coupled atoms/molecules, the excitation would seem to propagate, much like a particle. This quasiparticle is the exciton. However, keeping the focus on the individual molecules, the exciton is just the mechanism where molecules are allowed to exchange states. This mechanism between two molecules is described by a Hamiltonian much like Equation 3.76, where all terms and operators relating to a quantized field are replaced with the equivalent terms and operators for just another molecule. At this point the system should include at least two coupled molecules both of which get perturbed by the excitation pulse.

Such a system, though, will still not behave as expected since there is no exciton dissipation mechanism included, only excitonic interactions in a closed system. In order to include the dissipation a realistic view of the system has to be adopted, at least for the crystalline's case, as a one dimensional chain of coupled molecules. For ease, polar coordinates will be considered, where the pulses maximum hits at the origin of the axis. Since the pulse has a spatial profile, not all molecules will experience the same field strengths, and the molecules at great distances will experience no excitation whatsoever. This creates a system where energy is passed through the chain from the central molecule to the furthest end of the chain and eventually gets dissipated. Thus, the dissipation can again be considered as an interaction with a Markovian reservoir. It should be highlighted that the molecule chain will be terminated at two molecules (so that

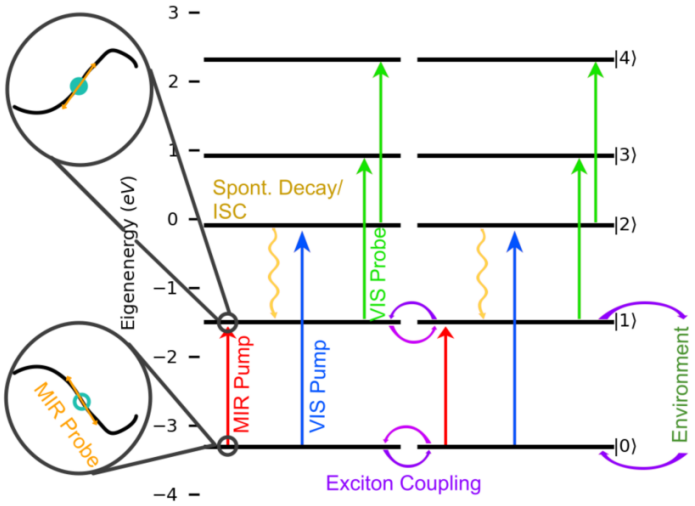

Figure 4.7: Modeled system scheme for the liquid deposited sample. The excitation and probe radiation is also overlaid for both transient absorption experiments. The blue and red arrows represent the perturbation caused by the exciting pulse, the green and orange arrows represent the probing pulses. The yellow arrows represent the interaction with the first reservoir (spontaneous emission) while the purple arrow shows the interaction between the molecules and the second reservoir (molecule chain).

exciton interactions can be included) and, out of the two, only the molecule in the second position is in contact with the reservoir and allowed to dissipate through it. In sum, the final simulation system looks like Figure 4.7. The pump and probe radiation from the MIR-probe and visible-probe experiments are also overlaid in Figure 4.7 for clarity, although the model was not meant to describe the intraband dynamics observed in the MIR-probe experiment.

4.5.2 Simulating the System

Now that the model is established, we can try to implement it. For the integration of the Lindblad equation a ready made library was used [60, 61]. It turns out that by optimizing the pulse parameters, the decay rates and the exciton coupling parameter, a rather accurate simulation of the crystalline sample can be achieved with minimal effort. On the contrary, the model would not describe the results of the amorphous sample irrespective of the parameters and the modifications made on the system. The sample response can be interpreted as raising too fast or not fast enough (depending on the simulation parameters).

Another mismatch is the shoulder seen in the data of Figure 4.6D around 10 ps, which cannot be simulated since it is indicative of a mechanism ending there, while another mechanism

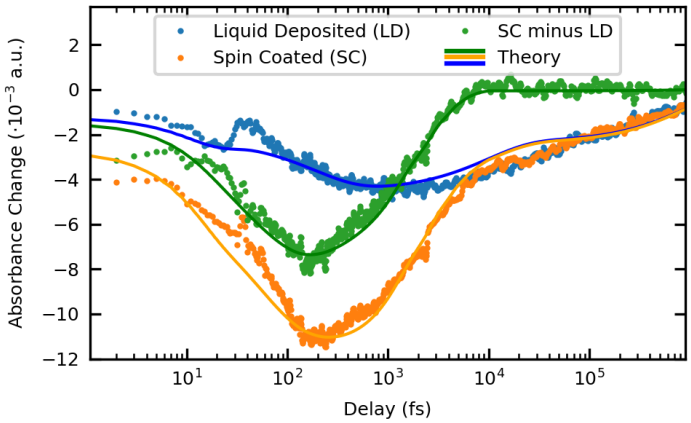

Figure 4.8: Simulation results for the crystalline (blue line) and the second contribution of the amorphous sample (green line). The response of the amorphous sample (orange line) is just the addition of the other two lines.

continues to take place. The model just described is incapable of doing that, since it follows the principle that if two mechanisms are active, the fastest will dominate and deplete all population, while the second one will never take place. This principle does not hold for the amorphous sample.

Last indication of what is going on is that if one overlays the data of the crystalline and amorphous samples and apply appropriate scaling (to account for the different sample thickness), the signals for delays greater than 10 *ps* completely overlap, while for all delays smaller than that, the signal of the crystalline is bellow that of the amorphous. This is a clear indication that the amorphous can be interpreted as a complex system consisting of two subsystems. One identical to the crystalline and one with different properties. Furthermore, given the response of the crystalline sample, the secondary response of the amorphous sample can be isolated by subtracting the two.

By doing so, a clear excitation signal can be obtained that can easily be simulated by the model described above with only a few parameter changes representing parameters of the material alone, such as decay rates and exciton coupling strength.

4.5.3 Result Interpretation

Now that a valid simulation is established for both samples, the focus can be shifted on the simulation results and what their implications are. To this end, consulting the overlay with the data (Figure 4.8) along with the calculations as depicted in Figure 4.9, where the electric field of the exciting pulse, the calculated population of each state, the resulting transient absorption

spectrogram as well as static spectra of the samples and the simulated system are shown.

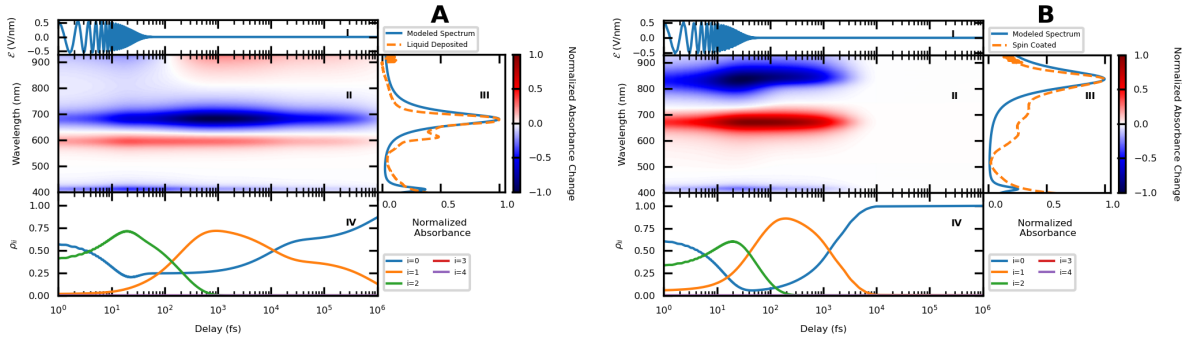

Figure 4.9: Simulation parameters and results for the crystalline (A) and the second contribution of the amorphous sample (B). The exciting pulses (I) (which are identical), the simulated transient absorption spectra (II), steady state absorption spectra (III) and the diagonal elements of the calculated density matrices (IV) are shown.

The first mismatch that has to be discussed is the oscillation-like behaviour that seems to happen for times greater than 1 ps. This is caused by the oversimplification of the excitonic mechanism. The dissipation rate that was set on the interaction with the second reservoir immediately relates to the position of the knee that happens when the data change from increasing to decreasing in amplitude. This parameter reflects the real time constant. On the other hand, the devised system with just two molecules is unable to hold a realistic amount of energy and starts losing energy too fast. This energy loss can only be limited by setting a non realistic exciton coupling intensity, much smaller than what it should be. The exciton coupling parameter, therefore, only holds for comparative studies between equivalent systems. It does not relate to its real value. This leads the second molecule to lose energy faster than what it can replenish from the first molecule, making the populations of the two molecules unequal. The simulations take into account the average population of the two molecules that seems to have that oscillation-like behaviour. Simulating with more molecules quickly eliminates this artefact, although it is computationally impractical to include more molecules in a five-level picture and when the calculations have to span for up to nanosecond time scales.

The second feature worth mentioning is the one around 20 fs, which is especially pronounced on the crystalline sample. This is caused by the intense pumping, while the transition is slightly off resonant. It can also be that partly a Rabi oscillation starts to take place just before the pulse ends giving this characteristic shape. This characteristic was used to turn the simulating software into a fitting algorithm through which optimum parameters for the excitation pulse were determined. As in can be seen in both systems (Figure 4.9 subplots IV), the exciting pulse

is putting population on the second excited state. Then, as energy dissipates, the population moves into the first excited state, where it remains until the exciton dissipation mechanisms return it to ground.

Taking a closer look at the parameters given for each simulation, for the crystalline sample a time constant for the second to first excited state of 200 fs and an exciton dissipation time constant of 10 ps. For the second contribution of the amorphous sample, a time constant for the second to first excited state of 50 fs was used while the exciton annihilation time constant was set to 1 ps. The exciton coupling strength had to be modified by an order of magnitude as well. For both simulations, the pulse duration was set to 40 fs, with a central photon energy of 3 eV and amplitude of 0.5 V/nm.

In conclusion, it can be distinguished by means of transient absorption techniques in the visible and MIR range, that the spin coated (amorphous) sample consists of two independent subsystems, one that behaves similar to the liquid deposited (crystalline) sample, which contains neatly organised stacks of MgPc molecules, and one that seems to vary significantly in its properties. The exciton coupling in the second subsystem seems to be much higher, which is consistent with the presence of the exciton coupling induced X-phase absorption peak. The decay rate is also higher, indicating an exciton dissipation dimensionality difference in the two subsystems, which is consistent with the findings of the investigation under MIR-probe transient absorption, as well as the explanation of the X-phase absorption peak [53]. The difference is thus found not to be the crystallinity of the two samples, but rather the presence of the different molecular arrangements, as the crystalline sample lacks the X-phase configuration, while the visible-probe transient absorption response of the amorphous sample reveals two internal structures, namely stacked molecules (although with no preferred orientation of the stacks, thus the completely amorphous nature) and X-phase behaviour (Further contributing to the amorphous nature).

Chapter 5

Attosecond Streaking Spectroscopy as Transient Photoemission Technique

Having established a solid understanding of transient absorption techniques and the dynamics resulting from light-matter interactions, it is only reasonable to wonder whether there is a way to utilize the already established attosecond spectroscopy techniques and the beamlines available to record the dynamics of a system with attosecond precision. This chapter will revolve around the basic ideas behind conducting such an experiment and what one should expect, as well as suggestions on how to analyze the results.

5.1 Attosecond Streaking Spectroscopy

The attosecond streaking spectroscopy [12,62,63] is a technique where an intense few-cycle phase stabilized NIR laser pulse is used to cause HHG in a small cell filled with some gas (typically Neon) [10,11,13]. The resulting harmonics have photon energies odd multiples of the generating fundamental [64--72]. They typically span up to 150 eV regions, which is the XUV spectral region. The harmonics co-propagate with the NIR pulse, albeit with much smaller divergence due to the difference in wavelengths. Out of the harmonic attosecond pulse train an attosecond pulse must be isolated. There are a few ways to achieve this, such as spectral filtering [12--14], polarization [15,16], double optical [17] or ionization [18,19] gating. The two pulses are spatially isolated so that a delay can be applied by some form motorized delay line (typically piezo-electric stage). The two pulses are then focused on a sample.

The attosecond XUV pulse causes photoelectric effect [73, 74], liberating electrons from the

sample. The liberated electron wavepacket can be considered almost a replica of the attosecond pulse, in the sense that it will have similar time duration and intensity profile when it is generated. The femtosecond NIR pulse will act on the liberated electrons, as an electric field does on a free charged particle, modifying their momentum [10, 12, 62, 63]. A complete pulse would not affect the final momentum of an electron since the sum of the force acted upon the it will be zero, but by varying the delay between the pulses the time at which the electron is liberated changes and thus from which point on the pulse would start acting on the electron. The summation of the electric field along the time axis to calculate the force results in a shape for the end momenta proportional to the vector potential of the pulse. In fact, this is the basic principle of attosecond streaking [75]. The liberated electrons propagate in vacuum and are collected by an electron energy analyzer, typically a time of flight (TOF) spectrometer. By recording spectra for different delay values one can probe the complete femtosecond NIR pulse and record its vector potential as a shift in the observed photoelectron lines positions.

5.1.1 Description of Attosecond Streaking Spectrogram

From a quantum mechanical standpoint, this problem differs slightly from what has already been described in the previous chapter. Considering an atom within the streaking fields, the Hamiltonian for an electron of the atom will then read:

$$H = H_{kinetic} + H_{atom} + \mathcal{V}(t) = H_0 + \mathcal{V}(t) \tag{5.1}$$

where H_{atom} contains all potential contributions caused by the atom and its other electrons. Assuming that the external field is much stronger than any interactions by the atom, the perturbation methods described in previous chapters can be used to treat this problem too. Starting from the most general case, Equation 3.34 can be rearranged to highlight what needs to be considered.

$$\frac{dC_k(t)}{dt} = -\frac{i}{\hbar}\sum_n \langle \Psi_k | \, \mathcal{V}(t) \, | \Psi_n \rangle \tag{5.2}$$

where k denotes the final wavenumber ($p = \hbar k$) of the electron and n runs over all states. Some approximations can be applied to simplify it further. Beginning with the single-electron approximation [10], assuming that the system only has one electron for the $n = 0$ state, the following can be derived:

$$\frac{dC_k(t)}{dt} = -\frac{i}{\hbar} \langle \Psi_k | \, \mathcal{V}(t) \, | \Psi_0 \rangle \tag{5.3}$$

As discussed above, the perturbation is given by $\mathcal{V}(t) = -e\mathbf{r} \cdot \mathbf{E}_X(t) - e\mathbf{r} \cdot \mathbf{E}_L(t)$, where $E_X(t)$ is the electric field of the XUV pulse and $E_L(t)$ is the electric field of the NIR laser pulse. Each term should give rise to a photoionization probability as described in Section 3.2.3. Considering transitions to vacuum, and specifically to a high order multiple of the laser frequency, the denominator in the probability equation will be considerably large, while the term $|\mathcal{V}_0(v)|^2$ is, comparatively speaking, vanishingly small. After all the pulse already lost a lot of energy during the HHG process, which is not efficient whatsoever, therefore causing HHG again is unreasonable. Thus the term containing the laser's electric field will be neglected for transitions so high into vacuum, resulting in:

$$\frac{dC_k(t)}{dt} = i\frac{e}{\hbar} \langle \Psi_k | \, \mathbf{r} \cdot \mathbf{E}_X(t) \, | \Psi_0 \rangle \tag{5.4}$$

Now the initial and final states should be determined. For the initial state, without the loss of generality, it can be written directly, that:

$$|\Psi_0\rangle = e^{-i\omega_0 t} \, |g\rangle = e^{i\frac{I_p t}{\hbar}} \, |g\rangle \tag{5.5}$$

where I_p is the ionization potential and $|g\rangle$ the spatial part of the ground state. No amplitude factor was included since it was assumed that the electron is certainly at the ground state ($c_0 = 1$). It will also be assumed that there will be no significant population percentage leaking to vacuum, so that $c_0(t) = 1$ for all times.

The next task is to consider the final states of the electron, which are easily defined within the strong field approximation (SFA) [10, 76]. According to this approximation, for a liberated electron, the effect of the atomic Hamiltonian is negligible with respect to the interaction with the electric field. It is also beneficial to work out this interaction in the velocity gauge:

$$H = H_{kinetic} + \mathcal{V}(t) = \frac{1}{2m_e} \left[\mathbf{p} + \mathbf{A}(t)\right]^2 \tag{5.6}$$

with $\mathbf{p}$ being the momentum of the electron and $\mathbf{A}(t)$ the vector potential of the external field. This is also know as the Volkov Hamiltonian in velocity gauge. A plane wave with a time dependent phase can be used as ansatz:

$$|\psi_k\rangle(t) = e^{-i\phi_k(t)}|k\rangle \tag{5.7}$$

By replacing back to the Hamiltonian an expression for the time dependent phase can be obtained:

$$\phi_k(t) = \frac{1}{2\hbar m_e}\int^t \left[\mathbf{p} + \mathbf{A}(t')\right]^2 dt' \tag{5.8}$$

In this specific problem, the amplitude of the XUV radiation is going to be orders of magnitude lower than that of the laser pulse. It can thus be written that $A(t) = A_X(t) + A_L(t) \approx A_L(t)$. The final state would then read:

$$|\Psi_k\rangle(t) = e^{-i\frac{1}{2\hbar m_e}\int^t [\mathbf{p}+\mathbf{A}_L(t')]^2 dt'}|k\rangle \tag{5.9}$$

The above can now be replaced in Equation 5.4:

$$\frac{dC_k(t)}{dt} = i\frac{e}{\hbar}\langle k|\,\mathbf{r}\cdot\hat{\mathbf{e}}_X\,|g\rangle\, E_X(t) e^{i\frac{I_p t}{\hbar}} e^{i\frac{1}{2\hbar m_e}\int^t [\mathbf{p}+\mathbf{A}_L(t')]^2 dt'} \tag{5.10}$$

The time dependent probability amplitude for an electron with momentum k can be found by integrating:

$$C_k(t) = \frac{e}{i\hbar}\langle k|\,\mathbf{r}\cdot\hat{\mathbf{e}}_X\,|g\rangle \int_{-\infty}^t E_X(t') e^{i\left\{\frac{I_p t'}{\hbar} + \frac{1}{2\hbar m_e}\int^{t'} [\mathbf{p}+\mathbf{A}_L(t'')]^2 dt''\right\}} dt' \tag{5.11}$$

The quantity $D(r,k) = \frac{e}{\hbar}\langle k|\,\mathbf{r}\cdot\hat{\mathbf{e}}_X\,|g\rangle$ is the photoionization cross section. The actual observable is the recorded spectrogram, or otherwise the probability of an electron being at $E_k = \frac{\hbar^2 k^2}{2m_e}$ for a set delay (t) is [62]. This is nothing more than the absolute square of the probability amplitude:

$$S(k,t) = |C_k(t)|^2 = \left|\frac{1}{i}D(r,k)\int_{-\infty}^t E_X(t') e^{i\left\{\frac{I_p t'}{\hbar} + \frac{1}{2\hbar m_e}\int^{t'} [\mathbf{p}+\mathbf{A}_L(t'')]^2 dt''\right\}} dt'\right|^2 \tag{5.12}$$

Although the above equation looks rather complicated at first, the meaning of all terms is quite simple to decode. It should be borne in mind that it describes a photoelectron spectrum where

the intensity relates to the photoionization cross section relateing the symmetry of the spatial parts of the initial and final states and also taking into account the polarization direction of the driving field. The intensity also relates to the intensity of the XUV pulse. The phase terms inside the integral will just calculate the contribution of the laser field to the electron's energy balance and define the frequency of the wave packet from it, which is nothing more than the perceived position of the photoelectron peak in the spectrum.

5.1.2 Aftermath of the Attosecond Streaking Formula

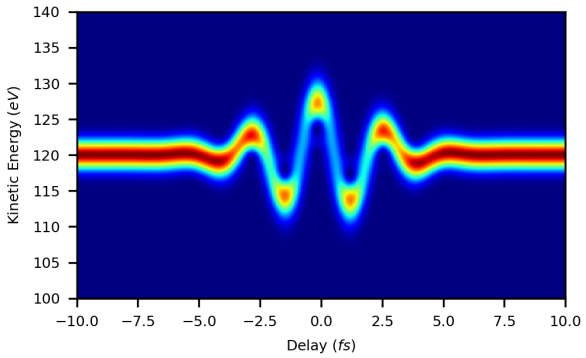

Figure 5.1: Attosecond streaking spectrogram example. An infrared pulse with 5 fs duration (FWHM), photon energy of 1.5 eV, and a carrier envelope phase (CEP) of -70 degrees has been selected. For the XUV pulse, a photon energy of 120 eV, and a pulse duration of 0.8 fs has been given. The binding energy has been set to 0 in this example.

An example of a spectrogram calculated by using the equation above is shown in Figure 5.1. The parameters used for such a calculation are given in the caption. Here it can be seen that for long delays, when the pulses do not overlap, there is just a photoelectron line appearing at the specific kinetic energy which is given by the energy balance $E_k = \hbar\omega_{XUV} - I_p$. Once the pulses start to overlap, the kinnetic energy of the photoelectrons is modified. This modification is defined by the term $[\mathbf{p} + \mathbf{A}_L]^2 = \mathbf{p}^2 + \mathbf{A}_L^2 + 2\mathbf{p} \cdot \mathbf{A}_L$. In most cases, the last term can be neglected and the dominating modification is the vector potential of the laser field, which is seen in Figure 5.1.

One interesting aspect in the attosecond streaking spectroscopy is the fact that the spectrogram holds all the information about the amplitudes and phases of both generating pulses, which means that several techniques can be used to retrieve the pulses parameters. Frequency Resolved Optical Gating (FROG) type methods can be used [77], with their most refined forms being the Least Squares Generalized Projection Algorithm (LSGPA) [78] and the ptychographic methods [79, 80]. If pulses with known shapes (such as gaussian envelopes, low chirp etc.) are

used, least squares minimization algorithms can be used [81--84] yielding more than satisfying precision. As such the technique is often used as a robust pulse characterization method. More details about the pulse characterization methods can be found in Appendix B.

Another major application of the attosecond streaking spectroscopy arises from the fact that there can often be more than one states within a material that give rise to photoelectron peaks. When these peaks are separated enough for the two photoelectron lines to be distinguished, the aforementioned techniques can be used to characterize the pulses from each individual line. There is a certain amount of delay between the individual lines [81], which can be caused by many different mechanisms that relate to the phase that the photoelectron acquired before and during its exposure to the electric field of the laser. The area of study of the photoionization delays is called attosecond chronoscopy [85] and is a major field in attosecond science [86].

5.2 Prediction of Dynamics Signature

As discussed in the previous section, the attosecond streaking technique is a really powerful tool for pulse characterization as well as for piercing into the nature of the photoionization process itself. This work largely aims to investigate if the same technique can be used for, or extended towards the recording of electron dynamics within the parent atom in a pump-probe-like picture. The idea is to push the resolution down to the attosecond timescale that the attosecond streaking spectroscopy can offer.

5.2.1 Developing a calculation model

We should start by trying to predict how a photo-excitation would manifest itself in the context of attosecond streaking. To this end, a scheme where both the photo-excitation theory and the streaking spectroscopy theory would be particularly helpful. In the discussion about Equation 5.5, an argument was raised concerning the existence of a $c_0(t)$ factor that was excluded due to the assumptions made (low photocurrent and only one active electron in the ground state). Including this factor is the key to combining both models, as it was meant to adjust the transition probability based on the probability of an electron being in that state at time t. The simplest way, therefore, is to use the photo-excitation dynamics model to calculate the population distribution in our model system. Then, a photoelectron line would have to be generated for every state of our modelled system. This factor will be included by multiplying each generated photoelecton line with the corresponding diagonal element of the density matrix for the set delay value, as it comes down to the same result, under the assumption that the population does not change significantly in the timescale of the attosecond pulse. For the time

being, all cross sections will be set to unity, so that the intensity of all photoelectron lines will depend only on the population of the states.

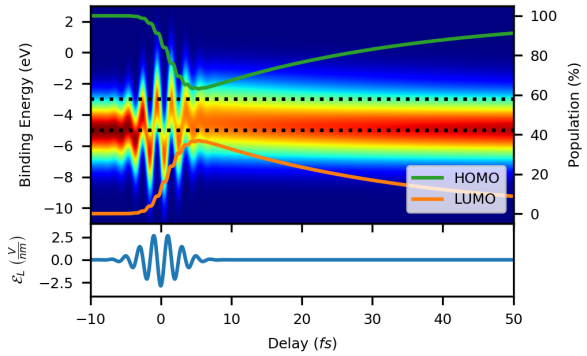

Figure 5.2: Implementation of the above described model. As a system a two level system is selected for simplicity. The energy levels are depicted as black dashed lines. For the XUV pulse a photon energy of 120 eV has been given and a pulse duration of 0.8 fs. The energy axis takes into account the photon energy to reveal the binding energy.

Such a calculation is presented in Figure 5.2. A two-level system is selected with binding energies of -5 eV and -2 eV. The off-diagonal dipole matrix elements are simply set to 1. A fast spontaneous decay is included to show the effects of decay in the same scale as the streaking trace. The XUV pulse was set to central photon energy of 120 eV and a duration of 0.8 fs. The effects of the photo-excitation in the photoelectron spectrum can now clearly be observed in a streaking spectrogram. The binding energies of the system's eigenstates have been marked on the spectrogram in Figure 5.2 with black dashed lines. Here it can be noted that for negative delays, before the NIR pulse starts, the photoelectron line is centered around the ground state's binding energy. During the streaking, when the two pulses overlap, the situation becomes more complex, although in general it looks like the center of the line (ignoring the streaking oscillations) is pulled towards higher binding energies. Right after the streaking has ended we can clearly see that the photoelectron line has been broadened towards the higher binding energies, almost half-way to the binding energy of the excited state. This is because with the selected parameters we are pumping close to 40% of the population on the excited state. As the population decays, there is a gradual narrowing of the photoelectron line until the system relaxes completely, where the photoelectron returns to its original shape.

5.2.2 Considerations on the Signal Strength

Although no further processing is needed to extract conclusions from the results in Figure 5.2 taken into consideration that this is a calculation aiming at highlighting the effects. For instance,

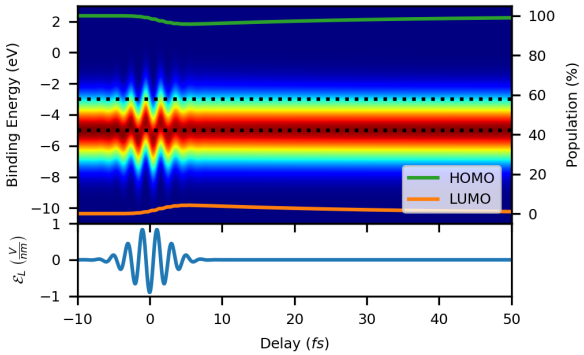

Figure 5.3: Recalculation of the aforementioned model for weaker electric field.

the strength of the electric field used in this simulation is five times that of the simulations for the MgPc transient absorption measurements. Although this is possible to achieve, it is doubtful whether a material would survive long enough under such radiation to obtain a satisfactory measurement. Therefore unrealistic expectations should be avoided.

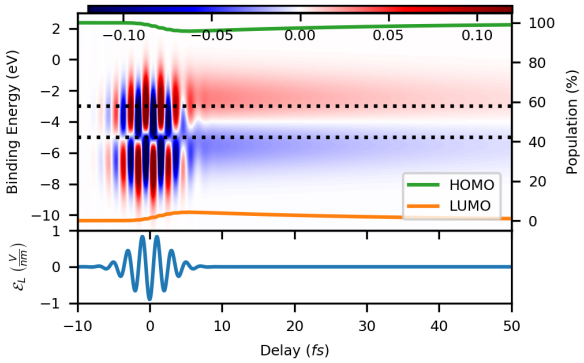

Figure 5.4: Recalculation of the above mentioned model for weaker electric field. A reference spectrum of the system on ground state has been subtracted from all individual spectra.

In Figure 5.3 the expected signal is calculated again but this time a more reasonable laser intensity has been given. In this case, only a few percents of the total population make it to the excited state, thus the change in the photoelectron spectrum is equivalently low. It is really hard to recognize any of the effects noted before by naked eye. To emphasize the differences to the initial spectrum, a reference spectrum recorded for negative delays (XUV pulse hits before the laser pulse) will be subtracted. The results are shown in Figure 5.4, where,sufficiently low noise has been assumed, the signal (after the streaking at least) can easily be perceived and quantified. In the case shown here the signal is in the order of 3% after streaking.

5.2.3 Analysis Approaches

Although the streaking is taking place it is not trivial to evaluate what is happening, once the streaking is over the differential signal around each state's binding energy can be summed and used directly with a simple fitting model as was done in the analysis of the MIR transient absorption technique. It should be noted that the lines here do not relate to the population difference, as was the case for the transient absorption signals; Instead they relate directly to the population of a state. This top-down analysis approach can prove very useful if a good enough fitting model has been established. The experiment is designed to collect data for a range of few hundreds of femtoseconds. During this time window, there is limited activity, which means that any dynamics would be purely electronic, for which a few-exponential fit should be decent.

Lastly, the calculation method developed here can be used with a more physical model for a system similar to the one developed for the visible transient absorption analysis to match the differential signal recorded from the experiment. The bottom-up analysis approach is more demanding since a really robust model of the system is necessary, but it could also reveal information about the dynamics even in the streaking region, where the pulses overlap.

5.3 Development of a Top-Down Analysis Method

The attosecond streaking spectroscopy offers a chance of recording the dynamics of a system with an unmatched temporal resolution. In this case, the long-lasting (from the attosecond prespective) dissipation dynamics are of no major interest, since a visible transient absorption technique could in most cases reveal the same dynamics with ease and without the need for such a complicated setup that the attosecond streaking spectroscopy does.

What the attosecond streaking technique can offer is the highest possible temporal resolution together with a completely controlled excitation and probe pulse, the ability to fully characterize the pulses used in the specific measurement, and a highly controlled environment, due to the experiments taking place in vacuum. Combined with a good model description of the system, this would give access to the exact quantum states of the system during the entire excitation process. As has been established thus far, accessing the exact quantum states of the system is only possible in the bottom-up analysis approach. Although this is already important, the possibility of piercing into the pulse overlap region with a top-down analysis method should be investigated, since such approaches are much faster to implement and are useful in cases where the exact nature of the sample is not understood.

In the prediction of the signal, what made the signal interpretation impossible in the pulse overlap region was the effect of the infrared pulse onto the photoelectron wavepackets, otherwise,

the streaking itself. This effect needs to be further investigated in order to deduce if there is a way to counteract it in a simple enough way. In principle it can be considered as three main effects. An intensity modification due to possible photoionization cross section dependency on the photoelectrons' final momentum, the shift of the photoelectron peak due to the laser pulse vector potential and, narrowing and broadening of the photoelectron peak due to streaking.

5.3.1 Counteracting the Streaking Effects

Any intensity modulations can easily be counteracted, at least partially, by normalizing the photoelectron spectra. Assuming that the photoionization cross section for both the ground and the excited states is the same, normalization on the area under the photoelectron peak can be performed, effectively normalizing on the total number of photoelectrons.

The second effect, namely the shift of the photoelectron peak by the vector potential of the laser pulse is by far the most pronounced and is the one that the attosecond streaking spectroscopy method is known for. This can be negated by performing some form of center of energy (COE) fit to the spectrogram in order to retrieve the exact position of the photoelectron peak for every delay value. The peak can then be shifted according to the positions obtained from the last step. There are several ways to perform this operation, for instance by performing a center of mass fit, or by trying to fit Gaussians on the individual spectra and obtaining the center point of the fitted Gaussians. This could in principle handle most of the problem. In reality, though, the streaking amplitude is photon energy dependent and this process introduces more errors to the spectrogram. Furthermore, when the signal is significantly smaller than the primary photoelectron peak, higher order effects need to be considered that could only be accounted for by numerically solving Equation 5.12. This only allows for a bottom-up analysis options.

5.3.2 Temporal Resolution Over Spectral Resolution

The goal of a top-down analysis is the easy quantification of a phenomenon or a process with as little assumptions for the exact nature of the subject system as possible. To this end, it can be shown that, by abandoning the spectral resolution for the region where the pulses overlap, a clear look at the photo-excitation process can be obtained. The positions of the photo-excited electrons can be spectrally resolved as soon as the two pulses stop overlapping, as it can be seen in Figure 5.4.

To show how to retrieve such signals, the discussion about the ground state of the system as shown in Equation 5.5 needs to be re-evaluated. There, a single active electron located on the ground state was assumed. The same assumption will be made here, but the electron is allowed

to occupy an excited state, thus:

$$|\Psi_0\rangle = \sum_{j=0}^{1} c_j e^{-i\omega_j t} |j\rangle = \sum_{j=0}^{1} c_j e^{i\frac{I_p^j t}{\hbar}} |j\rangle \tag{5.13}$$

where c_j is the amplitude of the electron being at the $|j\rangle$ state, which has ionization potential of I_p^j. The predicted spectrogram would then read:

$$S(k,t) = \left| \frac{1}{i} \sum_{j=0}^{1} c_j D_j(r,k) \int_{-\infty}^{t} E_X(t') e^{i\left\{ \frac{I_p^j t'}{\hbar} + \frac{1}{2\hbar m_e} \int^{t'} [\mathbf{p}+\mathbf{A}_L(t'')]^2 dt'' \right\}} dt' \right|^2 \tag{5.14}$$

where c_j is treated as a time independent in the aftermath of the approximations of the single active electron, as well as the assumption that no significant population would be moved by and during the photo-excitation process, same as was done for the photo-ionization process. The equation can be rewritten by substituting $\rho_{jj} = c_j c_j^*$:

$$S(k,t) = \rho_{00} S_0(k,t) + \rho_{11} S_1(k,t) \tag{5.15}$$

where it was defined that:

$$\begin{aligned} S_0(k,t) &= \left| \frac{1}{i} D_0(r,k) \int_{-\infty}^{t} E_X(t') e^{i\left\{ \frac{I_p^0 t'}{\hbar} + \frac{1}{2\hbar m_e} \int^{t'} [\mathbf{p}+\mathbf{A}_L(t'')]^2 dt'' \right\}} dt' \right|^2 \\ S_1(k,t) &= \left| \frac{1}{i} D_1(r,k) \int_{-\infty}^{t} E_X(t') e^{i\left\{ \frac{I_p^1 t'}{\hbar} + \frac{1}{2\hbar m_e} \int^{t'} [\mathbf{p}+\mathbf{A}_L(t'')]^2 dt'' \right\}} dt' \right|^2 \end{aligned} \tag{5.16}$$

This is percicely the consideration that drove the simulation of the signal as a sum of photoionization peaks for every available state weighted by the population of each state. Equation 5.15 can be generalized to arbitrarily many states. As discussed in Subsection 5.1.2, Equation 5.12 can be used in a least squares minimization scheme to construct a retrieval algorithm for the pulse parameters [81--84]. The method is referred to as the restricted time-dependent Schrödinger's equation (TDSE) method (see Appendix B). The utilization of this technique will be demonstrated to uncover the dynamics hidden within the overlap region.

The advantage of this technique over all other retrieval methods is its restricted nature. The

method uses Equation 5.12 in combination with pre-defined pulse shapes (Gaussian envelopes) to generate a spectrogram as a function of a limited number of parameters. The parameters are then optimized to minimize the error with the given spectrogram. Since it follows Equation 5.12, it includes all effects caused from the streaking. The restricted nature of the technique does not allow it to arbitrarily modify the pulses or the intensity of the spectrogram to account for mismatches to the input spectrogram. It has further been shown that for composite signals, the technique seems to ignore small contributions of less than 10% to the signal completely [83], which is the exact case where our signal falls into.

If a good matching restricted TDSE retrieval can be performed on our spectrogram (S), we can ideally write for the recreated spectrogram from the retrieved parameters (R):

$$R(k,t) \approx S_1(k,t) \tag{5.17}$$

Now, the two spectrograms can be subtracted, while the temporal evolution of the density matrix should also be considered at this point.

$$S(k,t) - R(k,t) = \rho_{00}(t)S_0(k,t) + \rho_{11}(t)S_1(k,t) - S_0(k,t) \tag{5.18}$$

The total population remains the same, so $\rho_{00}(t) + \rho_{11}(t) = 1$. It then follows that:

$$S(k,t) - R(k,t) = [1 - \rho_{11}(t)]S_0(k,t) + \rho_{11}(t)S_1(k,t) - S_0(k,t)$$

$$S(k,t) - R(k,t) = -\rho_{11}(t)\left[S_0(k,t) - S_1(k,t)\right] \tag{5.19}$$

If the quantities involved should now be considered, assuming that the photoionization cross sections are not greatly affected by the kinetic energy shift induced by the streaking, then the only real time dependent amplitude term in this equation is the population of the excited state, which is energy independent. The time dependence in the $S_0(k,t)$ and $S_1(k,t)$ only relates to the phase effects of the streaking, which result in shifts and compressions of the photoelectron peak along the kinetic energy axis. Thus, if the spectrograms are subtracted and the result is summed over the kinetic energy axis, a quantity that whose only temporal dependence is the population of the excited state will be obtained.

This method is sensitive to amplitude changes due to experimental imperfections (such as laser stability) and possibly susceptible to noise, since the term $[S_0(k,t) - S_1(k,t)]$ can be rela-

tively small with respect to the amplitudes of both $S_0(k,t)$ and $S_1(k,t)$. Thus, good references accompanying each individual spectrum need to be recorded. The signals need to be recorded with significantly high signal to noise ratio in order to enable the implementation of this analysis method. If such measures are to be implemented in an experiment, the analysis method could prove itself useful, as it is easy to perform and general enough to not be case-specific.

5.3.3 Demonstration of the De-Streaking Retrieval Method

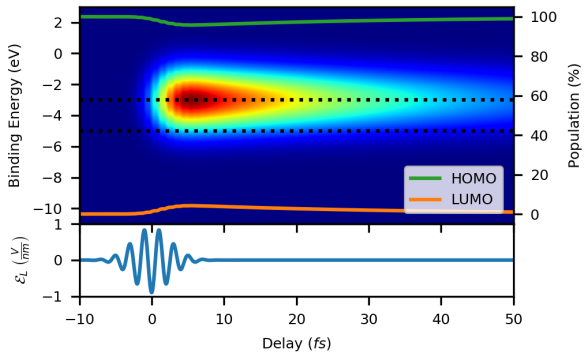

Figure 5.5: Recalculation of the photo-excitation signal alone, without any effects from attosecond streaking.

A demonstration of how such a method is supposed to work in principle will follow, beginning by performing the exact same simulation of a signal, as it was done in the previous section. We can demonstrate what the signal would resemble by reducing the streaking amplitude to zero and only generating a photoelectron line for the excited state. Such a line can be seen in Figure 5.5. It is clear that, other than the actual binding energy and bandwidth of the line (which can easily be deduced once the streaking is over by subtracting a reference spectrum), no information is present along the energy axis. The information that we are interested in is the population evolution of the excited state (ρ_{11}), which is imprinted in the intensity of the photoionization peak as described by Equation 5.15. It is evident that the intuition of sacrificing the spectral resolution to gain access to the photo-excitation process in a top-down scheme is valid.

A restricted TDSE retrieval of the spectrogram depicted in Figure 5.3 can be performed. Once the parameters of both pulses are retrieved, a reconstruction of the spectrogram, as well as a the difference between the original spectrogram and the recreation can be generated. Such results can be seen in Figure 5.6, which illustrates that the original and reconstructed spectrograms are very similar to one another. Still, the difference indicates a small degree of mismatch which increases as the photo-excitation signal starts forming. This is expected and is going to allow for this analysis to be performed.

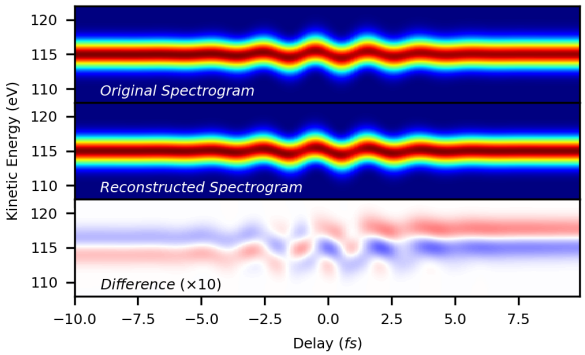

Figure 5.6: Results of a restricted TDSE retrieval.

To obtain a good reconstruction, the algorithm needs to see data that are as focused as possible to the streaking range. The reconstruction can then be extended to match the experimental window if need be. It is also essential that the photoelectron spectrum is matched as well as possible to minimize any sources of error. To achieve this, the common practice is to add a number of photoionization peaks and optimize their position and amplitude to get a decent description of the original spectrum. The fitting algorithm would then generate a streaking trace for every individual peak defined in the previous step. The streaking trace would then be the sum of all traces.

Applying the aforementioned method, a photo-excitation signal as the one shown in Figure 5.7 can be deduced. The signal obviously resembles the original signal and thus the population of the excited state to a satisfying degree. Any existent leftover defects from the streaking are reduced to a level where they do not obscure the picture of what is happening during the overlap of the pulses. The signal is much weaker than the original and can be inverted as shown by Equation 5.19, therefore, it may need to be inverted and its initial value to be set to zero. Then it can be scaled to match the signal observed after the streaking by subtracting a reference spectrum. By doing so one can obtain a fair estimation of the dynamics during photo-excitation as well as after the initial excitation can be obtained.

It is important to mention that effects such as differences in photoionization cross section or differences in the DOS between the ground and excited states are crucial for the signal to be adequately strong to be retrieved, as they will exaggerate the difference between the spectra that is demanded by Equation 5.19. If this is not the case the signal can easily be lost to noise or even completely gone in the case that the two states generate identical steady state photoionization spectra.

Whenever the signal is not retrievable with the method described above, an estimate can always be obtained by getting the absolute of the spectrogram differences. This will be a non

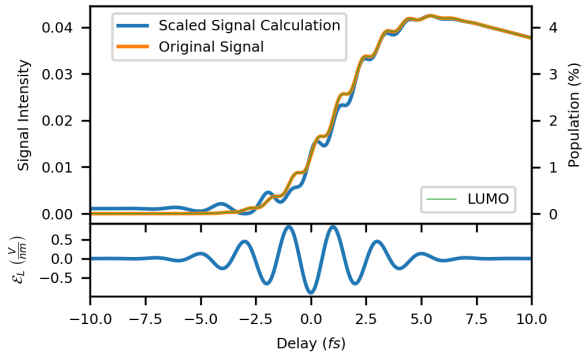

Figure 5.7: The photo-excitation signal as calculated by this analysis method (Top figure, blue line). The signal has been scaled to match the original signal, which is a cross section of the signal presented in Figure 5.5 at the central binding (orange line). The population of the excited state is also shown (green line).

vanishing value that loosely correlates to the population of the excited state. It is not guaranteed that the deduced value will always be between 0 and 1, nor that the streaking effects will be significantly reduced, but it should be tracing out the rough shape of the photo-excitation. Proper scaling will also be necessary, since it will depend on quantities that are not strictly defined or accounted for, such as the error of the restricted TDSE method and the photoionization cross section of each state.

Chapter 6

Measurements of Dynamics Using the Attosecond Streaking Spectroscopy

The ability to utilize the available attosecond beamlines, and more specifically attosecond streaking spectroscopy, to record photo-excitation dynamics, has been a major task in the E11 chair for many years. A lot of projects have been conducted in this direction but the results were typically underwhelming. It was a major aim of this work to examine whether such a measurement was possible. As shown in the previous chapter, there seems to be merit in the idea since, if one induces a few percents of population movement in a system, the technique could in principle resolve it and the signal could be analyzed.

In this chapter the experimental apparatus used for all the attempts that the author was part of will be described. The systems used will be presented and the individual ideas that motivated each project will be presented. Then typical results and findings will be showcsaed, explaining how the results motivated new investigations. Finally, suggestions for further research will be provided, given that the desired result is not obtainable with the instrumentation available.

6.1 Experimental Setup

All the experimental efforts that I was involved with utilized a specific beamline, namely the "AS3" chamber [83, 87, 88], which was initially located in the Max Plank Institute for Quantum Optics (MPQ). The setup was transferred, during the course of this work, to the E11 chair of the Physics department of Technical University of Munich (TUM). Only a part of the entire beamline was moved so the setup had different laser systems, different infrared pulse processing

and even different HHG setups. Apparently only a brief description of these systems will be provided in this section, as the specifics of the particular setup are described elsewhere [83, 88].

6.1.1 Laser System and High Harmonic Generation

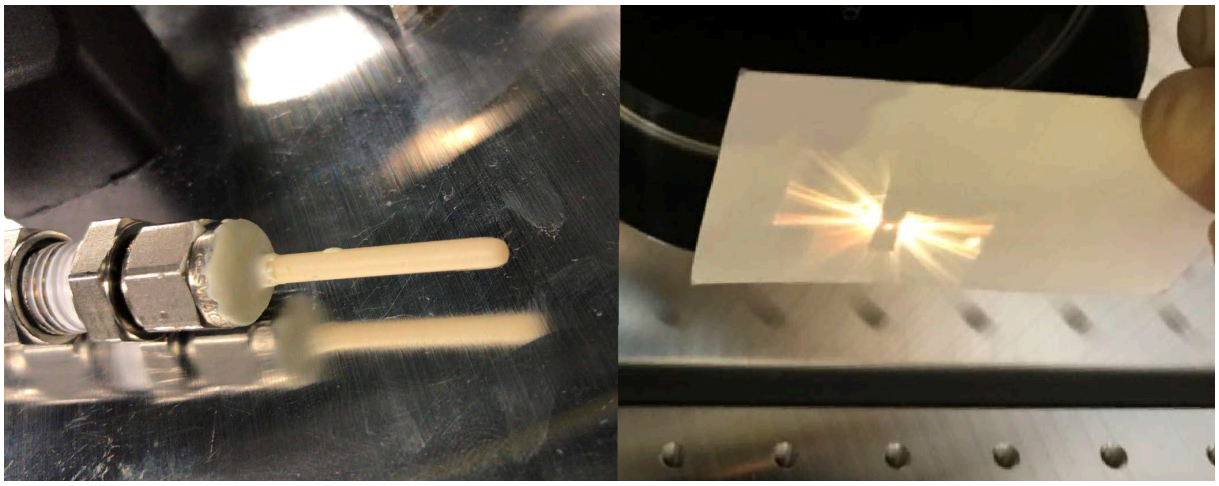

Figure 6.1: A ceramic cell used for HHG is presented. On the right image the laser light is shining on the target so that the hole of the cell is visible in the shadow of the target.

The latest setup consisted of a Ti:Sapphire mode-locked oscillator outputting pulses spectrally centered around 789 nm and a repetition rate of 75 MHz. A 0-to-f interferometer was located in front of the oscillator to measure the carrier envelope phase offset f_{CEO} and stabilize it using an acousto-optical frequency shifter (AOFS) by means of the feed-forward method [89]. The pulses from the oscillator where temporally stretched and amplified at a chirped pulse amplification (CPA) setup [90] which was a combination of a Ti:Sapphire based nine-pass preamplifier and a two-pass Ti:Sapphire based power amplifier unit. During the CPA process in the preamplifier the repetition rate is reduced down to 4 kHz using a Pockel's cell, while it also passes through an acousto-optic programable filter to adjust the dispersion up to fifth order and the spectrum of the pulses [91, 92]. The CPA unit increased the power of the beam from 100 mW to 12 W. The resulting high-power pulses were then compressed down to approximately 23 fs using a grating compressor. With the help of an active beam stabilization system the pulses where coupled into the entrance of a 3 m long hollow core fiber, with an inner diameter of 500 μm, filled with a nobble gas (typically He) from an inlet located at the center of the fiber. The ends of the fiber were actively pumped. Propagating the focused pulses through the He gas causes self phase modulation [2] due to its non-linear response, resulting in the spectral broadening of the pulse. Once the beam exits the fiber, it is kept in vacuum to avoid dispersion.

After re-collimating and by reflecting the beam several times by pairs of multilayer chirped mirrors, the spectrally broadened pulses were compressed down to few-cycle durations (typically $5-7\ fs$ according to the Fourier limit). The beam was then driven through a pair of wedges to finely tune the dispersion and thus the chirp of the laser pulses. A reflection from the wedges was collected into an f-to-$2f$ interferometer, probing the exact carrier envelope phase (f_{CEP}) of the pulses, and controlling a motorized pair of wedges located inside the oscillator cavity. By adjusting the optical path inside the oscillator a precise value for f_{CEP} could be set and stabilized. A motorized adjustable iris was placed after the compression wedges and was used to attenuate the outer parts of the beam, which is necessary for achieving phase-matching in the HHG process [84]. The beam was then focused by a spherical mirror (with typical focus length from 75 cm to 1.5 m depending on experimental requirements) into a ceramic target through which a small through-hole was drilled with a diameter of 150 μm. The target was constantly supplied with Ne with typical background pressure in the order of 10^{-3} $mbar$ in the HHG chamber. Inside the target the HHG process was taking place. After passing the target, the beam, now containing the laser pulses as well as the HHG radiation, was driven through a skimmer designed to contain most of the gas in the HHG chamber.

6.1.2 The AS3 Beamline

Figure 6.2: An overhead drawing of the AS3 beamline. The top halves of the chambers have been removed to offer the reader a view of the inside of the chambers

Once the beam passed the skimmer, the unchanged part of the beamline started. A long thin tube was differentially pumped to dispose of the residual gas that made it past the skimmer. At the end of this tube, a chamber containing several thin metal filters was located. The filters

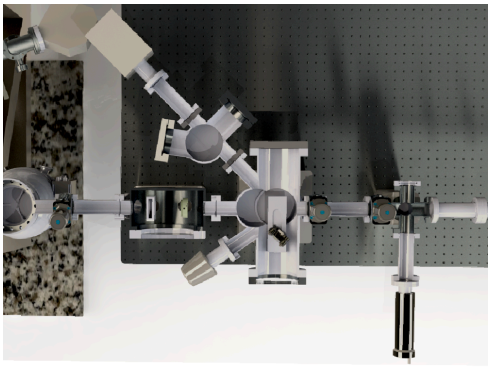

Figure 6.3: An overhead illustration of the filter and pellicle chambers. The motorized gold mirror is shown. When the mirror intercepts the beampath, the beam is deflected to the chamber next to the pellicle chamber, where the grating is. The XUV camera is shown as a white box.

were used when necessary to block the infrared and visible radiation of the laser, allowing only the high-harmonics to propagate through the metal filter and further into the beamline. Right after the filter chamber, a chamber containing a gold mirror mounted on a motorized stage was located. The stage was used to drive the mirror into the beam-path. The mirror would reflect the incoming beam into a spectrometer consisting of a grazing incidence grating optimized for radiation around 120 eV. An XUV camera was used to analyze the spectral components of the incoming radiation. To characterize the harmonic radiation, different combinations of thin metal filters were used to highlight characteristic absorption edges (typically the Al and Si edjes) allowing for the calibration of the spectrometer. Once the spectrometer was calibrated, a pair of Zr filters were used to record the XUV spectrum.

When the gold mirror was not intercepting the beam, the latter was allowed to propagate into the next chamber, which contained another motorized adjustable iris together with a thin metal filter mounted on a pellicle. The pellicle was adjusted to block the central part of the laser beam, blocking the infrared and optical radiation but allowing the XUV radiation to propagate through it. This separated the two pulses spatially, allowing for tunability of the delay between them at a later stage. The iris was used to attenuate the outer parts of the laser radiation, allowing for fine tuning of the peak intensity of the laser pulses at the sample.

After the pellicle chamber, the beam was propagated through the last differential pumping station and into the experimental chamber which was kept in ultra high vacuum conditions (background pressure in the order of low 10^{-10} mbar). The last optical component in this chamber was a double mirror mounted on several motorized stages, allowing for full adjustment of its pointing as well as its distance to the sample. The mirror was split into two parts, namely the inner and outer part, matching the geometry of the spatially separated beams. The outer

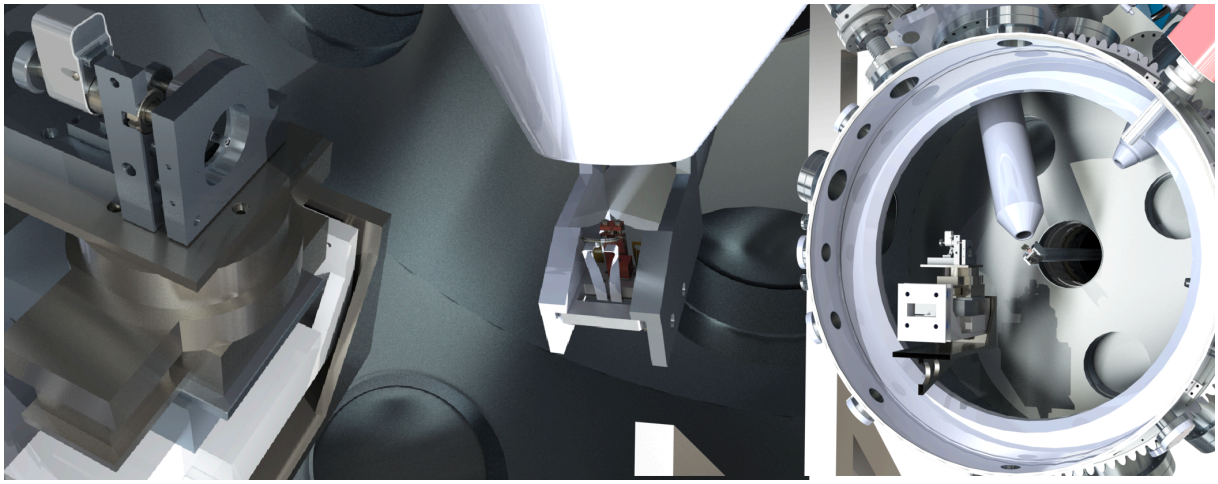

Figure 6.4: An drawing of the AS3's experimental chamber. The front face of the chambers have been removed to give the viewer a chance of looking into the chamber

part was meant to reflect and focus the incoming laser radiation onto a sample that was located in the center of the chamber. The inner part was meant to serve several functions. First, it would focus the XUV radiation onto the sample. The inner mirror was a multilayered mirror specifically designed and tailored to spectrally filter the incoming XUV radiation, reflecting only the cutoff region of the HHG radiation, resulting in an isolated attosecond pulse. The inner mirror could be swapped for another mirror tuned to filter different photon energies allowing us to adjust the used XUV photon energies of the attosecond pulse. The third function of the inner mirror was to tune the delay between the two pulses. This was achieved by a fine precision piezo stage on which the double mirror was mounted. The piezo stage would move the inner mirror in or out along the radius of the outer mirror. By doing so, the distance that the two pulses have to propagate would vary, ultimately adjusting the timing between them.

The experimental chamber was equipped with a TOF spectrometer and a hemispherical electron analyzer, both of which were mounted on a rotating mantle of the chamber, pointing at the center of it a with 15 degree angle. The rotating mantle allowed for selecting electron analyzer and the analyzed photoelectron emission angles. Furthermore, an X-ray source was located on the same mantle, pointing toward the center, allowing for X-ray photoemission spectroscopy (XPS) measurements on the sample when combined with the hemispherical detector.

A multichannel plate coupled with a phosphorus screen were also mounted on the chamber in the same height as the double mirror to allow for characterization of the spatial profile of the harmonic beam, and for the adjustment of the pellicle and the iris used to attenuate intensity of the laser beam. In order to drive the beam into the MCP setup instead of the double mirror, the

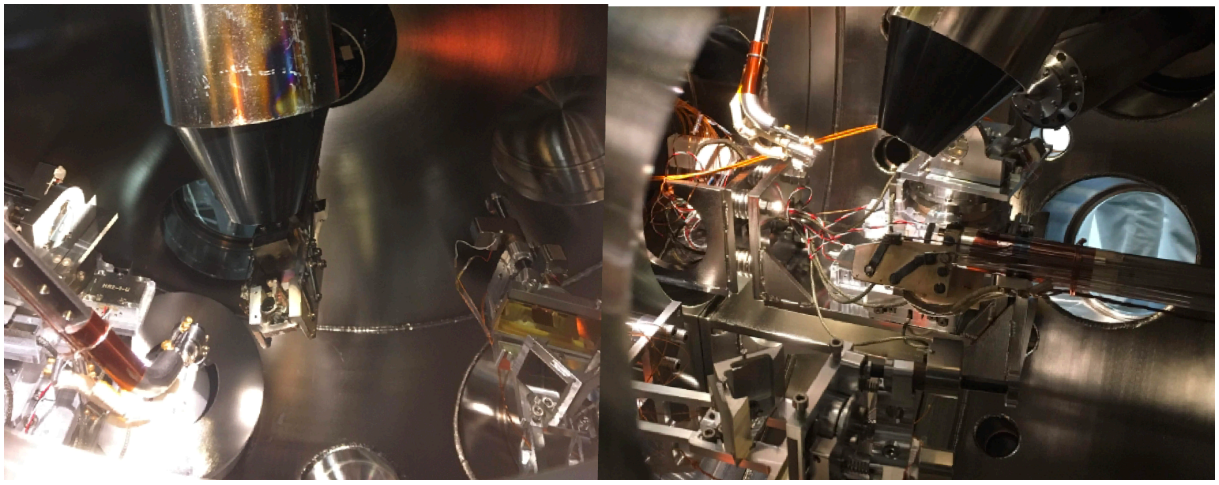

Figure 6.5: The experimental chamber of AS3 taken from different windows around the chamber. In these pictures the hemispherical analyzer is used.

experimental chamber that was mounted on pneumatic feet was rotated accordingly. Lastly, a mass spectrometer was mounted on the experimental chamber to allow for detection of specific elements and monitoring during the experiment.

The sample was mounted on a motorized manipulator arm and was driven into the center of the experimental chamber through a gate valve that connected the experimental with the preparation chamber. The preparation chamber was equipped for the preparation and analysis of the surface of solid state samples. As such, the chamber was equipped with an Ar-ion sputtering gun, a gas dosing system and several exchangeable evaporators. The sample holder was also specially designed to include filaments right below the sample, allowing for the controlled heating of the sample. The sample could also be put to high voltage to increase the efficiency of the heating system. The sample holder was also in contact with a cooling system using liquid nitrogen. Using both systems in combination with a thermocouple pair that was mounted on the sample, the temperature of the sample could be finely tuned. On the characterization side, the preparation chamber included a low energy electron diffraction (LEED) setup for monitoring the surface quality as well as a mass spectrometer that was used in combination with the evaporators and the temperature control system for temperature programmed deposition (TPD) measurements or for establishing the surface cleanliness. The surface quality and composition was also verified using the XPS setup in the experimental chamber.

The different preparation and monitoring setups were placed along the outer mantle of the experimental setup. The sample manipulator was mounted on the front face of the chamber which was rotatable, allowing the sample to be placed in front of each individual setup for

processing or characterization. When the front face of the chamber was rotated so that the sample manipulator was at its lowest position, the sample could be driven through the gate valve connecting the experimental and preparation chambers.

Lastly, a loadlock setup was located at the mantle of the preparation that allowed for the exchange of the sample without having to break the ultra high vacuum of the preparation chamber. It consisted of a small chamber with a sample holder mechanism mounted on a linear manipulator. The chamber had three openings, namely a gate valve to the preparation chamber, a small window that could expose the loadlock chamber into the atmosphere and a connection to a nitrogen tank. The sample was placed on the linear manipulator through the window opening, while the gate valve to the preparation chamber was closed, and while the loadlock chamber was supplied with nitrogen for reducing contamination from the atmosphere. The window was then closed and the supply of nitrogen was stopped. The loadlock chamber was pumped typically down to 10^{-8} mbar. At this point, the valve to the preparation chamber was opened and the sample was mounted on the experimental chamber's manipulator with the help of the loadlock's linear manipulator.

6.2 Mg-Phthalocyanine Organic Semiconductor Monolayer

In this section the efforts towards recording photo-excitation electron dynamics in MgPc self--assempbled monolayer on Ag(100) surface will be presented. This work was a collaboration between the group of Prof. Dr. Augustin Schiffrin, School of Physics and Astronomy of Monash University, the group of Prof. Dr. Karsten Reuter, Chair for Theoretical Chemistry of TUM, and the group of Prof. Dr. Reinhard Kienberger, Chair for Laser and X-ray Physics (E11) of TUM. The different groups focused on different topics around this subject in order to be able to preform the measurements.

Dr. Marina Castelli, Dr. Cornelius Krull, Dr. Jack Hellerstedt and Prof. Dr. Augustin Schiffrin developed a preparation method that would fit the AS3 chamber. They also characterized MgPc monolayers using scanning tunneling microscopy (STM) and scanning tunneling spectroscopy (STS) techniques and supplied us with photoemission cross section and energy dispersion curve (EDC) measurements of MgPc monolayers from the Australian Synchrotron.

Simiam Ghan and Prof. Dr. Karsten Reuter supplied us with density functional theory (DFT) calculations of the MgPc molecule as an isolated molecule and as a monolayer semiconductor on a silver (100) surface.

From the group of Prof. Dr. Reinhard Kienberger, Maximilian Schnitzenbaumer and I were in charge of the experimental efforts, with Pascal Scigalla, Christian Schröder, Michael Haimerl and Eckhard Schock contributing significantly. I also developed a computational model based on

what was discussed in the previous chapters and utilizing the results supplied to us by Simiam Ghan and Prof. Dr. Karsten Reuter in order to predict the expected effects and guide the experimental efforts.

6.2.1 MgPc Self-Assembled Monolayer on Ag(100) Surface

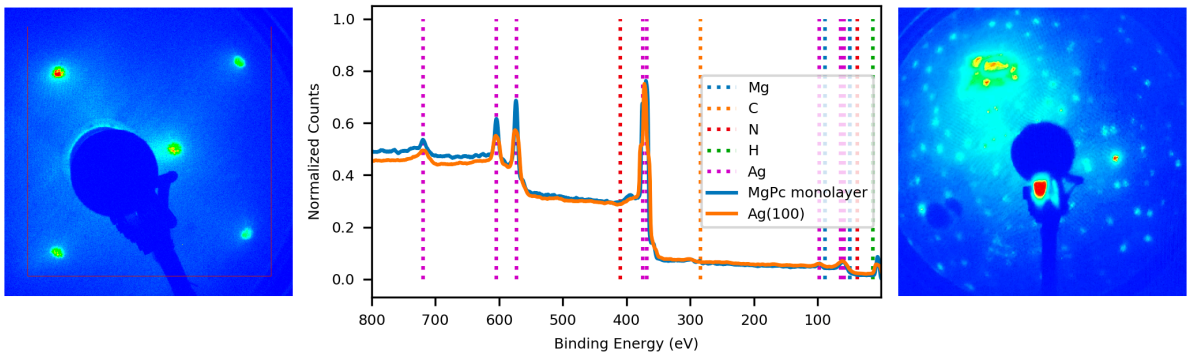

Figure 6.6: Typical surface quality characterizations of Ag(100) by LEED on the left, XPS characterization of clean Ag(100) and monolayer MgPc on Ag(100) in the center, as well as LEED characterization of MgPc monolayer on Ag(100).

Section 4.2 introduced the MgPc molecule and ways to prepare thin film semiconductors from it. It was mentioned there that the MgPc, as well as other Pc molecules, tends to form neat monolayers due to their flat geometry and symmetric shape which allow them to lock in place on a 2-dimensional array. For achieving this, MgPc molecules need to adsorb on a clean surface, therefore a clean surface has to be prepared in ultra high vacuum to keep any contamination from happening. To that end a monocrystalline Ag crystal was used with its (100) surface polished. Several cycles of 30 minutes long Ar sputtering were performed, with Ar background pressure of $2.5 \cdot 10^{-5}$ $mbar$ and estimated kinetic energies of 1.25 keV. The Ar ions induced a current in the order of 40 μA on the sample. The sputtering was meant to remove any contamination by chipping away the first layers of Ag together with the contaminants. Following every Ar sputtering, a heating cycle took place. During the heating cycle, the sample would be heated up to 600 K where it was allowed to stay for 10 minutes. After that time the sample was cooled at a rate of 1 K per second down to 300 K. The heating cycles were meant to allow the restructuring of the Ag surface. The surface quality was confirmed using XPS and LEED measurements as seen in Figure 6.6.

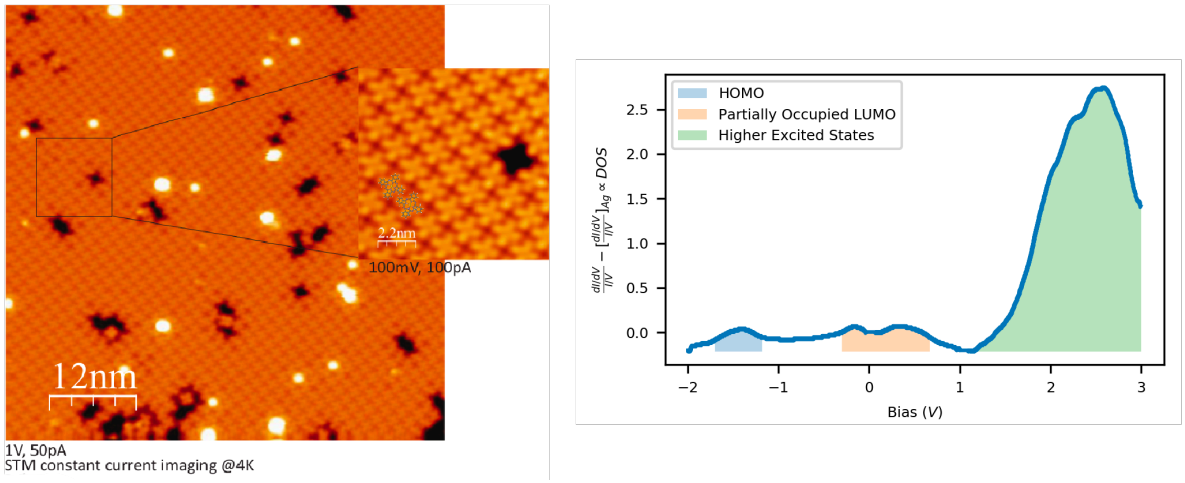

Figure 6.7: Characterization of MgPc monolayer on Ag(100) by STM on the left and STS on the right. The STM image and STS data were supplied to us by Marina Castelli.

MgPc molecules were supplied on the surface using an organic molecular beam epitaxy (OMBE) evaporator, which was filled with commercially available MgPc powder with 90% purity. As the adhesion between the individual molecule and the surface is greater than that between molecules stacking on each other, the probability of an evaporated molecule to adsorb on the surface is much greater. Once the surface coverage is great enough, the molecules start locking into place with one another, forming a high coverage organized monolayer film. When that happens, the LEED pattern of the surface gets a characteristic shape revealing the MgPc lattice symmetry (See Figure 6.6). To achieve this effect, the OMBE was heated at 420 K and let stay there for a few minutes before the output shutter was opened to allow for deposition on the sample. The sample was spaced approximately 10 cm away from the OMBE and the evaporation time for achieving a good monolayer was about 10 minutes. The process was very sensitive to the exact placement of the sample with respect to the OMBE, so fine-tuning of the process with the exact experimental conditions was always necessary.

Typical STM and STS characterizations of MgPc monolayer on Ag(100) are presented in Figure 6.7. On the STM one can see how the molecules lock in place forming the monolayer. The shadows are places where molecules are missing from the lattice, while the bright spots are molecules that are stacked on top of the lattice. The information obtained by the STS measurements is also critical for the understanding of the system. Three distinct features that are shaded in the right plot of Figure 6.7. The features have been identified as the HOMO, the LUMO, which seems to be partially occupied, and the higher excited states. In this plot, zero bias voltage corresponds to the Fermi level. The technique does not work at zero bias voltage,

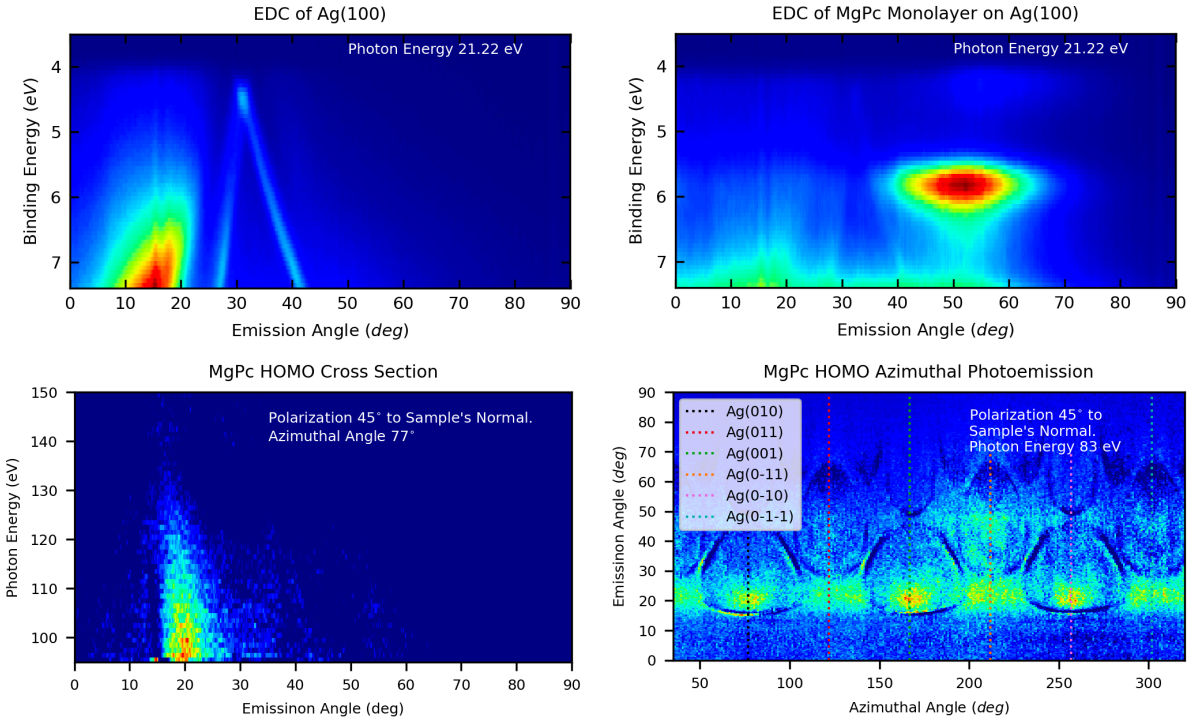

Figure 6.8: EDC of Ag(100) (top left) and MgPc monolayer on Ag(100) (top right). Photoionization cross section (bottom left) and azimuthal emission scans for the HOMO orbital of MgPc monolayer on Ag(100) surface. The data were supplied to us by the group of Prof. Dr. Augustin Schiffrin.

thus the LUMO appears to be split in two peaks.

As a part of the characterization of the MgPc monolayer on Ag(100) surface, EDC curves and results of a photoemission study using synchrotron radiation which can be seen in Figure 6.8 were supplied to us by the group of Prof. Dr. Augustin Schiffrin. For the EDC of Ag(100) it is clear that its emission is localized between 0 and 20 degrees and then at 25 to 45 degrees. For the EDC of MgPc monolayer, there are two principle features centered around 5.7 eV and 4.2 eV that emit photoelectrons in the range of 40 to 65 degrees. The two features are the HOMO and the partially occupied LUMO states of the molecule. It should be noted that, in this measurement, the binding energy is shown, thus zero is the vacuum level, not the Fermi level. Using the information from the EDCs, the detector's parameters were fixed in order to analyze only the binding energy of the HOMO state, while other experimental parameters were changed. By changing the central photon energy of the radiation, a photoionization cross section study was conducted (Bottom left plot in Figure 6.8). It can be noted how, for the given photon energy range the emission angle has reduced to approximately 20°. The cross section

intensely reduces as the photon energy increases. By varying the azimuthal angle of the sample, the emission along the azimuthal angle was recorded. We can see that the emission from the HOMO state maximizes along the principle directions of the crystal. All measurements were performed with a polarization of the radiation at 45° with respect to the sample's normal. This was done because there was no emission when the polarization axis was perpendicular to the sample's normal, while the setup would not allow for a polarization parallel to the sample's normal. The value of 45° was a necessary compromise, which revealed some facts about the polarization dependence of the photoemission.

6.2.2 DFT Calculations of MgPc Monolayer on Ag(100) Surface

Recording the photo-excitation dynamics on such a system is a non trivial task. The experimental parameters need to be perfectly tuned if there is to be any chance of success in such an experiment. The complexity of the problem and the experimental apparatus is such that allows no room for errors. Therefore, a significant effort was put into predicting the signal and the properties of the molecule so that the optimum experimental parameters would be picked.

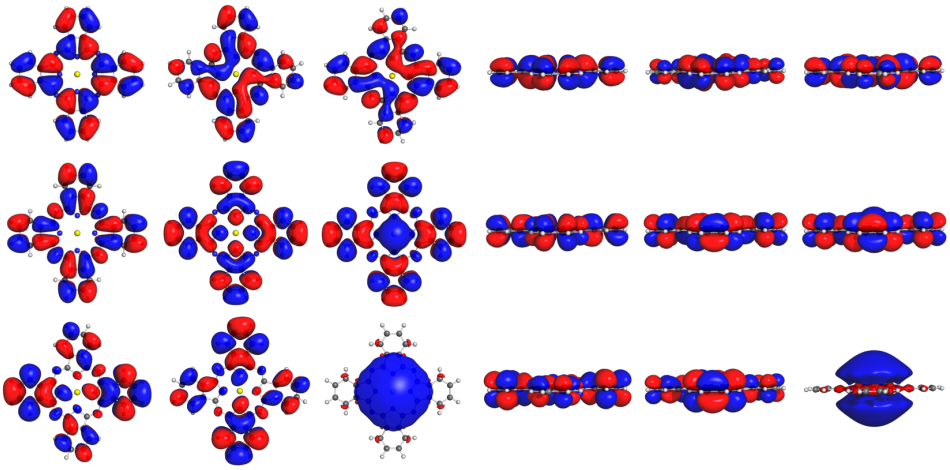

Figure 6.9: DFT calculation predicted position dependent part of the wave function for isolated MgPc molecule using hybrid functionals (TIGHT-b3lyp). The alpha orbitals (spin up) from HOMO to LUMO+7 are depicted in a 3×3 matrix. Two matrices are shown. One depicting the molecule from above (left) and one from the side (right).

As shown in Chapter 4, when considering interband dynamics of MgPc, laying in the visible range, it is reasonable to skip the semiconductor picture for a molecular picture, since the molecules are spaced far enough so that they form a band structure with energy dispersions significantly lower than the interband distances. It was also demonstrated that the intermolec-

ular effects, although significant, play a role in timescales that are much larger than what this section is concerned with. Therefore, the first order approximation will be an isolated molecule and attention will be drawn only on its singlet states.

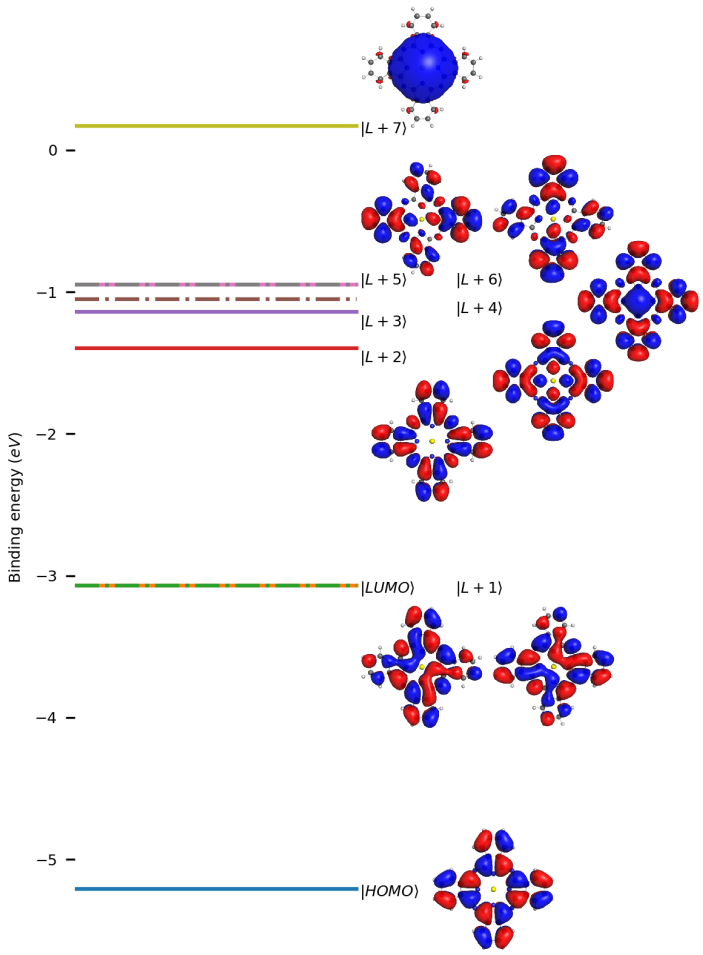

Figure 6.10: DFT calculation predicted eigenenergies for isolated MgPc molecule using hybtid functionals (TIGHT-b3lyp). The alpha orbitals (spin up) from HOMO to LUMO+7 are depicted.

A thorough understanding of the molecule, its structure and behavior can be reached by performing a DFT calculation for it. The orbitals of the most relevant states predicted by such calculations can be seen in Figure 6.9. It becomes apparent that the states are rather delocalized on the ligant of the molecule. It is also apparent that LUMO and LUMO+1 are identical but

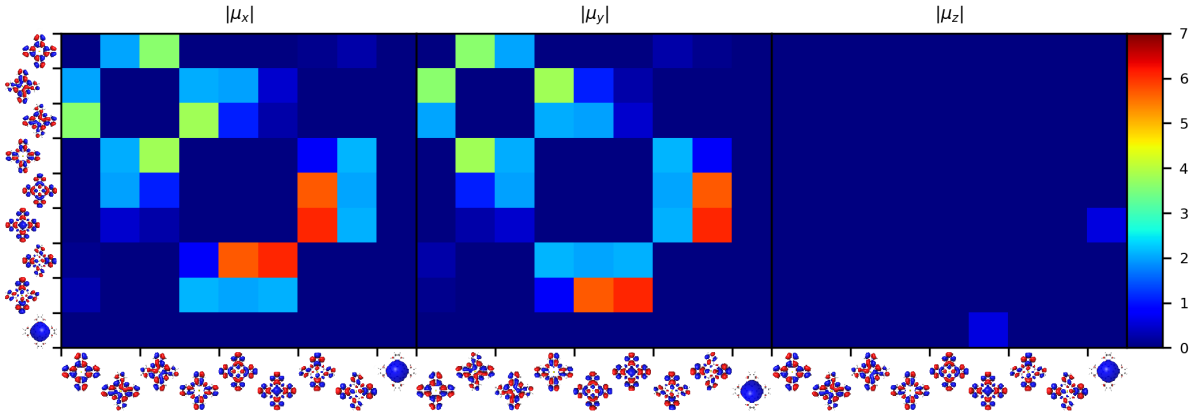

Figure 6.11: DFT calculation predicted dipole moments for isolated MgPc molecule using hybtid functionals (TIGHT-b3lyp).Three matrixes are shown for the dipole along the x, y, and z directions, where the molecule lies on the $x-y$ plane. The absolute value of the dipole matrix is depicted. The alpha orbitals (spin up) from HOMO to LUMO +7 are depicted.

rotated by 90 degrees. The same is true for LUMO+5 and LUMO+6. These pairs of states are degenerate. The degeneracy relates to the symmetry of the molecule. The next interesting orbital is the LUMO+7, which is localized towards the center of the molecule. We can also see that this state extends the furthest along the z direction (assuming the molecule lies on the $x-y$ plane.)

Figure 6.10 depicts the eigenenergies of the same set of states. It can be noted that HOMO and LUMO are about 2 eV apart. LUMO and LUMO+1 and LUMO+5 and LUMO+6 are really degenerate. From 1.7 eV to 2.2 eV above the LUMO and LUMO+1 states there is a second group of closely packed states, forming the B-Band of MgPc. An eV above the B-band is the LUMO+7 state, which is predicted to be above the vacuum level and thus a free electron state. The eigenenergy values predicted by DFT calculations are typically not very accurate, however they do represent the reality. Divergences in the exact eigenvalues are expected in the context of an experiment.

The next major insight gained would be the dipole matrix. Which will define the polarization direction that the driving field needs to have in order to drive transitions on the molecule. Such matrices can be seen in Figure 6.11, where the absolute value of the dipole matrix is given in color. Three matrices are given for transitions along the x, y, and z directions. It can be seen that the matrices for the x and y directions are complimentary to each other, while by orienting the electric field along the z direction (or the molecule's normal) only one transition from LUMO+4 to LUMO+7 can be driven. Knowing how the molecule lays flat on the surface and by trying to conduct the experiment the usual way for attosecond streaking spectroscopy

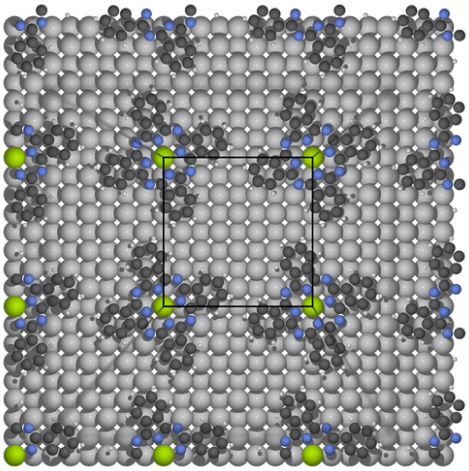

Figure 6.12: MgPc molecules on Ag(100) surface.

(field polarization parallel to the surface normal), it can be concluded that no signal would ever be possible. What is needed is a decent amount of the driving field to be in the $x - y$ plane.

At this point the major insights that DFT calculations had to offer for predicting the principle nature of the molecule and its interaction with light have been presented. Still, further investigations were made in which the MgPc molecule was simulated onto a slab of silver atoms, along the (100) surface. From these calculations, the group of Prof. Dr. Karsten Reuter was able to predict that the molecules lock in place 18° with respect to the Ag (010) principle direction, as well as obtain really good estimations of the DOS of such a system that matches the data shown in Figure 6.7. The partially occupied LUMO state was also explained by these calculations.

6.2.3 Deducing the Experimental Parameters

From the previous two sections, a very clear picture of the molecule and how it behaves should have been shaped. Now what remains is to determine the optimum experimental parameters and possibly make a prediction of the signal and whether it could be detected. To achieve that, decoding the information provided in the previous chapters is necessary. The EDC reveal a preferred photoemission zenith angle, which does not directly translate to the angle that must be used in the attosecond transient photoemission experiments, since the spectra for EDC were recorded with a given photon energy (21.22 eV). During the photoionization process, the parallel to the surface component of the electron momentum is preserved, while the parallel to the surface normal is set by the photon energy minus the binding energy. An expression to transforming the angle of a given photoemission to an angle for a photoemission with different photon energy

can easily be deduced. Such an expression will be:

$$\sin\theta_f = \sqrt{\frac{E_i}{E_f}}\sin\theta_i \tag{6.1}$$

where θ_f and θ_i are the final and initial angles and E_f and E_i the final and initial kinetic energies of the electron (which can also be substituted for the photon energies for both).

For the photon energies that are going to be used (85 eV and 99.5 eV), the photoemission of MgPc is between 20° and 21° and extends about 5° around that value, as seen in Figure 6.8. It is also benefitial to orient towards higher angles rather than lower ones, since a few degrees lower than the HOMO emission there is a sharp emission from silver that should be avoided. When it comes to the azimuthal angle it was found that the emission maximizes towards the Ag(0±10) and Ag(00±1).The LEED can therefore be utilized to deduce the orientation of the Ag(100) sample and place it in a way that the detector is tilted approximately 21° from the sample's normal in one of the aforementioned crystal directions.

The next major chapter is the polarization of the laser's infrared few cycle femtosecond and the harmonic XUV attosecond pulses with respect to the sample's normal. There are contradicting requirements on this front, since, for photo-excitation to happen, the infrared pulse needs to be perpendicular to the sample's normal, while for photoemission to happen, the XUV polarization needs to be parallel to the sample's normal. The way the experimental apparatus was designed, it cannot select polarization axes independently, since the harmonic radiation follows the polarization direction of the fundamental beam. A compromise of 45° will be the solution here, as it provides equal components in both orientations. The added bonus is that this polarization is the same as the one used in the photoemission studies, ensuring that these experiments are replicated, but with different photon energies. The orientation of the molecule with respect to the Ag(010) direction is also known. The incident radiation is oriented 90° to the detector's azimuthal, which results in the incoming radiation being towards the Ag(001) direction. Thus, resulting in the incoming radiation being oriented 18° to the principle axis of the molecule.

Another important decision is the photon energy and the bandwidth of the XUV pulse, which can be selected by selecting the inner part of the double mirror. There are some technical details that have to be weighted in our decision. The spectrally narrower pulses that available by the setup would have a bandwidth (FWHM) of 0.8 eV and are a central frequency of 99.5 eV. This is due to the silicon edge which is used to reduce the bandwidth of the reflection from the inner multilayered mirror. On the other hand, the photoionization cross section strongly favors the lower kinetic energies, which are also more surface sensitive, since the penetration depth of the

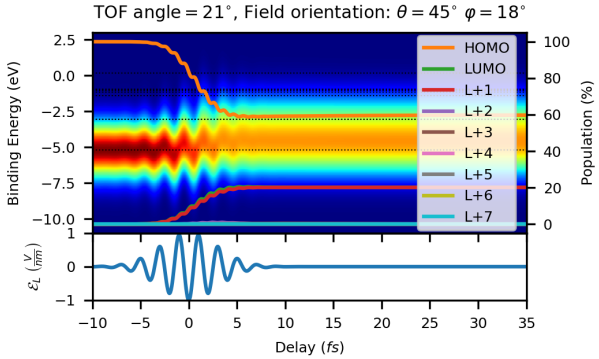

Figure 6.13: Calculation of the photo-excitation dynamics for isolated MgPc molecule. The experimental parameters have been set to the values determined in the text. The pulse parameters have been set by retrieving attosecond spectrograms of similar experiments and applying those parameters to the simulation.

XUV pulse is reduced, thus a greater portion of its energy is used to excite photoelectrons from the surface rather than the bulk. The practical limitation is our ability to isolate attosecond pulses. The task becomes unreliable at photon energies below 80 eV. We will thus have to probe at least two photon energies at the optimum of XUV bandwidth and the optimum of cross section. For the time being, more emphasis will be placed on the region of 99.5 eV, where the optimum spectral resolution of the technique can be ahieved.

The calculations of the dynamics of an isolated MgPc molecule will be presented first. The molecule has been placed on the $x-y$ plane. All angles are measured as in a spherical coordinate system. In Figure 6.13 the results of such a calculation are presented. The binding energies for each state are marked with a black dashed line. The calculations included up to the LUMO+7 state which is said to be the first unbound state. It can be observed that for the conditions picked here a total of 40% of the population ends up in excited states. Mainly the degenerate LUMO states are almost equally populated. During the pulse, a small percentage of the population moves to higher excited states but quickly returns to ground state before the pulse ends. The streaking trace is considerably shifted toward the LUMO states after the overlap region and some dissipation starts taking place within the first 35 fs.

From Figure 6.12, a rough estimation of 30 Ag atoms per layer per MgPc molecule can be made. If only the first layer of the Ag crystal is considered to contribute to the photoionization signal, then we can try to simulate as a 1:30 the signal intensities from MgPc and Ag respectively. All notions of photoemission cross section and directionality will be skipped here, since the only reliable method for deducing those parameters would be specifically designed experiments. Thus, only a rough estimate of the streaking traces can be obtained as expected from the setup. Such

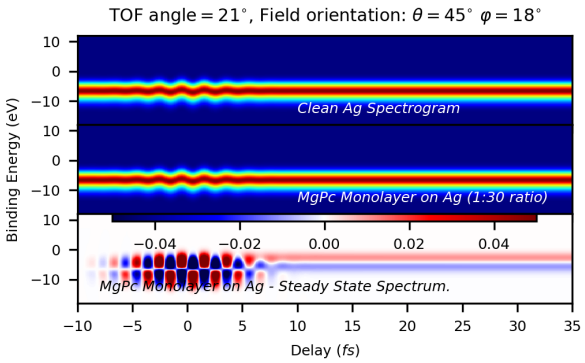

Figure 6.14: Estimation of the streaking trace for Ag under the selected parameters (top). A combination of 1:30 of the estimated MgPc and Ag spectrograms (middle) and lastly the same, where a reference spectrum has been subtracted to reveal the signal (bottom).

calculations can be seen in Figure 6.14. From these calculations the expected signal intensity after the overlap region seems to be in the order of 1% of the observable photoelectron peak. Assuming that the cross sections and the photoemission directionality work to enhance this effect, then an observation could be realized.

6.2.4 Experimental Findings from MgPc monolayer on Ag(100)

To adjust the polarization of the radiation, a periscope was used to tilt the polarization of the laser pulses before the HHG process in such a way that the 45° angle to the sample's normal was established. The 21° for the photoelectron detection could be realized by constructing a specialized sample holder that, instead of tilting the sample up by 15° upward to match the TOF geometry, it tilts the sample 6° downward, giving a total of 21° from sample's normal to TOF. The analysis methods presented in the previous chapter demand good reference spectra. The prediction of the signal's intensity also suggests that good referencing would be essential. For this reason, a chopper wheel was included to block the laser pulse of every second shot, leaving the harmonic radiation to propagate further. This way, an unpumped reference spectrum could be recorded in real time together with the pumped spectrum. The inner mirror was selected to have have a bandwidth (FWHM) of 0.8 eV and central photon energy of 99.5 eV. The best compromise between bandwidth, pulse duration and cross section was thus made. The outer mirror was selected such that it favours the reflection of 2 eV, without leaving the 1.5 eV components, in hope that the excitation from HOMO to the partially unoccupied LUMO and the partially occupied LUMO to higher excited states would also be resonant, following the DFT and dynamics simulations, as well as the STS measurements.

Once all experimental parameters described in the previous section were realized, it was time

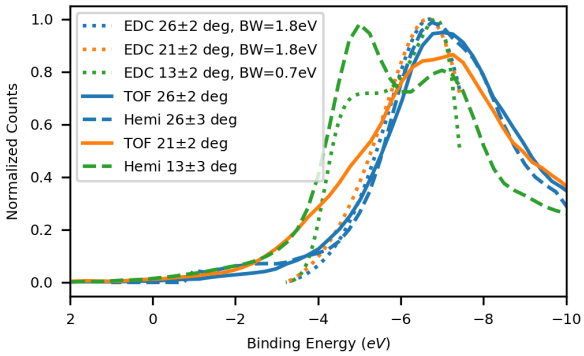

Figure 6.15: Calibration on the photoemission of Ag(100). Photoelectron spectra of Ag(100) at different emission angles were recorded using the TOF (solid lines) and hemispherical analyzer (dashed lines). From the EDC plots photoemission spectra were also generated for different parameters and overlaid with the data (dotted lines).

to perform the experiment. The first task was to calibrate the detectors and confirm that the photoemission angles were as expected. The time of flight spectrometer which was our most sensitive detector is sensitive to alignment and thus the act of moving the sample for preparation purposes or just change the spot on the sample where the radiation hits can lead up to 0.5 eV shift of the photoelectron peak's kinetic energy. To account for that, a series of measurements was performed utilizing both the TOF and the hemispherical analyzer using clean Ag as our sample and taking advantage of the knowledge gained by the EDC. Results from that study can be seen in Figure 6.15. The EDC that were supplied to us were used to generate an estimation of the spectra for the angles recorded here. The generated spectra were used to calibrate the binding energies and provide an estimation of the actual spectral resolution of our detectors. As it can be seen here, a bandwidth of 1.8 eV (FWHM) or more is necessary to match the experimental data with the EDC generated spectra, while the XUV bandwidth is supposed to be 0.8 eV (FWHM). The cause of this mismatch will be discussed at a later point. What this implied, though, is that minimizing the XUV bandwidth was not as effective as expected. Recording the Ag photoemission spectrum at 13° emission angle was specifically done to allow for the calibration, since it corresponds to the EDC in the range of 30°, resulting in two peaks. The bandwidth of the EDC generated spectrum at 13° was left at 0.7 eV to make the distinct peaks more prominent and allow for the calibration of the spectra. The unavoidable mismatch between the EDC generated and the measured spectra came from neglecting the effects of the photoionization cross section. In addition, the EDC-generated spectra tend to decrease below 6.5 eV since there were no data available below 7.5 eV, and thus when the convolution with a gaussian was made to include the bandwidth, the lines stopped overlapping, reducing the result

of the convolution.

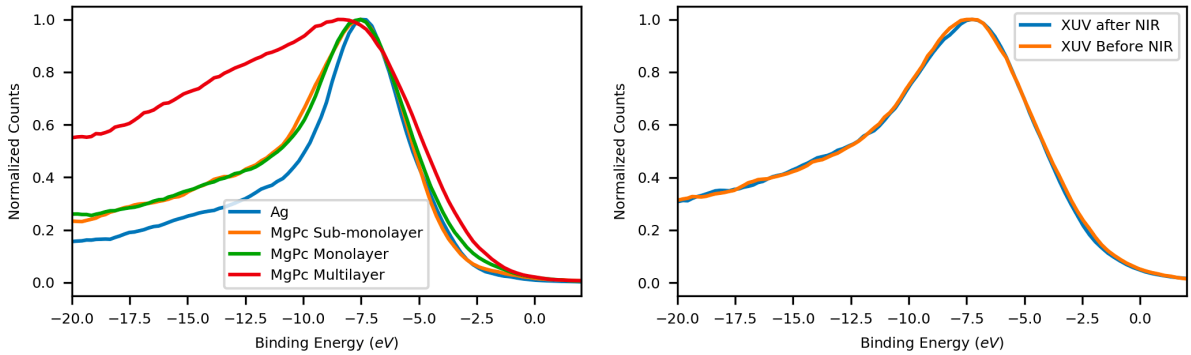

Figure 6.16: Identification of the effect on the photoelectron spectrum of MgPc deposition on Ag(100) (left plot). Comparison of photoelectron spectra of MgPc monolayer on Ag(100) surface for pumped and relaxed MgPc. All spectra shown here are recorded at an emission angle of 21°.

It was understood that recording the dynamics and the streaking are not complementing procedures, recording the streaking is wasteful in the sense that it requires numerous scans to resolve it nicely, while the dynamics need extremely long averaging times to have significantly high signal to noise ratio. Meanwhile, the maximum of the signal can easily be observed after the streaking, while during the streaking, there is a good chance that the signal is not even retrievable in the first place. For this reason a couple of streaking traces were initially recorded to prove the quality of the alignment and the pulse overlap inside the chamber. Then the efforts were focused on establishing an understanding of the photoelectron peaks. Such results can be seen in Figure 6.16. An observable difference is noticeable between the photoemission spectra from the valence band of clean Ag(100), MgPc sub-monolayer, monolayer, and multilayer on Ag(100) (left plot of Figure 6.16). The presence of the MgPc layer is immediately evident from the secondary electrons that are inellastically scattered on it and then recorded at lower binding energies. A subtle increase at the less bound electron side of the spectrum can also be observed. Spectra before and after the overlap were recorded (right plot of Figure 6.16), effectively recording pumped (blue line) and un-pumped (orange line) spectra. Here, a very subtle shift of the pumped spectrum to higher binding energies with respect to the un-pumped spectrum can be observed which is within the measurement error, but was also systematic. It was in the opposite direction of what was expected and, apart from the lower binding energies, it seemed to affect the entire spectrum.

Upon analyzing the recorded data, an emission difference from Ag could be established as seen in Figure 6.17 in the order of a few percents of the total photoionization peak. Once the

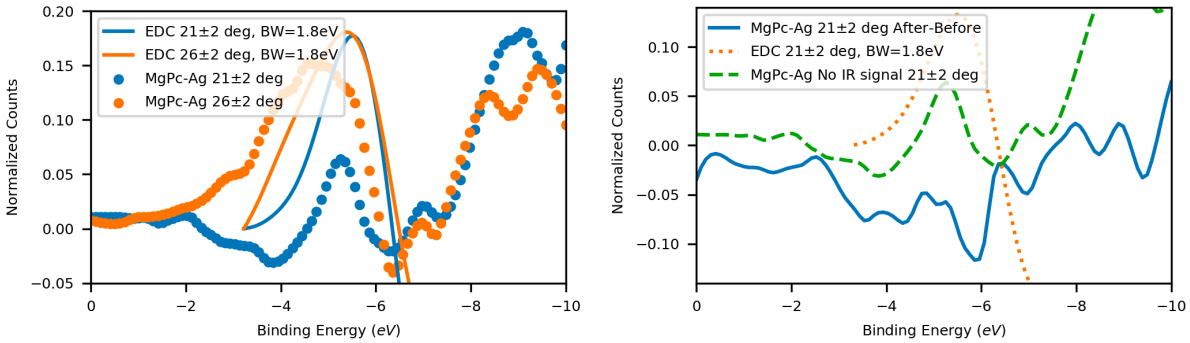

Figure 6.17: Subtraction of Ag(100) photoelectron spectrum from MgPc monolayer on Ag(100) photoelectron spectrum (left plot). Recorded data (points) are overlaid with calculations from the EDC (lines) for photoemission angles of 21° (blue) and 26° (orange). The difference between pumped and un-pumped spectra (right plot) for an emission angle of 21° (blue line). The spectrum difference between MgPc monolayer on Ag(100) and clean Ag(100) is repeated for the reader to keep track of the expected signal position from EDC generated spectra (orange dotted) and recorded data (green dashed).

subtraction between the pumped and un-pumped spectra is made a negative signal is revealed, caused by the shift which was noted above. Once that happens, even the difference between the MgPc monolayer on Ag(100) and clean Ag(100) photoemission could not be observed. The experiments were repeated at an emission angle of 26° to avoid any accidental error in the experimental determination of the photoemission angle that could result in the Ag(100) emission being recorded by our detectors, increasing the background signal and reducing the sensitivity. By doing so, a larger difference between the MgPc monolayer on Ag(100) and the clean Ag(100) photoemission could be established, but yielded equivalent results, where the difference could not be traced out once photo-excitation took place.

It was evident at this point that the experiment had little to no chance of succeeding since the experimental spectral resolution was less than expected, and the photoionization signal from MgPc was already limit of detection, so a difference of up to 40% on that would barely be recognizable, not to mention a parasitic effect that seemed to mask the signal. Still, one parameter was left that could improve one of those parameters, namely the signal to background ratio, due to the photoionization cross section. We proved that a bandwidth of 0.8 eV is ineffective since the bandwidth of the setup seems to be limited to values around 2 eV. Thus it was possible to repeat the experiments at lower photon energies. To this end, an inner mirror with a bandwidth of 1.5 eV and central photon energy of 85 eV was selected.

In Figure 6.18 a direct comparison of MgPc monolayer on Ag(100) and Ag(100) photoemission at a detection angle of 21° can be seen. Once again, there is an noticable difference between

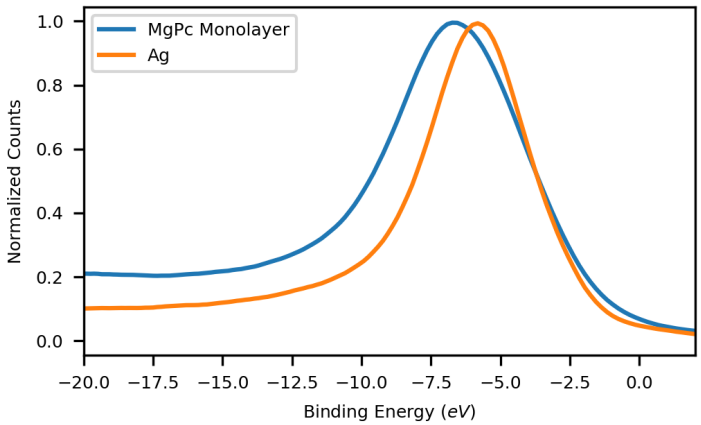

Figure 6.18: Comparison of photoelectron spectra of MgPc monolayer on Ag(100) (blue) and clean Ag(100) (orange). All spectra shown here are recorded at an emission angle of 26°.

the Ag(100) and MgPc(100) photoemission. Proceeding to the measurements, the same parasitic effect was observed again, only this time it was more pronounced and could be precieved during the experiment. This provided an opportunity to document it systematically, as can be seen in Figure 6.19. In order to record the evolution of this effect with respect to the delay, several spectra were recorded across the complete range of delays available (Figure 6.19 left plot), revealing a shape of gradual increase of the photoelectrons kinetic energy as the delay approaches zero from negative values (XUV arrives at the sample before the laser). At delay zero, the line seems broader and delocalized due to streaking, since only one spectrum was recorded within the overlap region. As the situation inverts the behavior changes and a more sudden decrease of the photoelectron's kinetic energy happens as the delay values increase from zero to higher positive values (XUV arrives after the laser at the sample). The photoelectrons kinetic energy asymptotically decreases down to the expected value as the delay increases further.

In order to record the intensity dependence of the effect, several photoelectron spectra of MgPc monolayer on Ag(100) were recorded at a set negative delay value. The iris in front of the pellicle was used to attenuate the power of the laser. The effects that the laser's power had on the photoelectron spectra can be seen in Figure 6.19 (right plot). As the power increases the photoelectron peak shifts to higher kinetic energies and the spectrum gets broader. This is one of the reasons for the loss of spectral resolution in our experiments. This effect is recognized as the pump induced space-charge effect [93] and is caused by a low energy electron cloud released by the laser's pulse in addition to the XUV photoelectrons. The electron cloud acts on the XUV photoelectrons modifying their kinetic energy. Since the XUV photoelectrons are much faster than the pump induced electron cloud, they inevitably end up spending more time propagating

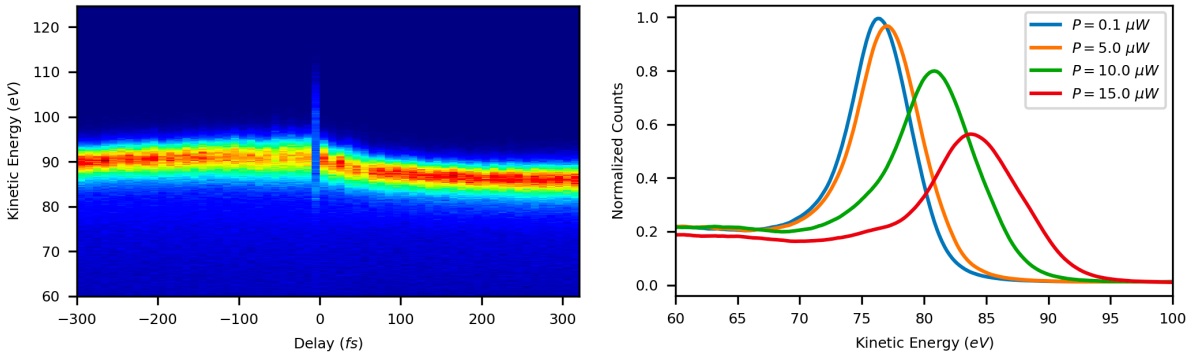

Figure 6.19: Recording of photoelectron spectra of Ag(100) in the full range of delays available on the AS3 chamber setup (left). Photoelectron spectra of MgPc on Ag(100) recorded at a fixed delay value versus the laser power at the target (right). The power measurements recorded here are estimations and only relate to each other, as they are heavily dependent on the specific setup parameters.

past the electron cloud toward the TOF and thus always gaining energy. The maximum energy is gained at zero delay, where the time that the XUV photoelectrons are pushed toward the TOF is maximized and the time that they spend below the electron cloud being pushed away from the TOF is zero. The asymmetry in the shape of the effect is caused by the XUV photoelectrons having to pass through the slow electron cloud for positive delays (XUV arrives after the laser at the target), which leaves the XUV photoelectrons with only a small net gain of energy that does not vary drastically for large delays.

Another reason for the loss of spectral resolution, even when the pump induced space-charge effect is small, would again be a space-charge effect (see Appendix A), only this time it is the self induced space-charge effect. As our laser system has a 12 W output at a repetition rate of 4 kHz, there is plenty of energy per pulse to generate a decent flux of harmonic radiation, which in turn generates a number of electrons per shot. The electrons have to propagate approximately 75 cm to reach the detector. This cloud of electrons is acts on its outermost layers accelerating the forward electrons and decelerating the lower ones. This causes an inevitable broadening of the observed photoelectron peaks. In measurements where the spectral resolution is not a critical parameter, such as in the attosecond chronoscopy, the self induced space-charge effect is not that important. For cases such as the experiments we tried to implement, it can prove catastrophic.

Between the two space-charge effects that severely limit the resolution of the used instruments as well as the ability to track weak signals along the delay and the vanishingly small intensity of the MgPc signal with respect to the underlying Ag background, we can conclude that there is

no sensible way to detect the photo-excitation of this system with the existing instrumentation.

6.3 GaSb Semiconductor Wafer

Although the work on the MgPc molecule was terminated with a negative result, there was still a window of implementing some improvements to the main idea and trying again. The MgPc monolayer definitely had to be replaced by something more advantageous. In the previous project one of the main problems (other than the space-charge effects that are inherent to our measuring method) was the signal to background ratio and the photo-excitation percentage on that. It is possible that, should more drastic changes be induced on a material's population, the signal would be more pronounced and traceable, which would allow us to counteract the pump induced space-charge effect (see Appendix A) and retrieve the dynamics. To achieve this all notions of molecules on surface have to be dismissed, as there will always be some contribution from the substrate which is bound to drown the signal, as was the case for the MgPc on Ag(100). Performing the experiment on gas phase is possible, but the molecular alignment cannot be easily implemented, especially in a setup like the one available. The solution would be a semiconductor wafer, where the substrate is also the photo-exciting material. The quality of the semiconductor can be very good, which would allows for pre-calculation of the signal strength and whether this could be observed in the experiment.

Gallium Antimonide (GaSb) is a III-IV type semiconductor with Zinc Blende crystal structure and was selected for its availability and low band gap of 0.726 eV, allowing for the entire spectrum of our laser pulse to be resonant. A further advantage of using this semiconductor is that transitions can be driven along any direction of the material, thus the standard setup for the attosecond streaking spectroscopy would fit to our purpose without any further modifications. It was hoped that a greater percentage of electrons can be excited possibly with lower pulse intensities to minimize the pump induced space-charge effect. The self induced space charge effect cannot be counteracted, thus a loss of resolution from it should be taken for granted. The cross section will not be much of a concern either, as the detection of the valence band is the only important criterion.

For this study, a Zn-doped p-type GaSb(100) wafer was supplied to us by Dr. Ralf Meyer, Walter Schotky Institute, as well as knowhow of appropriate treating of the sample. From the group of Prof. Dr. Reinhard Kienberger, Maximilian Schnitzenbauber, Pascal Scigalla, Michael Haimerl, Eckhard Schock and I were involved in the experiments. Maximilian Schnitzenbauber and I developed the idea for this work. The DFT calculations were performed by Maximilian Schnitzenbauber using ready made packages [94, 95], while the Dynamics calculations were performed by me. Christian Schröder significantly contributed towards the development of the

project and the calculations.

6.3.1 Dynamics Calculation On GaSb(100) surface

As with any other part of this work it makes sense to try and estimate the expected signal and deduce whether the attempt is worth the effort. To this end, some extension of the theoretical model to include intraband effects seems necessary. Starting from the Lindblad equation (Equation 3.96) one term can be added to account for the changes in the electron's quasi-momentum inside the lattice which is caused by the laser's electric field $\mathcal{E}$, or otherwise the laser induced current in the crystal. The equation that describes this problem is the following [26, 27, 96]:

$$\frac{\partial \rho}{\partial t} = -\frac{i}{\hbar}[H, \rho] - \mathcal{L}\rho + i\mathcal{E}\frac{\partial \rho}{\partial \mathbf{k}} \tag{6.2}$$

where the density matrix has a new degree of freedom along the momentum k. A custom solver has been implemented for solving the above equation, since the number of states that now extend into a new dimension increased to such an extent that the libraries implemented in the previous sections reached their limits and were incapable to perform the calculations. This causes no surprise as their original purpose was to handle a problems involving small systems like a few coupled qubits.

A Kohn-Sham DFT calculation of the semiconductor system took place first, using readily available software [94, 95]. From these simulations an estimation of the band structure was made and the dipole matrices were generated. The excited state band was offset slightly in energy to better match the literature values of the band gap. The band structure that was calculated can be seen in Figure 6.20. Here, the band at 13 eV binding energy is not involved in the photo-excitation. Bands 3 and 4 are almost identical, while band 2 exhibits the highest dispersion. Band 5 was the only one kept to be used as the conduction band. The Fermi energy was arbitrarily selected to lay in the band gap, as it would play no active role in what we were interested in. The valence band is assumed to be fully occupied.

Equation 6.2 was integrated with the typical initial conditions and pulse parameters that match the simulations performed in the previous section. The polarization direction was set to match the sample's normal. The detection angle was also set to the same value, since the band structure calculated here is along this direction. The occupation of every state for every delay value can be seen in Figure 6.20 (bottom plot). There it can be seen that our radiation is resonant away from the center of the band structure, where the band gap is minimum. This ensures resonance with as many states as possible, causing the maximum possible photo-excitation with the least amount of laser intensity. It can be seen that band 3, as it exhibits the highest

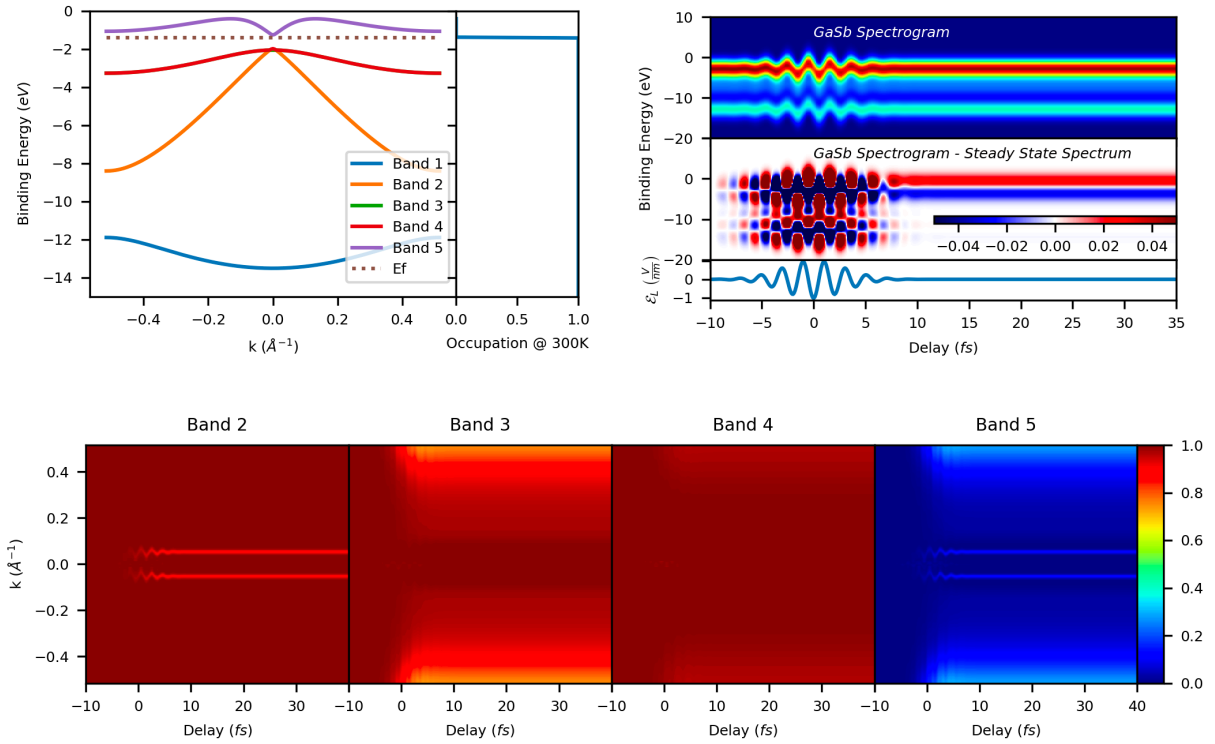

Figure 6.20: Calculation of the band structure of GaSb(100) along the sample's normal (top left). Simulating the photo-excitation dynamics signal in a streaking trace (top right). The simulated occupation across the four upper bands as a function of delay and wavenumber k (bottom).

dispersion is only resonant for a short range of wavenumbers contributing to the photo-excitation but only slightly. The most effect in the photo-excitation is accomplished by band 3, slightly complemented by band 4, both of which are resonant for large wavenumbers, but for a much broader range. It is notable that where there are holes opening in the valence bands (or electrons in the conduction band) they seem to be oscillating within the band following the pulse of the laser. These intraband transitions are caused by the term we included in Equation 6.2 which allows charge to acquire or lose quasi-momentum (or crystal momentum), given that there are free states in the band to be populated. The band structure is periodic, so the electrons leaving the band structure depicted here on one side equal the electrons entering the band structure depicted here from the other side.

As done for the case of MgPc, from each state a streaking trace is generated weighed by the occupation calculated and then all individual traces are added up to form a single streaking spectrogram as seen in Figure 6.20 (top right plot). Then, a steady state spectrum is subtracted

from all individual spectra to reveal the signal. In this case the total photo-excitation signal is found to be in the order of 3-4% of the total photoelectron amplitude, which is a significant improvement from the case of MgPc, where the signal was in the order of 1% in the calculations. However it is still far from ideal, as it will be hard to locate and track, knowing the experimental flaws. Since this was the last viable scheme for direct measurements of photo-excitation in the AS3 setup and as there was some improvement in the predictions it was decided to proceed with the measurements.

6.3.2 Experimental Findings From GaSb(100)

A GaSb(100) wafer that was provided to us was glued with a metallic conductive glue onto a metallic sample holder in order to establish a good connection to ground. For the experiment the 99.5 eV inner mirror was selected, with 0.8 eV bandwidth (FWHM) since no limitation on the cross section was present and having the best possible spectral resolution could prove useful. The outer mirror was the same as the experiments with the MgPc monolayer.

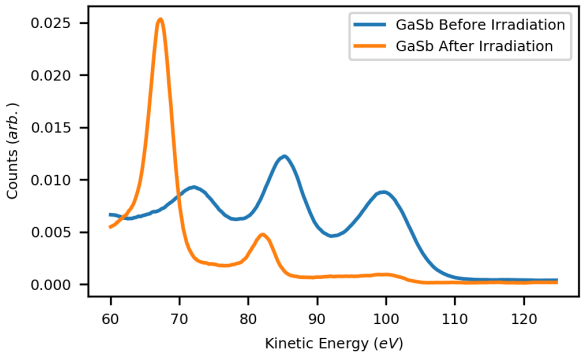

Figure 6.21: Results on the photoelectron spectrum from optical damage of GaSb(100) wafer.

Soon after trying to obtain the first streaking traces with the GaSb(100) wafer, another unexpected limitation presented itself. When irradiating the sample with typical intensities used in the attosecond streaking spectroscopy, optical damage of the crystal would occur. Typical spectrum of GaSb(100) wafer before and after intense irradiation can be seen in Figure 6.21. Clearly, the spectrum of the sample severely changes and it does not return to its original form as the structure of the sample has been permanently altered. A new spot on the crystal could then be used to proceed with the measurements. The optical damage was not instant in all cases. If slightly lower intensities were to be used, it would take some time for the damage to occur on the crystal. Reducing the intensity slightly more the sample would not be damaged even after long exposure to the radiation. Under these conditions all of the measurements took

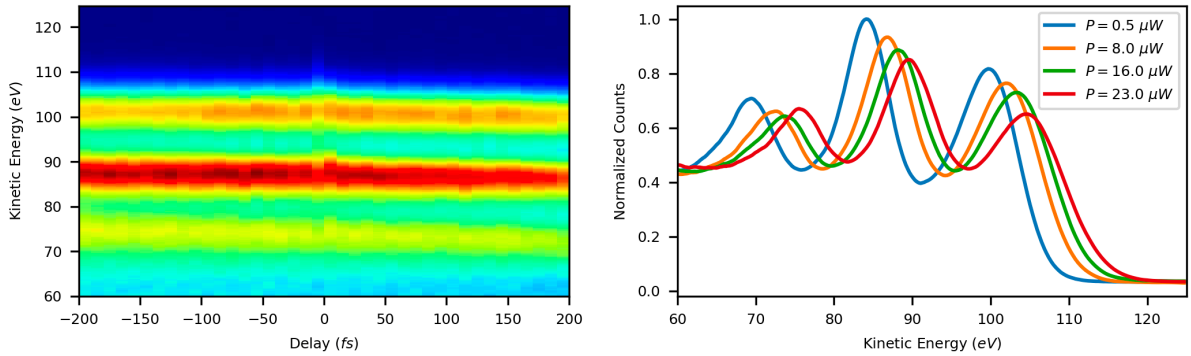

Figure 6.22: Space-charge behavior on a spectrogram recorded for GaSb(100) wafer (left). Intensity dependence of the space-charge effect as seen by recording spectra at set a delay value and varying the laser's power by opening and closing the iris before the pellicle (right). The power measuerments recorded here are estimations and relate only to each other as they are heavily dependent on the setup parameters.

place.

The optical damage implied that lower than usual intensities would be used leading to minimal gain in the expected signal with respect to the MgPc monolayer measurements since the total number of excited electrons had to be kept low to avoid the optical damage. By recording photoelectron spectra before and after photo-excitation, the persistence of the pump induced space-charge effect was realized. Documenting the pump induced space-charge effect as it was done for the MgPc monolayer can be seen in Figure 6.22. Beyond this effect no photo-excitation signal could be retrieved from the spectra as it was dwarfing any other changes to the photoelectron spectra.

The main conclusion that can be drawn is that, with the currently available instrumentation around the AS3 setup, no photo-excitation dynamics can be directly observed in the sense of valence band changes. The limiting factors are the pump induced space-charge effect and the self induced space-charge effect. Other considerations about the detector's resolution and sensitivity can also be considered, but they are not the leading causes. In order to avoid the pump induced space-charge effect, lower wavelength laser radiation has to be used as it will increase the nonlinear order of the above-threshold ionization (ATI) effect and severely limit it [93]. This can be achieved with the current setup by keeping the laser's pulse close to the fundamental during broadening or spectrally filtering it after HHG takes place. The major problem in doing so is that the signal can be lost due to poor spectral resolution. Improving the spectral resolution can only be achieved by reducing the XUV flux. Since the laser system is locked to 4 kHz due to the design of the amplification stage, an inevitable increase in integration

time would quickly render such attempts useless. The solution to this is a laser system with much less energy per pulse and much higher repetition rate leading to a low XUV flux that is accompanied by faster acquisition times. Systems like that are of no use to the attosecond streaking spectroscopy as they lack the peak intensities needed to generate that high harmonic radiation photon energies and generate isolated attosecond pulses with such narrow durations. It is then evident that such an experiment is best to have a dedicated setup along the lines of angle resolved photoemission spectroscopy (ARPES), where high repetition lasers are used in combination with hemispherical electron analyzers, although sacrificing the extremely low temporal resolution is inevitable. Another proven method that has gained traction in the last years is the attosecond transient absorption scheme [96, 97], where an attosecond technique is used to characterize the pulses which then propagate through a thin sample and into an XUV spectrometer setup where the absorption of the sample in the XUV range is recorded. This offers the extreme resolution of the attosecond streaking technique as well as a very good spectral resolution, as no electrons are used for the detection. The downside of this technique is that it requires a dedicated setup and it can only be implemented for specific thin samples that have absorbance resonances in the XUV spectral range, and that become more or less likely according to the population change on the valence and conduction bands. A setup in transient reflectance mode could also be constructed, but limitations on sample selection still apply, as the sample needs to be appropriately reflective in the XUV range and have resonances as described before.

Chapter 7

Attosecond Chronoscopy Studies on Highly Oriented Pyrolytic Graphite

Attosecond streaking spectroscopy is a useful tool for probing with uncanny temporal resolution into the nature of the photoionization process [12, 85, 98--100]. In the present work a focus on solid state photoemission is prominent, as it allows for probing the propagation of electrons in evermore complex materials, thus revealing more effects [99,101--103]. Solid state photoemission can be seen in two ways, the tree-step model [104,105], and the one-step model [102,106]. In the three-step model the solid state photoionization is split into three steps, namely photoionization, propagation within the solid to the surface, and escape through the surface. The one step model on the other hand treats the process as a single process, where the propagation within the material and the release through the surface are included in the calculation of the photoionization final state. More details about the two models can be found in the corresponding references.

As electrons are released within the bulk of a material from their parent atoms, they can acquire a phase. The released electron wave packet propagates through the material, it will experience further modification on its phase due to the material's potential surrounding it. If electrons originate from different states and their propagation path or parameters are different, they will end up having acquired different phases when exciting the material. This difference in phase can be translated into a delay between the different wave packets and can be encoded into an attosecond streaking trace, provided that the different wave packets acquire their phase differences before they encounter the streaking field. Measuring the relative delay between streaking of different photoionization peaks in a streaking measurement the phase shifts of the electron wave packets can be extracted, producing conclusions about their origin.

In this study, highly oriented pyrolytic graphite (HOPG) was used due to its layered structure. Photoelectrons that are generated into the bulk of the material would have to propagate

through the layered structure, which is a periodic potential. As they do so, they effectively travel through a Bragg reflector, which does not allow for specific frequencies to exist within it. As electrons are excited with energies for which their wave numbers match the periodicity of the layers, the propagation within the material should be forbidden and a delay should be present with respect to electrons that do not match this criterion. By recording the delay between electrons coming from two bands of HOPG as a function of the XUV photon energy, the effect of the periodic structure in the propagation of the electron wave packet can be recorded.

This project was a collaboration between the the group of Prof. Dr. Johannes Barth, E20 Chair for Surface and Interface Physics and the group of Prof. Dr Reinhard Kienberger, E11 Chair for Laser and X-ray Physics, TUM, and the group of Prof. Dr. Joachim Burgdörfer, Institute for Theoretical Physics, Vienna University of Technology. From the group of Prof. Dr Reinhard Kienberger, Maximilian Schnitzenbaumer, Pascal Scigalla, Michael Haimerl, Eckhard Schock and I were involved in the experimental procedures. Analysis of the data was performed by Maximilian Schnitzenbaumer. This work was originally submitted for publication in the journal Physical Review Letters. A more in-depth description of the project can be found in the thesis of Maximilian Schnitzenbaumer [107]

7.1 Highly Oriented Pyrolytic Graphite

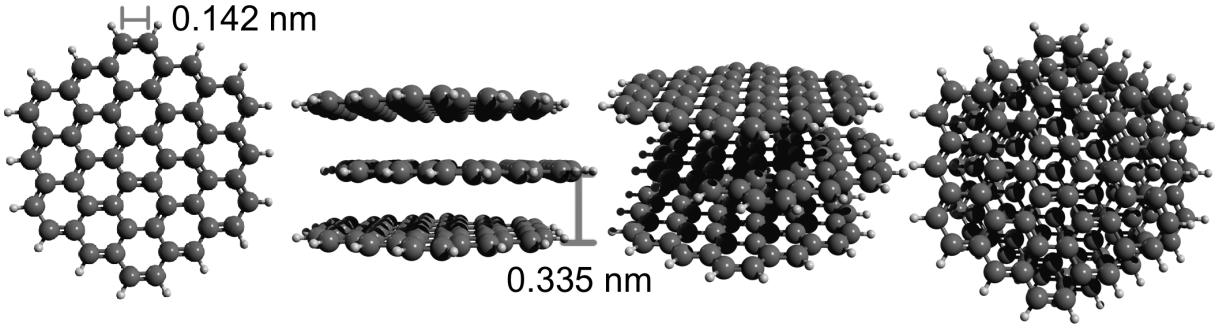

Figure 7.1: Structure of Graphite. A graphene sheet is demonstrated first, followed by three graphite layers from different perspectives. Hydrogen atoms have been added at the ends of the structure to terminate it.

When a carbon structure in sp^2 hybridism, where the carbon atoms form a 2-dimensional honeycomb lattice, is found alone, it called graphene [108]. Loosely bound by π-stacking consecutive equidistantly spaced (spacing of 0.335 nm) graphene layers form graphite. Near the surface of graphite the spacing is only slightly affected [109] and is not expected to have a major effect.

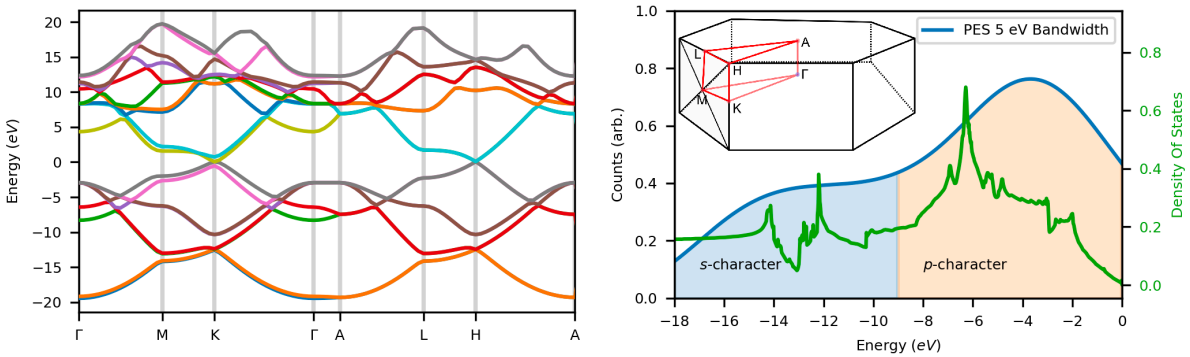

Figure 7.2: DFT calculations of Graphite. The Band structure of Graphite is presented on the left. The corresponding Density of states (green line) as well as a PES spectrum prediction for 5 eV bandwidth (blue line) are shown on the right. Zero on the energy axes of both plots denote the Fermi energy.

Each second layer is shifted with respect to the first so that only every second carbon atom has a direct neighbor on the next layer, as shown in Figure 7.1 [110--112]. Graphite is a semiconductor with wide spread uses and applications raging from high-temperature lubricants to brushes for electrical motors, to electronics and many more, due to its extraordinary properties. The layers are only loosely connected by the delocalized p_z electrons extending perpendicular to the layer. On the other hand, these delocalized electrons offer a very high electrical and thermal conductivity. This makes the graphite optically resonant across the complete visible and NIR spectrum.

A DFT calculation of the band structure of graphite can be seen in Figure 7.2. The origin of the bottom two states are the $2s$ states of carbon, while the next six bands located between the $2s$-bands and Fermi energy originate from the $2p$ orbitals. More detailed studies of HOPG valence band using XPS, X-ray emission spectroscopy (XES) and DFT calculations reveal a more complicated picture [113, 114], where the contributions are more intertwined. The main result still remains that, the tighter bound electrons in the valence band of HOPG are predominantly of s nature, while closer to the Fermi level, the p nature is dominant. From the DOS calculated from the DFT an estimate of the photoelectron spectrum can be obtained by convolving it with a Gaussian of appropriate bandwidth. By doing so, two peaks are formed, separated by approximately 10 eV. The two peaks are primarily of s- and p-character due to their origin. These peaks offer a convenient way of characterizing the relative delay between two photoelectrons propagating through the crystal at different kinetic energies and they will constitute the primary characterization tool used in this work.

The periodicity of HOPG is expected to cause band gaps in the ΓA direction, as electrons

with wavenumbers that match an integer multiple (n) of the lattice periodicity cannot propagate. The expected energies for those electrons can be calculated (in electronvolts) by the relation $E_n = n^2 \times 0.838\ eV$. Specialized DFT calculations for converging at high energies, predict a wide band gap in the region of 84 eV above the Fermi level, without crossing bands that span even to angles above 20° from the ΓA direction. Probing the photoemission delay for photon energies around 100 eV (taking into account the binding energy of the valence photoelectrons) should reveal the effects of the periodicity induced band gap on the photoionization process.

7.2 Attosecond Chronoscopy on HOPG

In this section the experimental procedures for preparing a clean surface of HOPG crystal will be described. The experimental results will be presented and interpreted in the basis of the most relevant theoretical framework. In the light of all of these we will discuss what this work adds to the understanding of solid state photoionization process.

7.2.1 Surface Preparation of HOPG

For the preparation, a commercially available HOPG crystal was used. The sample needed to be cleaved in vacuum to remove the top layers which are contaminated as they come in contact with the atmosphere. For this reason, a mask was used to hold the sample steadily onto the sample holder. One end of a capton adhesive tape was glued on the top face of the sample and the other end was glued in the inner wall of the load-lock chamber of AS3, ensuring that the orientation was such that when the sample was moved from the load-lock chamber into the UHV preparation chamber, the tape would peel from the surface of the sample, removing the top layers of graphite. Once the sample was moved into the preparation chamber with successful cleaving, it was further treated by heating to 1000 K where it remained for 5 minutes. After that, the sample was let to cool. The heating cycles were repeated five times. The surface quality was confirmed by XPS measurements and LEED characterizations as seen in the left plot of Figure 7.3. It can be seen there that the shape of the $1s$ peak of carbon changes and the $1s$ peak of oxygen completely disappeared with the heating treatment after cleaving. The LEED picture shows part of the concentric circles which is the expected LEED pattern for HOPG. The geometry of the LEED setup does not allow for the recording of the complete circles in the AS3 chamber.

To work toward the determination of the absolute photoemission time for graphite, a monolayer of iodoethane on the HOPG surface was also prepared by evaporating iodoethane on the HOPG surface with a background pressure of 1×10^{-9} mbar for approximately 30 s while keep-

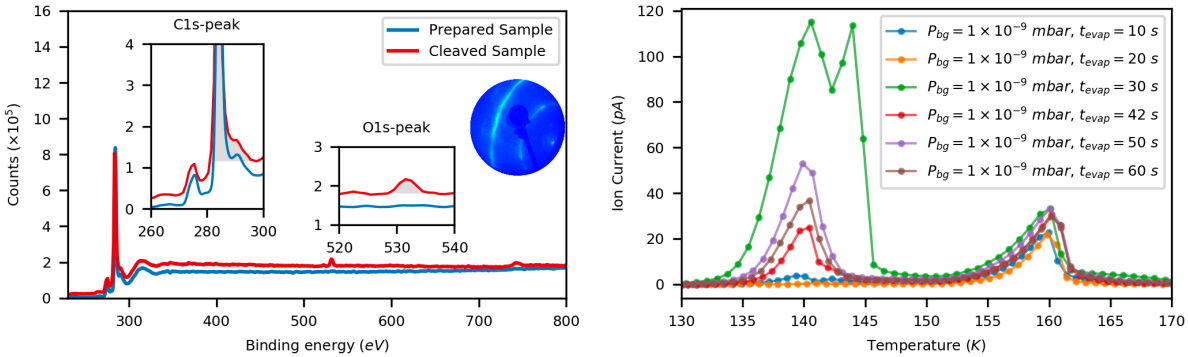

Figure 7.3: Sample characterization of HOPG layer by XPS in the left plot. The inlays show a close up of carbon 1s and oxygen 1s peaks and a LEED measurement. TPD measurements of iodoethane on HOPG surfcace for different deposition conditions. The background pressure and evaporation times are shown.

ing the temperature of the surface at 80 K. The sample was then heated to 150 K to desorb all the iodoethane that was not in direct contact with the HOPG surface, leaving a monolayer behind. The evaporation and temperatures were determined by TPD spectroscopy study, where the sample was prepared by using different parameters. The sample was then driven in front of a quadrupole mass spectrometer. The sample was then slowly heated at a rate of 0.5 K/s while the mass spectrometer records the current induced by ions of mass 156 Da, which is approximately the molecular weight of iodoethane (actual molecular mass 155.9656 Da). Such recordings are presented in the right plot of Figure 7.3 versus the temperature of the sample. We can observe two peaks. The first one is centered around 137 K and the other one is around 157 K. The first peak corresponds to molecules that are bound to each other while the second one corresponds to molecules that are bound to the HOPG surface.

7.2.2 Experimental Determination of the Effect of Photoelectron Kinetic Energy on the Photoemission Timing in HOPG

It is expected that the a resonance of the photoelectrons wavelength with the layer spacing would happen for photon energies of approximately 110 eV. The region of photon energies $80 - 130$ eV was systematically probed using pulses polarized 15° to the sample's normal and a detection angle of 0° (ΓA direction) and the delay between the two bands was determined. Figure 7.4 demonstrates the results of the measurements. The delays have been determined by the differential variant of the restricted TDSE method (see Appendix B). Each point in Figure 7.4 corresponds to an average value of a data set as it is shown in Figure 7.5. As it can be seen in the left plot of Figure 7.4, there is a characteristic valley in the measured delays.

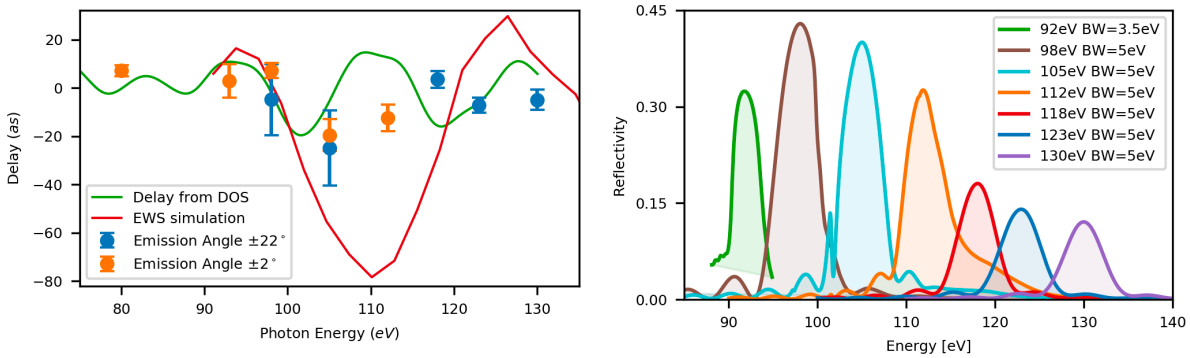

Figure 7.4: Relative delay values between the $s-$ and $p-$character bands of HOPG as determined by attosecond streaking chronoscopy (left). The convention used is that positive values of delay correspond to the $p-$band electrons being exposed first to the streaking field. Theoretical calculations of the expected delays with two different methods are overlaid (green and red lines). The reflectivity of all the inner mirrors used in the experiments (right).

Measurements that were made with the electrostatic lens of the TOF detector (emission angle $\pm 22°$) do not significantly differ from the ones recorded without the lens system (emission angle $\pm 2°$). A theoretical calculation of the delay values between the two bands of HOPG is overlaid with the data. It is clear that the experiment is in good agreement with the theory, especially in the case of DOS-deduced delays (see next section). The right plot of Figure 7.4 depicts the reflectivity of the inner mirrors used to record the data sets leading to the determination of the delay values.

Figure 7.5 is a collection of all data points as retrieved by the differential form of the restricted TDSE method (see Appendix B) directly from attosecond streaking spectrograms of HOPG for different photon energies. The left column is a collection of all data sets obtained without using the electrostatic lensing system of the TOF detector (emission angle $\pm 2°$), while the right column is a collection of data sets obtained by using the electrostatic lens (emission angle $\pm 22°$). For all data sets a minimum of 30 reliable data points was used. The data sets for 98 eV and 105 eV with lens were obtained to confirm that the value does not vary between the two acquisition methods and thus they are meant to be an addition to the initial data set. To determine the average delay value per photon energy a weighted average has been performed.

As a step towards the determination of the absolute photoemission timing of HOPG, a series of measurements was performed on a iodoethane monolayer on HOPG using an inner mirror reflecting at 105 eV and 5 eV bandwidth. This selection was made since the absolute photoemission time of iodine has been determined in the work of Ossiander et al. [115] in the same spectral range. The iodioethane was used since the photoionization cross section of iodine

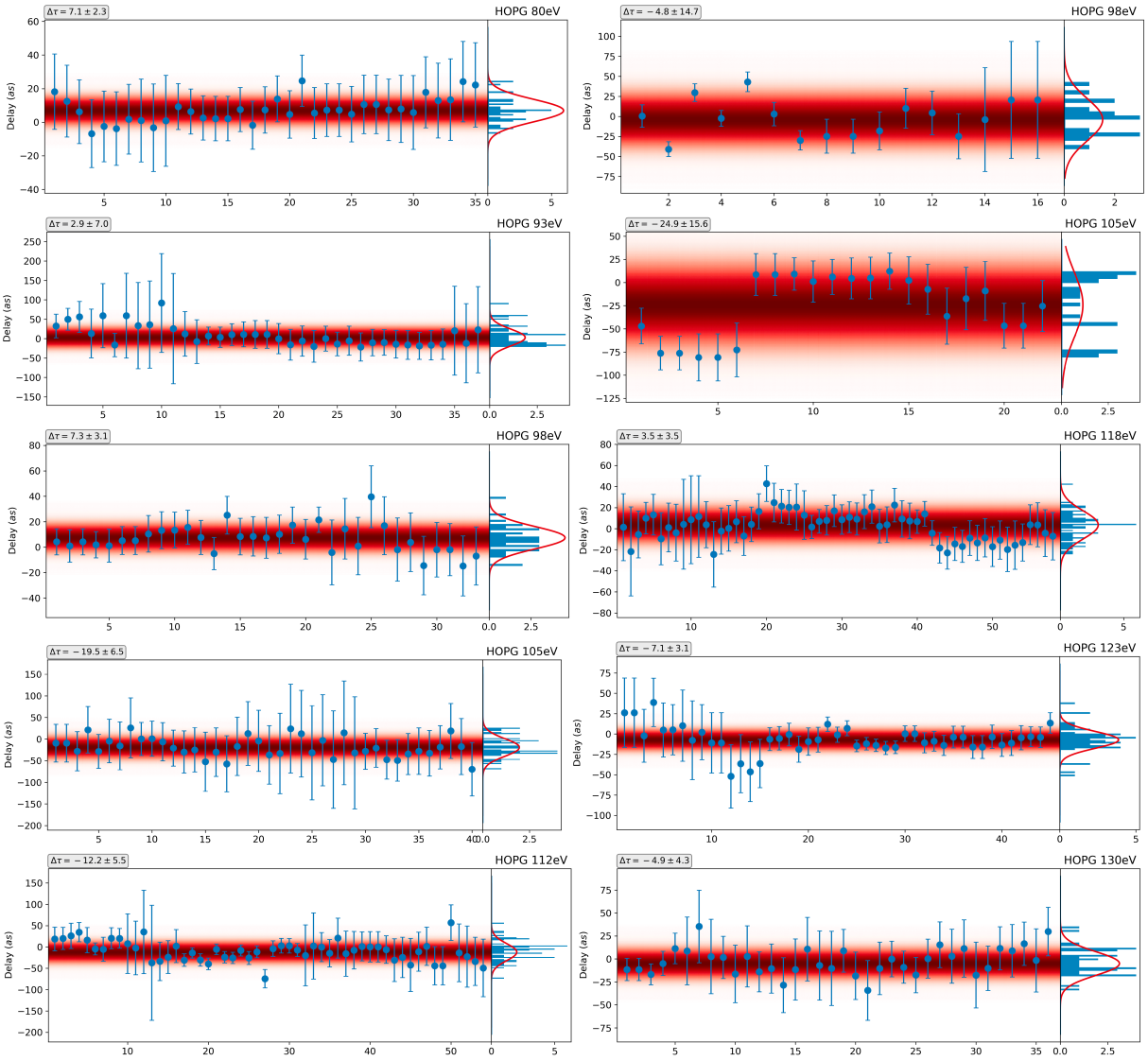

Figure 7.5: The data sets and their statistics for determining the delay values between the two bands of HOPG. The left column shows data sets obtained without using the electrostatic lens of the TOF, while the right column shows data obtained by using the electrostatic lens of the TOF.

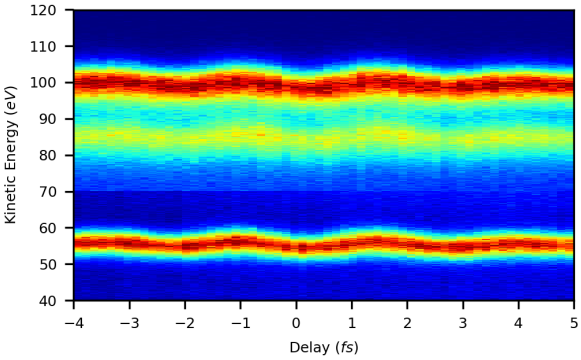

Figure 7.6: Typical streaking trace from iodethane monolayer on HOPG. The first two bands are the $p-$ and $s-$character bands of graphite, while the lowest peak corresponds to the iodine $4d$ photoionization peak.

$5d$ exhibits a significant resonance in the range of 75 eV, which makes the detection of iodine even in a monolayer fairly straight forward. On the other hand, iodoethane is an easy way to ensure the safety of the pumping systems and has a fairly high vapor pressure, which also makes the evaporation process simpler using dedicated evaporators for iodine. A typical attosecond streaking trace from iodoethane monolayer on HOPG can be seen in Figure 7.6. The upper two bands correspond to the $p-$ and $s-$bands of HOPG, while the lowest band corresponds to the iodine $4d$ band. As iodoethane was loosely bound to the HOPG surface, as demonstrated earlier by the TPD measurements, the intensity of the laser pulse had to be kept low in order to avoid locally heating the sample and disrobing the iodoethane. Still, the intensity of iodine $4d$ decreased slowly with time. This has been amended by separately normalizing the iodine $4d$ peak across the spectrogram and using a fresh spot for every new measurement ensuring the maximum achievable quality. The delay values between the HOPG photoemission peaks and the iodine $4d$ peak have been determined as $\Delta\tau_{p-I4d} = 42.5 \pm 11.6\ as$ and $\Delta\tau_{s-I4d} = 66.0 \pm 11.4\ as$. There can be effects that cannot be excluded in the photoemission process, such as the shielding of the laser pulse inside the HOPG and the effects of the iodoethane layer on the phase of the emitted photoelectrons from HOPG, therefore the absolute photoemission time cannot be deduced with certainty. If one is to assume complete shielding from the iodoethane monolayer and zero effect on the HOPG photoemission times from it, an absolute time of $\tau_p = 68.5 \pm 12.0\ as$ and $\tau_s = 92.0 \pm 11.8\ as$ can be estimated. It is also noteworthy that the delay value between the HOPG bands for the case of XUV photon energies of 105 eV is independent of the existence of the iodoethane monolayer, since both experiments with and without iodoethane gave the same values within the experimental error.

7.2.3 Interpretation of the Theory Behind the Photoionization Timing of HOPG

Two computation schemes for theoretically determining the dependence of the photoemission delay with the exciting XUV photon energy were utilized. The first scheme is based on the results of DFT calculations of bulk HOPG unit cell using the Vienna Ab initio Simulation Package (VASP). The DOS $\rho_\Omega(E)$ and dwell time of a wavepacket inside the corresponding region τ_d are connected by $\tau_d = 2\pi\hbar\rho_\Omega(E)$ [116]. On the other hand, the Eisenbud-Wiegner-Smith (EWS) delay τ_{EWS}, which is the delay accuired by a wavepacket from scattering by a potential (in our case the potential of the carbon atoms of HOPG), is related to the dwell time [116]. If we assume a single channel scattering resonance, then $\tau_d = \tau_{EWS}$ [85, 117--119]. By appropriately accounting for the symmetries of each orbital, the p and s character DOS are used to determine the delay of each wavepacket. The results are shown in Figure 7.4 (green line), where only the absolute delay value has been varied as an adjusting parameter. For the second computation method, the DFT calculated potential of HOPG has been averaged along two dimensions parallel to the surface, leaving a 1-dimensional representation of the potential. Although the resulting potential cannot represent the AB stacking that HOPG layers exhibit and results in more frequent band gaps, the behavior of τ_{EWS} near a band gap should not be qualitatively affected. The ground state of such a potential is excited into high-lying excited states by an approximate XUV pulse and the resulting wavepacket is let to propagate for a set time. The results for the p and s like orbitals are compared with a reference wavepacket propagating with the same final energy, but without experiencing the potential. Results are overlaid with the experimental findings in Figure 7.4 (red line).

As the incoming radiation from the laser has a polarization close to the surface normal, the field is expected to penetrate into the HOPG without significant screening [109, 120]. The measured delay is thus expected to be primarily the EWS delay, as the electrons can freely experience the streaking field as soon as they leave the parent ion and encrypt the acquired phase from only the first step of the three-step photoionization model into their momenta. In both simulation cases, only the EWS delay was determined and the results indicate an effect that resembles the measured delays, confirming the above statement. In conclusion the simulations confirm that the mere generation of the electron wavepacket close to the band gap has an effect on the photoionization delay, where the electron that has energies approaching the band gap is delayed, while the electron that is generated in proximity to but above the band gap seems to accelerate its generation.

Chapter 8

Conclusions And Outlook

The present work was aimed at investigating novel approaches to studying and understanding the dynamics of complex semiconductor materials relevant to technological applications. An understanding of light-matter interactions primarily from the perspective of quantum optics coupled with recent technological advances may give rise to opportunities to increase our understanding in evermore complex materials which in turn can yield new technological advances.

As a first step, the dynamics of MgPc single crystal thin film semiconductor, synthesized with a newly introduced preparation method called liquid deposition, were studied by means of pump-probe transient absorption techniques in the visible and mid-infrared spectral ranges. The measurements revealed in the mid-infrared spectral range indicated a clear signal of an almost one dimensional excitonic dissipation mechanism. The dynamics in the visible spectral range reveal the interband dynamics of the system with femtosecond precision, but is incapable of directly distinguishing the exact dimensionality of the excitonic mechanism. A thin MgPc film semiconductor with higher complexity structure (polycrystalline/amorphous) was manufactured using the spin coating method. The second sample under examination with mid-infrared transient-absorption revealed a clear dimensionality increase in the excitonic dissipation mechanism. Confirming the dimensionality change in the visible spectral range was achieved by decoupling the contributions from different structural configurations within the spin coated sample, and separately simulating each contribution with a quantum optical toy-model that describes the dynamics of a simplified MgPc bi-molecular system with different intermolecular coupling parameters. By doing so, a relatively simple method for calculating and describing the behavior of a complex system was introduced, capable of describing the femtosecond scale interband dynamics as well as the pico- to nanosecond excitonic dissipation of the residual energy in the MgPc semiconductor.

The next step was to push towards the attosecond timescale recording of light-matter in-

teractions. Two different approaches were considered in that front, namely investigating the bound-electron dynamics, much like the transient absorption studies, and photoionization dynamics, which could be investigated using the attosecond chronoscopy. Keeping firstly the perspective of bound-electron dynamics, a theoretical and experimental investigation was conducted on the expansion of the solid-state attosecond streaking spectroscopy setups towards a visible-pump XUV-probe scheme transient photoemission technique for detecting with attosecond precision the electron dynamics of technologically relevant semiconductor systems. A computational model for predicting the dynamics as well as the resulting signal from such an experiment was developed, as well as analysis approaches for retrieving the electron dynamics. The experimental efforts were focused on an MgPc monolayer on Ag(100) surface and on a GaSb semiconductor wafer. In both cases, despite the level of setup optimization, the signal was not retrievable due to parasitic effects intrinsic to the way of measuring. Since the attosecond streaking spectroscopy uses XUV attosecond pulses to extract photoelectrons and those photoelectrons are detected as the attosecond probe, space-charge effects are bound to significantly reduce the spectral resolution of the setup. Suppressing the space-charge effects would be possible in manners that either demand dedicated setups for the experiment to take place in, or that render the immediate technological relevance low, both of which were out of the scope of this work. Nevertheless, the results of this work provide significant insights into the nature of attosecond streaking spectroscopy, and provide tools, methods and considerations that can be of relevance to other photoionization studies.

Finally, from the perspective of photoionization dynamics, the photoemission times of HOPG, which is a layered semiconductor system, close to the material's bandgap (or otherwise for photoelectron wavepackets that have a wavenumber that is a multiple of the lattice periodicity) were studied utilizing an attosecond streaking spectroscopy setup. A distinct effect on the photoemission delay was observed when the exciting photon energy matches the material's bandgap. Two different theoretical approaches were used to confirm the origin and behavior of the observed attenuation of the photoionization delay, deducing it from the band structure of the material and by propagating a wavepacket from a reduced one-dimensional potential. Both methods only considered the EWS contributions to the photoionization delay and show qualitatively similar behavior to the experiment, confirming the assumptions of the effect being an EWS photoionization delay. Attempts were made towards the determination of absolute photoionization time from the HOPG surface by repeating some photoemission delay measurements on HOPG with an added monolayer of iodoethane. The photoionization delay difference determined for the $s-$ and $p-$bands of HOPG with respect to the iodine $4d$ peak were determined to be $\Delta\tau_{s-I4d} = 66.0 \pm 11.4\ as$ and $\Delta\tau_{p-I4d} = 42.5 \pm 11.6\ as$ respectively for an XUV photon energy of 105 eV. Since the HOPG partially shields the NIR pulse at its surface, the determina-

tion of the absolute photoemission time cannot be safely interpreted from these measurements, until an accurate determination of the shielding effects is deduced. This study revealed that the photoionization process seems to be delayed when the energy of the emitted photoelectron approaches a bandgap. It provides a clear, experimentally confirmed and theoretically supported insight into the nature of the photoionization process.

In conclusion, in this work, several aspects of light-matter interactions were used as tools to study technologically relevant complex semiconductor systems, expand the tools available for characterizations of more complex systems and push the limits of the available techniques and setups, as well as investigate the nature of light-matter interactions such as the photoionization process.

The need for technological advancement is an everlasting one that drives research and investigation for new materials, new experimental, theoretical and analysis techniques and implementations. To this end, this work only paved the way for a number of studies by presenting a methodology and some analytic approaches for studying complex semiconductor systems. It provided definitive answers to the capability of the attosecond streaking spectroscopy as a pump-probe technique for bound-electron dynamics, which in turn reveals the steps that must be taken for such measurements to take place with attosecond resolution. It also motivates further studies on the nature of photoionization process, as it leaves an open question on the ambiguity of determining the absolute photoemission timing of HOPG and similar materials where the streaking field penetrates the surface.

Appendices

Appendix A

Space-Charge Effects

In this work concerning the parts of utilizing the attosecond streaking spectroscopy for recording the valence band dynamics, the main obstacle encountered was space-charge effects that severely limit primarily the spectral resolution of the experimental setups. In this appendix the concepts behind the space-charge effects will be briefly introduced.

A.1 Self Induced Space-Charge Effect

The first consideration is the self induced space-charge effect, which occurs when there are dense concentrations of electrons localized in space. As the electrons propagate in space in a cloud-like formation, the outer shells of the cloud are pushed away from the main cloud, causing the fastest electrons of the bunch to gain more energy, while the slowest ones end up loosing even more energy. This causes an inevitable broadening in the measured spectrum of the electron cloud. A shift in the central energy of the electron can also occur. The electron clouds are generated usually by some pulse, typically in the visible spectral range and above, all the way to X-rays. A significant difference in the behavior of space-charge effect can be seen if one compares the effect in femtosecond or picosecond generated photoelectrons [121, 122]. This effect is caused by the longitudinal to transversal ratio difference between the two electron clouds, which results in different dynamics taking place.

A complete analytical description of such an effect is inherently impossible to happen, as it is a many-body problem, the details of which seem to affect the outcome in significant ways. What is possible and relatively accurate is a many-body simulation of the phenomenon, as it was done by Hellmann et al. [123], who made a lot of relations apparent. As an example, for short pulses like the ones used throughout this work, the generated cloud is an almost 2-dimensional disk as $c\tau \ll r_0$, where τ is the pulse duration c the speed of light and r_0 the radius of the spot.

This makes the pulse duration practically irrelevant for the effect, while the most important parameter for the geometric definition of the electron cloud is the spot size. The spectral distribution of the photoelectron cloud also seems important as, for spectrally broad chirped pulses, the effects seem to be more pronounced on the higher energy side of the spectrum, while the ability of the sample to form mirror charges on its surface will greatly counteract the effects of self induced space-charge. Another finding, which was also in experimentally observed was that the momentum resolution is not significantly affected by the space charge effects [123, 124]

A.2 Pump Induced Space-Charge Effect

In our experiments there are two pulses present (XUV and NIR) both capable of generating a cloud of photoelectrons, each with its own properties. The effect that one electron cloud has on the other can be significant. The NIR pulse generates a great number of slow photoelectrons mainly by nonlinear effects resulting in ATI, while the XUV pulse generates fewer photoelectrons with much greater kinetic energies from one photon photoionization, due to the higher photon energies. As the delay between the two pulses is adjusted, the situation between the electron clouds changes. When the XUV arrives at the sample first, it is always repelled towards the detector increasing its average photoelectron energies, with the maximum push between the pulses occurring when the pulses overlap temporally. When the XUV pulse arrives after the NIR pulse, the XUV photoelectrons have to overcome the attraction of the mirror charges and the repulsion of the NIR generated photoelectron cloud before they can overtake the latter. This means that they are going to lose some of their energy and, once they overtake the NIR generated cloud they will be accelerated again, resulting in a much reduced energy gain or even energy loss in specific cases. The effect is expressed in our recordings as an asymmetric delay dependent shift of the complete XUV photoelectron spectrum.

It was demonstrated that, for the case of the pump induced space-charge effect, a mean field model can be sufficient to describe the effect to a good extent [125]. In later iterations the effects of mirror charges were added [126] and a full study of the effect was performed by Oloff et al. [93] showing the deterministic nature of the phenomenon and a significant absence of contribution from stochastic effects such as electron scattering. An important finding for our case is the dependence of the effect on the photon energy of the pump pulse, where it was shown that it greatly depends on the number of photons needed to release a photoelectron. Thus, it was shown that doubling the photon energy (from 1.58 eV to 3.16 eV), the same shift could be achieved with an order of magnitude less energy per pulse.

A.3 Observables in the AS3 Setup

Both instances of space-charge effects have been observed in the AS3 beamline. Characterizing the details of the space-charge effects was never the primary objective during this work, thus significant measurements are lacking that would help determine the exact parameters around it. As this was the main limiting factor in the experiments, it is only reasonable to present some findings and considerations about it and the effects it had in the measurements.

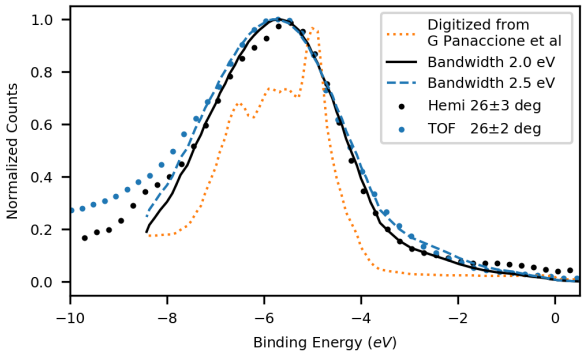

Figure A.1: Estimations of the spectral resolution of the setup based on photoemission spectra of Ag(100). Data from the work of Panaccione et al. [127] were used as a reference (dashed orange line). Convolutions of the reference data with Gaussians of bandwidth (FWHM) of 2 eV (black solid line) and 2.5 eV (blue dashed line) are shown. Photoemission data recorded at an emission angle of 26° using the Hemispherical analyzer (black dots) and the TOF spectrometer (blue dots).

The resolution of the setup can be estimated by comparing our results for the photoemission of Ag(100) with data from literature. For that reason, data from the work of Panaccione et al. [127] were used. The data were convolved with Gaussians of known bandwidths (FWHM). The value was varied until a decent overlap with the data recorded in our setup was established. For the referenced work, a value for the spectral resolution (ΔE_{Ref}) is defined as 100 meV. Thus the nominal spectral resolution for the convolution of the reference data with Gaussians of bandwidth ΔE_G will be:

$$\Delta E_C = \sqrt{\Delta E_{Ref}^2 + \Delta E_G^2} \tag{A.1}$$

Since the resolution of the reference is so small compared with the Gaussians, the result is approximately the bandwidth of the Gaussians. For our setup we can write for the spectral resolution:

$$\Delta E_{AS3} = \sqrt{\Delta E_{Det}^2 + \Delta E_{XUV}^2 + \Delta E_{SC}^2} \tag{A.2}$$

where ΔE_{Det} is the resolution of the detector, ΔE_{XUV} is the bandwidth of the XUV pulse, which is defined by the reflectivity of the used mirror, and ΔE_{SC} is the bandwidth increase of the electron spectrum due to space-charge effects. The data presented here from the AS3 beam line were recorded using an inner mirror reflecting at 99.5 eV with a bandwidth of 0.8 eV. For the TOF detector we can deduce the resolution ΔE_{TOF} for the given energy range to be 0.23 eV [84]. For the hemispherical analyzer (SPECS Phoibos 100), by following the equations in the manual supplied by the manufacturer, we can deduce a spectral resolution of 0.18 eV for the parameters used to record the spectrum (Slit in position 1, pass energy 5 eV and detection angle of $\pm 3°$). A value of 2.36 eV can be calculated for the measurements with the TOF spectrometer and a value of 1.82 eV can be calculated for the measurements using the hemispherical analyzer.

Since the measurements were performed under the same conditions, the values would be expected to match for the two measurements. It is clear that the resolution for the measurements with the TOF spectrometer is worse, although the instrument resolution alone does not account for this discrepancy. The reality is that the TOF spectrometer has a working distance of 2 mm from its entrance. The fact that the TOF spectrometer had to be aligned at 26° from the sample's normal means that the sample had to be placed further away from the entrance of the TOF spectrometer due to geometrical restrictions. On the other hand, the hemispherical analyzer has a much greater working distance of 40 mm, which allows for the recording of the photoemission at different angles without the loss of resolution. The value of the spectral resolution loss from the space-charge effect can be used as it was calculated for the case of the hemispherical detector and can be applied to the equation for the TOF to calculate the effective loss of resolution due to the misalignment. By doing so, we obtain $\Delta E_{TOF} = 1.52\ eV$, which can be further split into the electronic resolution as it was given before and the misalignment resolution loss, for which we get an approximate value of 1.50 eV.

The second instance of space-charge effects is the pump induced space-charge effects. This adds to the spectral resolution loss by introducing delay dependent shifts and distortions in the spectra. A typical case of pump induced space-charge effect on graphene monolayer on SiO_2 surface can be seen in Figure A.2. A simple mean field model [93] was used to simulate the space-charge effect. As the pump induced space-charge effect is typically expressed within picosecond timescales [93,122,124] our data only include a small portion of the complete dynamics. On top of that, factors like the ellipticity of the spot due to the geometry have to be considered. Unfortunately, for an elliptic spot, an analytic expression cannot be acquired for the electric

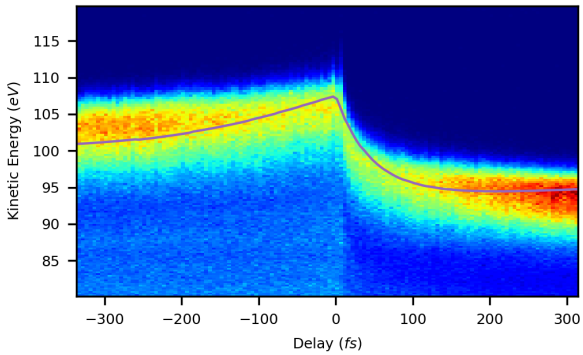

Figure A.2: Pump induced space-charge effect on the photoionization spectrum of monolayer graphene on SiO_2. A simulation of the effect is shown as a black line on top.

field and the simulation of the effect becomes very resource consuming. The reasons mentioned above, as well as not knowing the exact parameters of the electron cloud generated makes the simulations in our case hard to match with the experiments, thus it is not wise to attempt to draw conclusions from the exact values used in the simulations. It has also been shown that part of the resolution loss from the space-charge effect especially the energy shift and the restoration of the positions in k-space, can be restored [128], but the resolution in such a vanishingly small signal as is in our cases would not be returned, as the method is able to correct for the major peaks and shapes, not the fine details on those peaks.

Appendix B

Retrieval Methods

In the present work a number of analysis methods for retrieving the parameters of pulses from attosecond streaking spectrograms were implemented and considered as candidates for various non trivial applications. All methods used during this work can be implemented for retrieving the pulses as well as relative photoemission delays from spectrograms with multiple photoionization peaks. Extending the basic algorithms into retrieving photoemission delays was not the primary subject of this work and a description of implementing this can be found elsewhere [83, 84]. A brief description of the main methods will be given here to ensure comprehension of the basics behind the operation of each method, as well as the the advantages disadvantages and limitations imposed by each technique.

B.1 Center of Energy

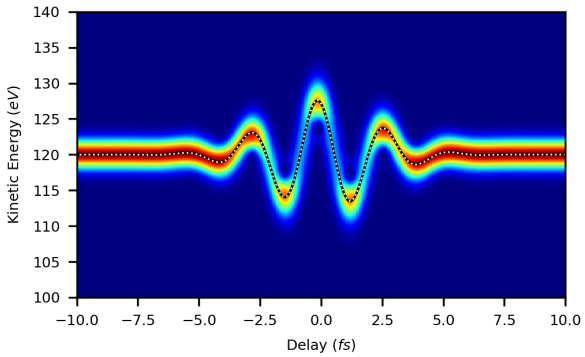

Figure B.1: Simulated streaking spectrogram. The center of energy has been drawn on top as a black solid line. The result of the least square fit has been overlaid as a dashed white line

The simplest and perhaps the most used method is the COE fit, according to which, the center of energy is traced throughout the delay axis. Assuming that the pulse envelope is not far off from a Gaussian, the equation for a gaussian pulse can be fitted to the center of energy and with a least squares minimization method the parameters of the near infrared can be estimated.

In Figure B.1, a simulation of an attosecond streaking spectrogram is shown. The results of the COE and the corresponding least squares fit are overlaid as a black solid line and a white dashed line respectively, allowing for a very fast and accurate determination of the properties of the dressing field and the binding energy, as the average of the central energy has to be equal to the photon energy minus the binding energy. If a background subtraction has been performed in the photoemission peak, a fitting of a sum of Gaussians can also be performed for determining the center of energy.

Most practical applications of COE fits are not to accurately retrieve photoemission delays nor characterizing the streaking field, but rather to provide accurate initial conditions for more sophisticated algorithms as the ones described below, also meant to retrieve the XUV pulse.

B.2 Restricted Time-Dependent Schrödinger's Equation.

The first significant method for retrieving accurately the properties of the XUV attosecond pulse is based on Equation 5.12, which is a solution to the TDSE and describes the attosecond streaking spectrogram with respect to the two pulses used to generate the spectrogram. By assuming again that the pulses are accurately described by the equation for pulses with Gaussian envelopes, and by replacing them to the equation, a minimization algorithm can be constructed [81,82]. Such an algorithm, given good initial conditions as described before and a streaking spectrogram which is focused around the pulse overlap region and with decent streaking amplitude, can easily retrieve the properties of both pulses. An example of this method can be seen in Figure B.2. A simulation of an attosecond streaking spectrogram is shown on top, followed by the results of the minimization algorithm. Lastly, a difference between the two is shown. The two spectrograms are in essence identical, which guarantees a good estimation of the parameters retrieved for both pulses.

Further improvements can be made to the algorithm to improve its accuracy [83,84,129]. For instance, a set of Gaussians can be used to fit the steady state spectrum of the photoionization peak. Then, the algorithm can be constructed to generate a streaking trace for every Gaussian and compare the sum of all traces to the given spectrogram. This minimizes the errors caused by a mismatch of the spectrum and allows the minimization routine to better track the streaking trace. A variance for reducing the effect of the background noise can be constructed by making the algorithm minimize the difference between the first derivatives along the delay axis of the

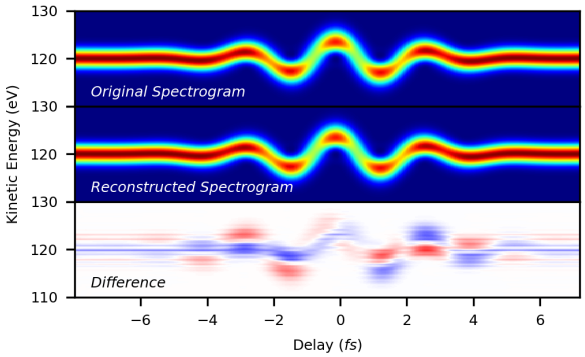

Figure B.2: Simulated streaking spectrogram (top), the reconstruction of it by the restricted TDSE method (midle) as well as the difference between the two spectrograms (bottom).

spectrogram and the reconstruction. The latter method was used to retrieve the photoionization delays from the attosecond streaking measurements of HOPG described in Chapter 7.

B.3 Least Squares Generalized Projection Algorithm

Another family of retrieval methods are based on the principles of FROG methodology [130, 131]. The similarity of Equation 5.12 with the equation for a FROG spectrogram allows for an implementation of the techniques developed for retrieving the spectrum and the phase of both the XUV and NIR pulses [77]. The FROG spectrogram is expressed as:

$$S(\omega,\tau) = \left| \int_{-\infty}^{\infty} P(t)G(t+\tau)e^{i\omega t}dt \right|^2 \tag{B.1}$$

where P represents the pulse to be characterized, while G represents a gating function that modulates the spectrum of P. By comparing with Equation 5.12, it becomes clear that P corresponds to the XUV pulse, while G corresponds to the Volkov phase terms that include the effects of the laser field. A method called LSGPA [78] is one of the best FROG type retrieval algorithms, as it is effective and robust. Furthermore, in this implementation, G is not necessarily only a phase filter; instead its amplitude is allowed to be different than unity, allowing it to act as an amplitude filter. This gives the algorithm the unique flexibility of incorporating intensity fluctuations into the gate function, allowing the accurate retrieval of the XUV pulse even in data where a degree of laser or sample instabilities have taken place. Figure B.3 shows the results of a pulse retrieval using the LSGPA method. The algorithm within 100 iterations was able to provide an accurate reconstruction of the spectrogram by retrieving the pulse and

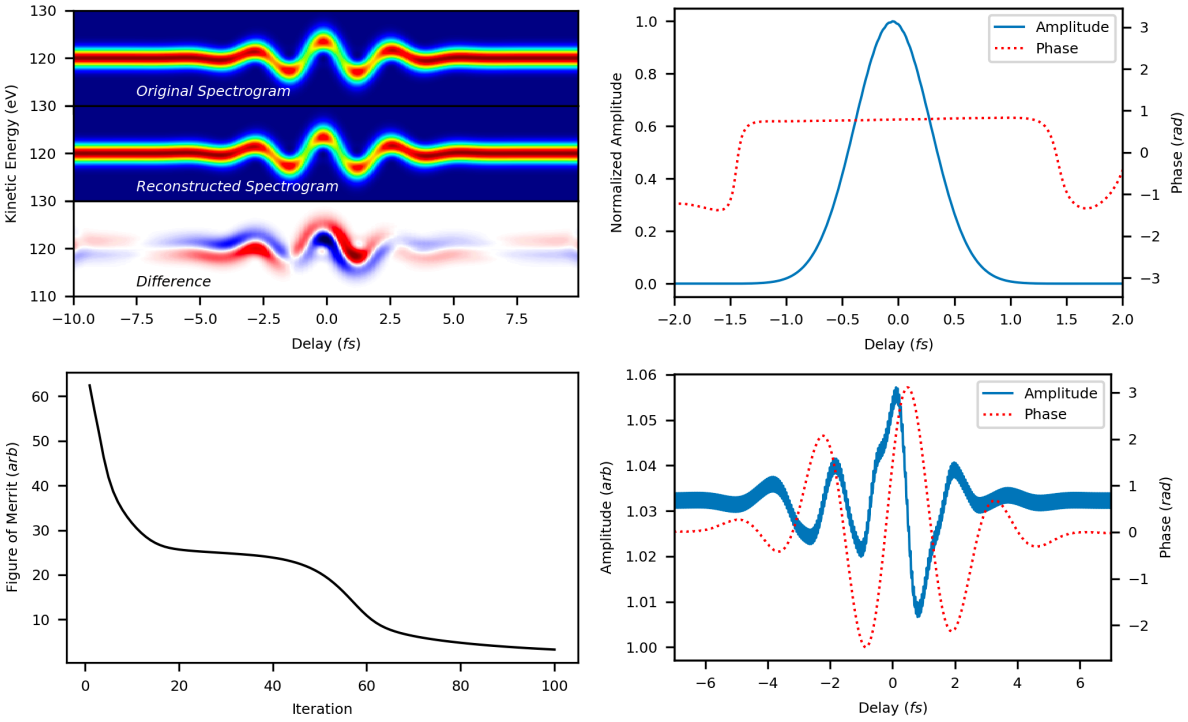

Figure B.3: LSGPA retrieval of simulated streaking spectrogram. The original spectrogram, reconstruction and difference (top left plot), a figure of merit versus the iteration number (botom left plot), the reconstructed pulse P (top right plot) and gate (bottom right plot) functions are shown

gate functions. The phase of the gate function can be compared with the Volkov phase term of Equation 5.12 and from that the vector potential of the laser pulse can be extracted as seen in Figure B.4. One of the downsides of the method is that the reconstructed gate function tends to oscillate and given noisy data and inefficient sampling, the oscillations can cause the algorithm to fail. In this case, a filter can be applied to the gate function to reduce the high frequency noise and help the algorithm converge. A loss of amplitude and sharp features in the reconstructed spectrogram can occur as a side-effect of filtering.

The advantage of FROG type techniques versus the restricted TDSE method is that the former can retrieve pulse and gate functions with arbitrary shapes. The pulses do not have to be well shaped nor well formed to be described by a fixed equation, which is optimum for pulse characterization. At the same time, this can be a negative feature for specific cases as any irregularity in the spectrogram that can be caused by mechanisms other than the pulses themselves will be incorporated in the gate and pulse functions, thus the reconstructed spectrogram would

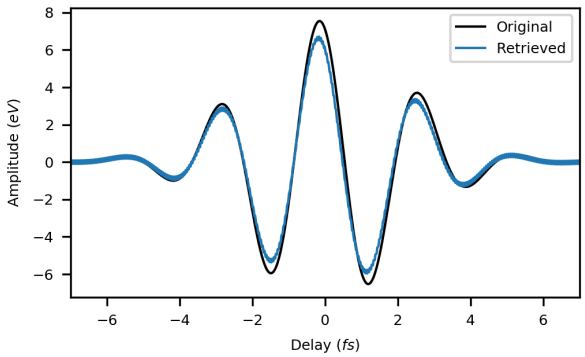

Figure B.4: Retrieved vector potential of the laser pulse from the reconstructed gate function (blue line), compared with the COE (black line).

exhibit the irregularities as well.

B.4 Ptychographic Iterative Engine

In conjunction with LSGPA, which is based on physical arguments on the overlap of the two pulses, another FROG type algorithm that is based on mathematical criteria for the determination of the gate and pulse functions called ptychographic iterative engine (PIE) can be constructed [79, 80, 132]. The algorithm differs only slightly from the LSGPA in that it generates new pulse and gate functions and is optimized on performance. In practice, the algorithm makes an iteration much faster than LSGPA, but progresses much less per step with respect to LSGPA. Nevertheless, it results in a net decrease of the computation time for retrieving the pulse and gate functions. It is also limited in the sense that the gate function has to be a phase filter only. An advantage with respect to LSGPA is the extra stability as the gate function does not suffer from oscillations that could destabilize the retrieval process, leading to meaningless results.

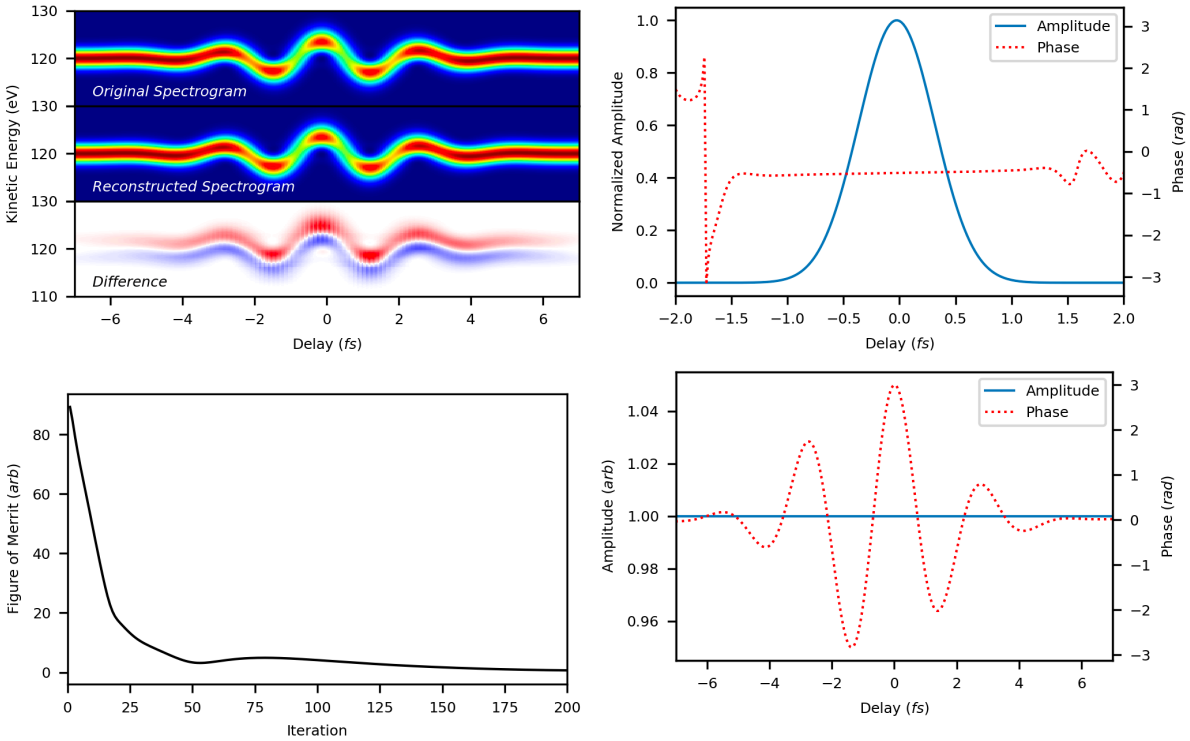

Figure B.5: PIE retrieval of simulated streaking spectrogram. The original spectrogram, reconstruction and difference (top left plot), a figure of merit versus the iteration number (botom left plot), the reconstructed pulse P (top right plot) and gate (bottom right plot) functions are shown

An example pulse retrieval using the PIE method can be seen in Figure B.5. The algorithm needed about 200 iterations to complete and result in an accurate reconstructed spectrogram and the retrieval of the pulse and gate functions.

Bibliography

[1] D. J. Griffiths, *Introduction to Electrodynamics*. Cambridge University Press, 6 2017.

[2] B. E. A. Saleh and M. C. Teich, *Fundamentals of Photonics*. Wiley, 2 ed., 2007.

[3] H. J. Pain, *The Physics of Vibrations and Waves: Sixth Edition*. John Wiley and Sons, 6 2005.

[4] M. Young, *Optics and Lasers*, vol. 5. Springer Berlin Heidelberg, 1984.

[5] F. J. McClung and R. W. Hellwarth, ``Giant optical pulsations from ruby,'' *Journal of Applied Physics*, vol. 33, pp. 828--829, 6 1962.

[6] M. A. Kovacs, G. W. Flynn, and A. Javan, ``Q switching of molecular laser transitions,'' *Applied Physics Letters*, vol. 8, pp. 62--63, 11 1966.

[7] W. E. Lamb, ``Theory of an optical maser,'' *Physical Review*, vol. 134, p. A1429, 6 1964.

[8] L. E. Hargrove, R. L. Fork, and M. A. Pollack, ``Locking of hene laser modes induced by synchronous intracavity modulation,'' *Applied Physics Letters*, vol. 5, pp. 4--5, 11 1964.

[9] A. Wirth, M. T. Hassan, I. GrguraÅ¡, J. Gagnon, A. Moulet, T. T. Luu, S. Pabst, R. Santra, Z. A. Alahmed, A. M. Azzeer, V. S. Yakovlev, V. Pervak, F. Krausz, and E. Goulielmakis, ``Synthesized light transients,'' *Science*, vol. 334, pp. 195--200, 10 2011.

[10] M. Lewenstein, P. Balcou, M. Y. Ivanov, A. L'Huillier, and P. B. Corkum, ``Theory of high-harmonic generation by low-frequency laser fields,'' *Physical Review A*, vol. 49, pp. 2117--2132, 1994.

[11] L. V. Keldysh, ``Ionization in the field of a strong electromagnetic wave,'' 1965.

[12] R. Kienberger, E. Goulielmakis, M. Uiberacker, A. Baltuska, V. Yakovlev, F. Bammer, A. Scrinzi, T. Westerwalbesioh, U. Kleineberg, U. Heinzmann, M. Drescher, and F. Krausz, ``Atomic transient recorder,'' *Nature*, vol. 427, pp. 817--821, 2004.

[13] R. Kienberger, M. Hentschel, C. Spielmann, G. A. Reider, N. Milosevic, U. Heinzmann, M. Drescher, and F. Krausz, ``Sub-femtosecond x-ray pulse generation and measurement,'' *Applied Physics B: Lasers and Optics*, vol. 74, pp. s3--s9, 2002.

[14] M. Hentschel, R. Kienberger, C. Spielmann, G. A. Reider, N. Milosevic, T. Brabec, P. Corkum, U. Heinzmann, M. Drescher, and F. Krausz, ``Attosecond metrology,'' *Nature*, vol. 414, pp. 509--513, 2001.

[15] G. Sansone, E. Benedetti, F. Calegari, C. Vozzi, L. Avaldi, R. Flammini, L. Poletto, P. Villoresi, C. Altucci, R. Velotta, S. Stagira, S. D. Silvestri, and M. Nisoli, ``Isolated single-cycle attosecond pulses,'' *Science*, vol. 314, pp. 443--446, 10 2006.

[16] R. Boge, S. Heuser, M. Sabbar, M. Lucchini, L. Gallmann, C. Cirelli, and U. Keller, ``Revealing the time-dependent polarization of ultrashort pulses with sub-cycle resolution,'' *Optics Express*, vol. 22, p. 26967, 2014.

[17] H. Mashiko, S. Gilbertson, C. Li, S. D. Khan, M. M. Shakya, E. Moon, and Z. Chang, ``Double optical gating of high-order harmonic generation with carrier-envelope phase stabilized lasers,'' *Physical Review Letters*, vol. 100, p. 103906, 2008.

[18] M. C. Chen, C. Mancuso, C. Hernádez-García, F. Dollar, B. Galloway, D. Popmintchev, P.-C. Huang, B. Walker, L. Plaja, A. A. Jaroń-Becker, A. Becker, M. M. Murnane, H. C. Kapteyn, and T. Popmintchev, ``Generation of bright isolated attosecond soft x-ray pulses driven by multicycle midinfrared lasers,'' *Proceedings of the National Academy of Sciences of the United States of America*, vol. 111, pp. E2361--E2367, 2014.

[19] M. Nisoli, S. D. Silvestri, and O. Svelto, ``Generation of high energy 10 fs pulses by a new pulse compression technique,'' *Applied Physics Letters*, vol. 68, pp. 2793--2795, 1996.

[20] P. Meystre and M. Sargent, *Elements of quantum optics*. Springer Berlin Heidelberg, 2007.

[21] M. O. Scully and M. S. Zubairy, *Quantum Optics*. Cambridge University Press, 9 1997.

[22] R. Boyd, *Nonlinear Optics*. Academic Press, 2008.

[23] P. Lambropoulos and D. Petrosyan, *Fundamentals of quantum optics and quantum information*. Springer Berlin Heidelberg, 2007.

[24] S. Trachanas, *Quantum Mechanics II*. University Publiching of Crete, 2008.

[25] A. Yariv, *Quantum Electronics*. Wiley, 3 ed., 1989.

[26] M. Kira and S. W. Koch, *Semiconductor quantum optics*, vol. 9780521875097. Cambridge University Press, 1 2011.

[27] H. Haug and S. W. Koch, *Quantum theory of the optical and electronic properties of semiconductors, fifth edition*. World Scientific Publishing Co., 5 ed., 2009.

[28] M. Uiberacker, T. Uphues, M. Schultze, A. J. Verhoef, V. Yakovlev, M. F. Kling, J. Rauschenberger, N. M. Kabachnik, H. Schröder, M. Lezius, K. L. Kompa, H. G. Muller, M. J. Vrakking, S. Hendel, U. Kleineberg, U. Heinzmann, M. Drescher, and F. Krausz, ``Attosecond real-time observation of electron tunnelling in atoms,'' *Nature*, vol. 446, pp. 627--632, 4 2007.

[29] K. Hütten, M. Mittermair, S. O. Stock, R. Beerwerth, V. Shirvanyan, J. Riemensberger, A. Duensing, R. Heider, M. S. Wagner, A. Guggenmos, S. Fritzsche, N. M. Kabachnik, R. Kienberger, and B. Bernhardt, ``Ultrafast quantum control of ionization dynamics in krypton,'' *Nature Communications*, vol. 9, pp. 1--5, 12 2018.

[30] K. S. Karimov, I. Qazi, T. A. Khan, P. H. Draper, F. A. Khalid, and M. Mahroof--Tahir, ``Humidity and illumination organic semiconductor copper phthalocyanine sensor for environmental monitoring,'' *Environmental Monitoring and Assessment*, vol. 141, pp. 323--328, 6 2008.

[31] S. S. Hassan, A. H. Kamel, and N. H. Elbehery, ``Potentiometric detection of low-levels of sulfamethazine in milk and pharmaceutical formulations using novel plastic membrane sensors,'' *Journal of Electrochemical Science and Engineering*, vol. 9, pp. 17--26, 2019.

[32] N. T. Boileau, R. Cranston, B. Mirka, O. A. Melville, and B. H. Lessard, ``Metal phthalocyanine organic thin-film transistors: Changes in electrical performance and stability in response to temperature and environment,'' *RSC Advances*, vol. 9, pp. 21478--21485, 2019.

[33] A. K. Ghosh, D. L. Morel, T. Feng, R. F. Shaw, and C. A. Rowe, ``Photovoltaic and rectification properties of al/mg phthalocyanine/ag schottky-barrier cells,'' *Journal of Applied Physics*, vol. 45, pp. 230--236, 1974.

[34] T. Duong, J. Peng, D. Walter, J. Xiang, H. Shen, D. Chugh, M. Lockrey, D. Zhong, J. Li, K. Weber, T. P. White, and K. R. Catchpole, ``Perovskite solar cells employing copper phthalocyanine hole-transport material with an efficiency over 20

[35] J. Blochwitz, M. Pfeiffer, T. Fritz, and K. Leo, ``Low voltage organic light emitting diodes featuring doped phthalocyanine as hole transport material,'' 8 1998.

[36] M. J. Cook, ``Phthalocyanine thin flms*,'' 1999.

[37] S. K. Hämäläinen, M. Stepanova, R. Drost, P. Liljeroth, J. Lahtinen, and J. Sainio, ``Self--assembly of cobalt-phthalocyanine molecules on epitaxial graphene on ir(111),'' *Journal of Physical Chemistry C*, vol. 116, pp. 20433--20437, 2012.

[38] T. Komino, M. Matsuda, and H. Tajima, ``The fabrication method of unsubstituted planar phthalocyanine thin films by a spin-coating technique,'' *Thin Solid Films*, vol. 518, pp. 688--691, 11 2009.

[39] B. Wang, X. Zuo, Y. Wu, Z. Chen, and Z. Li, ``Preparation, characterization and gas sensing properties of high soluble metal (ii) phthalocyanine thin films by spin-coating method,'' *Materials Letters*, vol. 59, pp. 3073--3077, 10 2005.

[40] S. Jain, R. Ridhi, N. Soleimanioun, S. Bharti, G. K. Bhullar, and S. K. Tripathi, ``Layers dependent properties of magnesium phthalocyanine thin films prepared by langmuir blodgett method,'' vol. 2093, p. 020041, American Institute of Physics Inc., 4 2019.

[41] L. Valli, ``Phthalocyanine-based langmuir-blodgett films as chemical sensors,'' *Advances in Colloid and Interface Science*, vol. 116, pp. 13--44, 11 2005.

[42] M. C. Petty, *Langmuir-Blodgett Films*. Cambridge University Press, 2 1996.

[43] T. V. Basova, V. G. Kiselev, V. A. Plyashkevich, P. B. Cheblakov, F. Latteyer, H. Peisert, and T. Chassè, ``Orientation and morphology of chloroaluminum phthalocyanine films grown by vapor deposition: Electrical field-induced molecular alignment,'' *Chemical Physics*, vol. 380, pp. 40--47, 2 2011.

[44] D. M. Mattox, *Handbook of Physical Vapor Deposition (PVD) Processing*. 2007.

[45] G. Ran, J. Wang, J. Yue, M. Pei, J. Chen, and W. Zhang, ``Femtosecond excited state dynamics of liquid deposited magnesium phthalocyanine thin films,'' *Chemical Physics Letters*, vol. 751, p. 137501, 2020.

[46] Q. Wang, F. Yang, Y. Zhang, M. Chen, X. Zhang, S. Lei, R. Li, and W. Hu, ``Space-confined strategy toward large-area two-dimensional single crystals of molecular materials,'' *Journal of the American Chemical Society*, vol. 140, pp. 5339--5342, 4 2018.

[47] S. M. Critchley, M. R. Willis, M. J. Cook, J. Mcmurdob, and Y. Maruyamac, ``Deposition of ordered phthalocyanine films by spin coating,'' 1992.

[48] K. Vasseur, K. Broch, A. L. Ayzner, B. P. Rand, D. Cheyns, C. Frank, F. Schreiber, M. F. Toney, L. Froyen, and P. Heremans, ``Controlling the texture and crystallinity of evaporated lead phthalocyanine thin films for near-infrared sensitive solar cells,'' *ACS Applied Materials and Interfaces*, vol. 5, pp. 8505--8515, 2013.

[49] Z. Valicsek and O. Horváth, ``Application of the electronic spectra of porphyrins for analytical purposes: The effects of metal ions and structural distortions,'' *Microchemical Journal*, vol. 107, pp. 47--62, 2013.

[50] T. Schwieger, H. Peisert, M. S. Golden, M. Knupfer, and J. Fink, ``Electronic structure of the organic semiconductor copper phthalocyanine and k-cupc studied using photoemission spectroscopy,'' *Physical Review B - Condensed Matter and Materials Physics*, vol. 66, pp. 1--5, 2002.

[51] J. Mizuguchi, G. Rihs, and H. R. Karfunkel, ``Solid-state spectra of titanylphthalocyanine as viewed from molecular distortion,'' *Journal of Physical Chemistry*, vol. 99, pp. 16217--16227, 1995.

[52] J. E. Norton and J. L. Brédas, ``Theoretical characterization of titanyl phthalocyanine as a p-type organic semiconductor: Short intermolecular π-π interactions yield large electronic couplings and hole transport bandwidths,'' *Journal of Chemical Physics*, vol. 128, p. 1228, 2008.

[53] A. Endo, S. Matsumoto, and J. Mizuguchi, ``Interpretation of the near-infrared absorption of magnesium phthalocyanine complexes in terms of exciton coupling effects,'' *Journal of Physical Chemistry A*, vol. 103, pp. 8193--8199, 1999.

[54] X. Zhang, Y. Zhang, and J. Jiang, ``Towards clarifying the n-m vibrational nature of metallo-phthalocyanines: Infrared spectrum of phthalocyanine magnesium complex: Density functional calculations,'' *Spectrochimica Acta - Part A: Molecular and Biomolecular Spectroscopy*, vol. 60, pp. 2195--2200, 8 2004.

[55] J. Mi, L. Guo, Y. Liu, W. Liu, G. You, and S. Qian, ``Excited-state dynamics of magnesium phthalocyanine thin film,'' 2003.

[56] G. Ma, L. Guo, J. Mi, Y. Liu, S. Qian, D. Pan, and Y. Huang, ``Femtosecond nonlinear optical response of metallophthalocyanine films,'' *Solid State Communications*, vol. 118, pp. 633--638, 2001.

[57] R. Seoudi, G. S. El-Bahy, and Z. A. E. Sayed, ``Ultraviolet and visible spectroscopic studies of phthalocyanine and its complexes thin films,'' *Optical Materials*, vol. 29, pp. 304--312, 2006.

[58] V. Gulbinas, M. Chachisvilis, A. Persson, S. Svanberg, and V. Sundström, ``Ultrafast excitation relaxation in colloidal particles of chloroaluminum phthalocyanine: One-dimensional exciton-exciton annihilation,'' *Journal of Physical Chemistry*, vol. 98, pp. 8118--8123, 1994.

[59] V. Gulbinas, M. Chachisvilis, L. Valkunas, and V. Sundström, ``Excited state dynamics of phthalocyanine films,'' *Journal of Physical Chemistry*, vol. 100, pp. 2213--2219, 1996.

[60] J. R. Johansson, P. D. Nation, and F. Nori, ``Qutip: An open-source python framework for the dynamics of open quantum systems,'' *Computer Physics Communications*, vol. 183, pp. 1760--1772, 8 2012.

[61] J. R. Johansson, P. D. Nation, and F. Nori, ``Qutip 2: A python framework for the dynamics of open quantum systems,'' *Computer Physics Communications*, vol. 184, pp. 1234--1240, 4 2013.

[62] J. Itatani, F. Quéré, G. L. Yudin, M. Y. Ivanov, F. Krausz, and P. B. Corkum, ``Attosecond streak camera,'' *Physical Review Letters*, vol. 88, p. 4, 2002.

[63] M. Drescher, M. Hentschel, R. Kienberger, G. Tempea, C. Spielmann, G. A. Reider, P. B. Corkum, and F. Krausz, ``X-ray pulses approaching the attosecond frontier,'' *Science*, vol. 291, pp. 1923--1927, 2001.

[64] M. V. Ammosov, N. B. Delone, and V. P. Krainov, ``Tunnel ionization of complex atoms and of atomic ions in an alternating electromagnetic field,'' *Sov. Phys. JETP*, vol. 64, 1986.

[65] G. L. Yudin and M. Y. Ivanov, ``Nonadiabatic tunnel ionization: Looking inside a laser cycle,'' *PHYSICAL REVIEW A*, vol. 64, 2001.

[66] T. Popmintchev, M. C. Chen, D. Popmintchev, P. Arpin, S. Brown, S. Ališauskas, G. Andriukaitis, T. Balčiunas, O. D. Mücke, A. Pugzlys, A. Baltuška, B. Shim, S. E. Schrauth, A. Gaeta, C. Hernández-García, L. Plaja, A. Becker, A. Jaron-Becker, M. M. Murnane, and H. C. Kapteyn, ``Bright coherent ultrahigh harmonics in the kev x-ray regime from mid-infrared femtosecond lasers,'' *Science*, vol. 336, pp. 1287--1291, 2012.

[67] N. H. Burnett, H. A. Baldis, M. C. Richardson, and G. D. Enright, ``Harmonic generation in co2 laser target interaction,'' *Applied Physics Letters*, vol. 31, pp. 172--174, 1977.

[68] A. McPherson, G. Gibson, H. Jara, U. Johann, T. S. Luk, I. A. McIntyre, K. Boyer, and C. K. Rhodes, ``Studies of multiphoton production of vacuum-ultraviolet radiation in the rare gases,'' *Journal of the Optical Society of America B*, vol. 4, p. 595, 4 1987.

[69] M. Ferray, A. L'Huillier, X. F. Li, L. A. Lompre, G. Mainfray, and C. Manus, ``Multiple-harmonic conversion of 1064 nm radiation in rare gases,'' *Journal of Physics B: Atomic, Molecular and Optical Physics*, vol. 21, p. L31, 1988.

[70] X. F. Li, A. L. Huillier, M. Ferray, L. A. Lompre, and G. Mainfray, ``Multiple-harmonic generation in rare gases at high laser intensity,'' 1989.

[71] A. L'Huillier, P. Balcou, S. Candel, K. J. Schafer, and K. C. Kulander, ``Calculations of high-order harmonic-generation processes in xenon at 1064 nm,'' *Physical Review A*, vol. 46, pp. 2778--2790, 1992.

[72] P. B. Corkum, ``Plasma perspective on strong field multiphoton ionization,'' *Physical Review Letters*, vol. 71, pp. 1994--1997, 1993.

[73] I. Adawi, ``Theory of the surface photoelectric effect for one and two photons,'' *Physical Review*, vol. 134, p. A788, 1964.

[74] J. F. Clauser, ``Experimental distinction between the quantum and classical field-theoretic predictions for the photoelectric effect,'' *Physical Review D*, vol. 9, pp. 853--860, 1974.

[75] V. S. Yakovlev, F. Bammer, and A. Scrinzi, ``Attosecond streaking measurements,'' vol. 52, pp. 395--410, 2005.

[76] H. R. Reiss

[77] Y. Mairesse and F. Quéré, ``Frequency-resolved optical gating for complete reconstruction of attosecond bursts,'' *Physical Review A - Atomic, Molecular, and Optical Physics*, vol. 71, p. 011401, 2005.

[78] J. Gagnon, E. Goulielmakis, and V. S. Yakovlev, ``The accurate frog characterization of attosecond pulses from streaking measurements,'' *Applied Physics B: Lasers and Optics*, vol. 92, pp. 25--32, 7 2008.

[79] M. Lucchini, M. Brügmann, A. Ludwig, L. Gallmann, U. Keller, and T. Feurer, ``Ptychographic reconstruction of attosecond pulses,'' *Optics Express*, vol. 23, p. 29502, 2015.

[80] M. Lucchini and M. Nisoli, ``Refined ptychographic reconstruction of attosecond pulses,'' *Applied Sciences (Switzerland)*, vol. 8, p. 2563, 12 2018.

[81] M. Schultze, M. Fieß, N. Karpowicz, J. Gagnon, M. Korbman, M. Hofstetter, S. Neppl, A. L. Cavalieri, Y. Komninos, T. Mercouris, C. A. Nicolaides, R. Pazourek, S. Nagele, J. Feist, J. Burgdörfer, A. M. Azzeer, R. Ernstorfer, R. Kienberger, U. Kleineberg, E. Goulielmakis, F. Krausz, and V. S. Yakovlev, ``Delay in photoemission,'' *Science*, vol. 328, pp. 1658--1662, 6 2010.

[82] S. Neppl, R. Ernstorfer, E. M. Bothschafter, A. L. Cavalieri, D. Menzel, J. V. Barth, F. Krausz, R. Kienberger, and P. Feulner, ``Attosecond time-resolved photoemission from core and valence states of magnesium,'' *Physical Review Letters*, vol. 109, 2012.

[83] M. T. Ossiander, ``Absolute photoemission timing,'' 2018.

[84] J. E. Riemensberger, ``Time-frequency-resolved absolute time delay of the photoelectric effect,'' 2018.

[85] R. Pazourek, S. Nagele, and J. Burgdörfer, ``Attosecond chronoscopy of photoemission,'' *Reviews of Modern Physics*, vol. 87, 2015.

[86] F. Krausz and M. Ivanov, ``Attosecond physics,'' *REVIEWS OF MODERN PHYSICS*, vol. 163, pp. 0034--6861, 2009.

[87] E. Magerl, S. Neppl, A. L. Cavalieri, E. M. Bothschafter, M. Stanislawski, T. Uphues, M. Hofstetter, U. Kleineberg, J. V. Barth, D. Menzel, F. Krausz, R. Ernstorfer, R. Kienberger, and P. Feulner, ``A flexible apparatus for attosecond photoelectron spectroscopy of solids and surfaces,'' *Review of Scientific Instruments*, vol. 82, p. 063104, 2011.

[88] J. Riemensberger, S. Neppl, D. Potamianos, M. Schäffer, M. Schnitzenbaumer, M. Ossiander, C. Schröder, A. Guggenmos, U. Kleineberg, D. Menzel, F. Allegretti, J. V. Barth, R. Kienberger, P. Feulner, A. G. Borisov, P. M. Echenique, and A. K. Kazansky, ``Attosecond dynamics of sp-band photoexcitation,'' *Physical Review Letters*, vol. 123, p. 176801, oct 2019.

[89] F. Lücking, A. Assion, A. Apolonski, F. Krausz, and G. Steinmeyer, ``Long-term carrier-envelope-phase-stable few-cycle pulses by use of the feed-forward method,'' *Optics Letters*, vol. 37, p. 2076, 2012.

[90] D. Strickland and G. Mourou, ``Compression of amplified chirped optical pulses,'' *Optics Communications*, vol. 56, pp. 219--221, 1985.

[91] P. Tournois, ``Acousto-optic programmable dispersive filter for adaptive compensation of group delay time dispersion in laser systems,'' *Optics Communications*, vol. 140, pp. 245--249, 1997.

[92] F. Verluise, V. Laude, Z. Cheng, C. Spielmann, and P. Tournois, ``Amplitude and phase control of ultrashort pulses by use of an acousto-optic programmable dispersive filter: pulse compression and shaping,'' *Optics Letters*, vol. 25, p. 575, 2000.

[93] L.-P. Oloff, K. Hanff, A. Stange, G. Rohde, F. Diekmann, M. Bauer, K. Rossnagel, and . K. Hanff, ``Pump laser-induced space-charge effects in hhg-driven time-and angle-resolved photoelectron spectroscopy,'' *J. Appl. Phys*, vol. 119, p. 225106, 2016.

[94] J. Enkovaara, C. Rostgaard, J. J. Mortensen, J. Chen, M. Dułak, L. Ferrighi, J. Gavnholt, C. Glinsvad, V. Haikola, H. A. Hansen, H. H. Kristoffersen, M. Kuisma, A. H. Larsen, L. Lehtovaara, M. Ljungberg, O. Lopez-Acevedo, P. G. Moses, J. Ojanen, T. Olsen, V. Petzold, N. A. Romero, J. Stausholm-Møller, M. Strange, G. A. Tritsaris, M. Vanin, M. Walter, B. Hammer, H. Häkkinen, G. K. Madsen, R. M. Nieminen, J. K. Nørskov, M. Puska, T. T. Rantala, J. Schiøtz, K. S. Thygesen, and K. W. Jacobsen, ``Electronic structure calculations with gpaw: A real-space implementation of the projector augmented-wave method,'' 2010.

[95] J. J. Mortensen, L. B. Hansen, and K. W. Jacobsen, ``Real-space grid implementation of the projector augmented wave method,'' *Physical Review B - Condensed Matter and Materials Physics*, vol. 71, p. 035109, 2005.

[96] A. Picón, L. Plaja, and J. Biegert, ``Attosecond x-ray transient absorption in condensed--matter: a core-state-resolved bloch model,'' *New Journal of Physics*, vol. 21, p. 043029, 2019.

[97] F. Schlaepfer, M. Lucchini, S. A. Sato, M. Volkov, L. Kasmi, N. Hartmann, A. Rubio, L. Gallmann, and U. Keller, ``Attosecond optical-field-enhanced carrier injection into the gaas conduction band,'' *Nature Physics*, 2018.

[98] P. Eckle, M. Smolarski, P. Schlup, J. Biegert, A. Staudte, M. Schöffler, H. G. Muller, R. Dörner, and U. Keller, ``Attosecond angular streaking,'' *Nature Physics*, vol. 4, no. 7, pp. 565--570, 2008.

[99] M. Fanciulli, H. Volfová, S. Muff, J. Braun, H. Ebert, J. Minár, U. Heinzmann, and J. H. Dil, ``Spin Polarization and Attosecond Time Delay in Photoemission from Spin Degenerate States of Solids,'' *Physical Review Letters*, vol. 118, no. 6, p. 067402, 2017.

[100] T. Barillot, C. Cauchy, P. A. Hervieux, M. Gisselbrecht, S. E. Canton, P. Johnsson, J. Laksman, E. P. Mansson, J. M. Dahlström, M. Magrakvelidze, G. Dixit, M. E. Madjet, H. S. Chakraborty, E. Suraud, P. M. Dinh, P. Wopperer, K. Hansen, V. Loriot, C. Bordas, S. Sorensen, and F. Lépine, ``Angular asymmetry and attosecond time delay from the giant plasmon resonance in C60 photoionization,'' *Physical Review A - Atomic, Molecular, and Optical Physics*, vol. 91, p. 033413, mar 2015.

[101] F. Roth, T. Arion, H. Kaser, A. Gottwald, and W. Eberhardt, ``Angle resolved Photoemission from Ag and Au single crystals: Final state lifetimes in the attosecond range,'' *Journal of Electron Spectroscopy and Related Phenomena*, vol. 224, pp. 84--92, apr 2018.

[102] A. Damascelli, ``Probing the electronic structure of complex systems by ARPES,'' *Physica Scripta T*, vol. T109, no. T109, pp. 61--74, 2004.

[103] J. H. Ryoo and C. H. Park, ``Spin-conserving and reversing photoemission from the surface states of Bi2Se3 and Au (111),'' *Physical Review B*, vol. 93, no. 8, p. 085419, 2016.

[104] C. N. Berglund and W. E. Spicer, ``Photoemission studies of copper and silver: Theory,'' *Physical Review*, vol. 136, p. A1030, 1964.

[105] C. N. Berglund and W. E. Spicer, ``Photoemission studies of copper and silver: Experiment,'' *Physical Review*, vol. 136, p. A1044, 1964.

[106] G. D. Mahan, ``Theory of photoemission in simple metals,'' *Physical Review B*, vol. 2, pp. 4334--4350, 1970.

[107] M. Schnitzenbaumer, ``Attosecond dynamics of the photoelectric effect at the bandgap of a single-element layered system,'' 2021.

[108] K. S. Novoselov, A. K. Geim, S. V. Morozov, D. Jiang, Y. Zhang, S. V. Dubonos, I. V. Grigorieva, and A. A. Firsov, ``Electric field in atomically thin carbon films,'' *Science*, vol. 306, pp. 666--669, 2004.

[109] A. B. Djurišić and E. H. Li, ``Optical properties of graphite,'' *Journal of Applied Physics*, vol. 85, pp. 7404--7410, may 1999.

[110] J. Pappis and S. L. Blum, ``Properties of Pyrolytic Graphite,'' *Journal of the American Ceramic Society*, vol. 44, no. 12, pp. 592--597, 1961.

[111] L. C. F. Blackman and A. J. P. Ubbelohde

[112] F. Matsui, H. Nishikawa, H. Daimon, M. Muntwiler, M. Takizawa, H. Namba, and T. Greber, ``The 4π kz periodicity in photoemission from graphite,'' *Physical Review B*, vol. 97, p. 045430, jan 2018.

[113] C. Lechner, B. Pannier, P. Baranek, N. C. Forero-Martinez, and H. Vach, ``First-Principles Study of the Structural, Electronic, Dynamic, and Mechanical Properties of HOPG and Diamond: Influence of Exchange-Correlation Functionals and Dispersion Interactions,'' *Journal of Physical Chemistry C*, vol. 120, pp. 5083--5100, mar 2016.

[114] K. Endo, S. Koizumi, T. Otsuka, M. Suhara, T. Morohasi, E. Z. Kurmaev, and D. P. Chong, ``Analysis of xps and xes of diamond and graphite by dft calculations using model molecules,'' *Journal of Computational Chemistry*, vol. 22, no. 1, pp. 102--108, 2001.

[115] M. Ossiander, J. Riemensberger, S. Neppl, M. Mittermair, M. Schäffer, A. Duensing, M. S. Wagner, R. Heider, M. Wurzer, M. Gerl, M. Schnitzenbaumer, J. V. Barth, F. Libisch, C. Lemell, J. Burgdörfer, P. Feulner, and R. Kienberger, ``Absolute timing of the photoelectric effect,'' *Nature*, vol. 561, pp. 374--377, 2018.

[116] G. Iannaccone, ``General relation between density of states and dwell times in mesoscopic systems,'' *Physical Review B*, vol. 51, pp. 4727--4729, feb 1995.

[117] F. T. Smith, ``Lifetime matrix in collision theory,'' *Physical Review*, vol. 118, pp. 349--356, apr 1960.

[118] H. G. Winful, ``Tunneling time, the Hartman effect, and superluminality: A proposed resolution of an old paradox,'' dec 2006.

[119] C. A. De Carvalho and H. M. Nussenzveig, ``Time delay,'' jun 2002.

[120] B. Song, H. Gu, S. Zhu, H. Jiang, X. Chen, C. Zhang, and S. Liu, ``Broadband optical properties of graphene and HOPG investigated by spectroscopic Mueller matrix ellipsometry,'' *Applied Surface Science*, vol. 439, pp. 1079--1087, may 2018.

[121] S. Passlack, S. Mathias, O. Andreyev, D. Mittnacht, M. Aeschlimann, and M. Bauer, ``Space charge effects in photoemission with a low repetition, high intensity femtosecond laser source,'' *Journal of Applied Physics*, vol. 100, p. 24912, 2006.

[122] J. Graf, S. Hellmann, C. Jozwiak, C. L. Smallwood, Z. Hussain, R. A. Kaindl, L. Kipp, K. Rossnagel, and A. Lanzara, ``Vacuum space charge effect in laser-based solid-state photoemission spectroscopy,'' *J. Appl. Phys*, vol. 107, p. 14912, 2010.

[123] S. Hellmann, K. Rossnagel, M. Marczynski-Bühlow, and L. Kipp, ``Vacuum space-charge effects in solid-state photoemission,'' *Physical Review B*, vol. 79, 2009.

[124] C. Corder, P. Zhao, J. Bakalis, X. Li, M. D. Kershis, A. R. Muraca, M. G. White, and T. K. Allison, ``Ultrafast extreme ultraviolet photoemission without space charge,'' *Structural Dynamics*, vol. 5, 2018.

[125] L. P. Oloff, M. Oura, K. Rossnagel, A. Chainani, M. Matsunami, R. Eguchi, T. Kiss, Y. Nakatani, T. Yamaguchi, J. Miyawaki, M. Taguchi, K. Yamagami, T. Togashi, T. Katayama, K. Ogawa, M. Yabashi, and T. Ishikawa, ``Time-resolved haxpes at sacla: Probe and pump pulse-induced space-charge effects,'' *New Journal of Physics*, vol. 16, 2014.

[126] R. Al-Obaidi, M. Wilke, M. Borgwardt, J. Metje, A. Moguilevski, B. Engel, D. Tolksdorf, A. Raheem, T. Kampen, and S. Mähl, ``Ultrafast photoelectron spectroscopy of solutions: space-charge effect,'' *New Journal of Physics*, 2015.

[127] G. Panaccione, G. Cautero, M. Cautero, A. Fondacaro, M. Grioni, P. Lacovig, G. Monaco, F. Offi, G. Paolicelli, M. Sacchi, N. Stojić, G. Stefani, R. Tommasini, and P. Torelli, ``High-energy photoemission in silver: resolving d and sp contributions in valence band spectra,'' *J.Phys.: Condens. Matter*, vol. 17, pp. 2671--2679, 2005.

[128] B. Schönhense, K. Medjanik, O. Fedchenko, S. Chernov, M. Ellguth, D. Vasilyev, A. Oelsner, J. Viefhaus, D. Kutnyakhov, W. Wurth, H. J. Elmers, and G. Schönhense, ``Multidimensional photoemission spectroscopy - the space-charge limit,'' *New Journal of Physics*, vol. 20, 2018.

[129] M. Ossiander, F. Siegrist, V. Shirvanyan, R. Pazourek, A. Sommer, T. Latka, A. Guggenmos, S. Nagele, J. Feist, J. Burgdörfer, R. Kienberger, and M. Schultze, ``Attosecond correlation dynamics,'' *Nature Physics*, vol. 13, pp. 280--285, 3 2017.

[130] R. Trebino, *Frequency-Resolved Optical Gating: The Measurement of Ultrashort Laser Pulses*. Springer US, 2000.

[131] K. W. Delong, D. N. Fittinghoff, R. Trebino, B. Kohler, and K. Wilson, ``Pulse retrieval in frequency-resolved optical gating based on the method of generalized projections,'' 1994.

[132] A. Maiden, D. Johnson, and P. Li, ``Further improvements to the ptychographical iterative engine,'' *Optica*, vol. 4, p. 736, 2017.

Acknowledgements

During the course of this work there where many people who helped and endorsed me. I would like to start by thanking Prof. Dr. Kienberger Reinhard for offering me the opportunity to work under his supervision in a state of the art laboratory allowing me to have a front seat in the exploration at the frontier of science.

A lot of support came from my colleagues, helping me learn, supporting my efforts and helping me overcome the language barrier. Most prominent where Schnitzenbaumer Maximilian, with continuous organization efforts, hard work and splendid cooperation, Scigalla Pascal, Schröder Christian, Haimerl Michael and Schock Eckhard with tireless efforts in the technical, experimental, programming support and maintenance of the lab. A lot of knowledge and knowhow as well as part pf my training in the setup came from Riemensberger Johann, Ossiander Marcus, Shirvanyan Vahe, Duensing Andreas, Akil Ayman, to whom I am grateful.

A special section needs to be dedicated firstly to PD Dr. Iglev Hristo and then to Matthias Nuber and Schletter Albert for listening, understanding and immediately responding during a dire occation that with their support was turned into a success story.

This work took place in the Max Plank Institute for Quantum Optics and the Technical University of Munich and was partially funded by the program MEDEA which was part of the European Union's Horizon 2020 research and innovation program under the Marie Skłodowska-Curie grant agreement No 641789. MEDEA also offered excellent training and networking opportunities that significantly eased my transition into the attosecond field.

Last but not least is the support from my family and friends without whom this work would not have even started. Out of my friends, there are two special groups who deserve special treatment. First is a group of ex-colleagues, as they are actively involved in research and could fully understand and support me in my struggles. Papagiannouli Irene, Kakkava Irene, Orfanos Ioannis and Papadakis Ioannis were all very supportive and happy to discuss both the scientific and the personal concerns involving this work. Secondly, a group of friends that with their presence they made living abroad a breeze, namely Vogiatzi Chrysoula, Koufaki Anastasia and Chlis Nikolaos.